

Dr. J. W. Rockway

LEVEL II

ADA097326



NUMERICAL SOLUTIONS FOR SCATTERING BY RECTANGULAR BENT PLATE STRUCTURES

By

Donald R. Wilton

Allen W. Glisson

Chalmers M. Butler

Department of Electrical Engineering
University of Mississippi.
University, Mississippi 38677

For

Naval Electronics Laboratory Center
San Diego, California 92152

Contract No. N00123-75-C-1372

October, 1976

Approved for public release;
distribution unlimited.

814

3094

UNCLASSIFIED

SECURITY CLASSIFICATION OF THIS PAGE (When Data Entered)

REPORT DOCUMENTATION PAGE		READ INSTRUCTIONS BEFORE COMPLETING FORM
1. REPORT NUMBER <i>(6) HD-A097326</i>	2. GOVT ACCESSION NO. <i>HD-A097326</i>	3. PECIOPENT'S CATALOG NUMBER
4. TITLE (and Subtitle) <i>NUMERICAL SOLUTIONS FOR SCATTERING BY RECTANGULAR BENT PLATE STRUCTURES.</i>	5. TYPE OF REPORT & PERIOD COVERED Final (6/1/75 - 10/31/76)	
7. AUTHOR(s) <i>(10) Donald R. Wilton Allen W. Glisson Chalmers M. Butler</i>	8. CONTRACT OR GRANT NUMBER(s) <i>(15) N00123-75-C-1372</i>	6. PERFORMING ORG. REPORT NUMBER
9. PERFORMING ORGANIZATION NAME AND ADDRESS Department of Electrical Engineering University of Mississippi University, Mississippi 38677	10. PROGRAM ELEMENT, PROJECT, TASK AREA & WORK UNIT NUMBERS <i>(17) 62762N XF54585004</i>	11. REPORT DATE <i>(18) Oct 1976</i>
11. CONTROLLING OFFICE NAME AND ADDRESS Naval Electronics Laboratory Center San Diego, California 92152	12. NUMBER OF PAGES <i>(19) 157</i>	13. SECURITY CLASS. (of this report) <i>UNCLASSIFIED</i>
14. MONITORING AGENCY NAME & ADDRESS(if different from Controlling Office) ONRRR, University of Alabama in Huntsville Research Institute Post Office Box 1247 Huntsville, Alabama 35807	15a. DECLASSIFICATION/DOWNGRADING SCHEDULE	
16. DISTRIBUTION STATEMENT (of this Report) <i>Approved for Public Release; Distribution Unlimited</i>	17. DISTRIBUTION STATEMENT (of the abstract entered in Block 20, if different from Report) <i>(9) Final Sept. 1 Jun 75-31 Oct 76</i>	
18. SUPPLEMENTARY NOTES		
19. KEY WORDS (Continue on reverse side if necessary and identify by block number) Rectangular Bent Plate Numerical Techniques Induced Currents Scattering Electromagnetic Theory		
20. ABSTRACT (Continue on reverse side if necessary and identify by block number) <i>(21) This report considers the numerical determination of the current induced on a bent rectangular plate illuminated by an incident plane wave. Drawing heavily on techniques which are first proven effective for the two-dimensional problems of scattering of TE and TM plane waves incident on infinitely long bent strips, the authors develop a unique staggered subdomain scheme for representing the currents on a bent plate. The resulting numerical techniques are</i>		

UNCLASSIFIED

SECURITY CLASSIFICATION OF THIS PAGE (When Data Entered)

simple, efficient, and highly convergent. Computed current distributions are given for two frequencies and for several angles of incidence for both a flat square plate and a bent square plate.

UNCLASSIFIED

SECURITY CLASSIFICATION OF THIS PAGE (When Data Entered)

NUMERICAL SOLUTIONS FOR SCATTERING
BY RECTANGULAR BENT PLATE STRUCTURES

by

Donald R. Wilton
Allen W. Glisson
Chalmers M. Butler

Department of Electrical Engineering
University of Mississippi
University, Mississippi 38677

for

Naval Electronics Laboratory Center
San Diego, California 92152

Contract No. N00123-75-C-1372

October, 1976

ABSTRACT

This report considers the numerical determination of the current induced on a bent rectangular plate illuminated by an incident plane wave. Drawing heavily on techniques which are first proven effective for the two-dimensional problems of scattering of TE and TM plane waves incident on infinitely long bent strips, the authors develop a unique staggered subdomain scheme for representing the currents on a bent plate. The resulting numerical techniques are simple, efficient, and highly convergent. Computed current distributions are given for two frequencies and for several angles of incidence for both a flat square plate and a bent square plate.

Accession For	<input checked="" type="checkbox"/>
NTIS ST. LI	<input type="checkbox"/>
NTIS ST. LI	<input type="checkbox"/>
U.S. GOVT	<input type="checkbox"/>
Other	<input type="checkbox"/>
Classification	
Controlled by	
Priority Codes	
.. and/or	
Dist. Special	
A	

TABLE OF CONTENTS

	<u>Page</u>
TITLE PAGE	iii
ABSTRACT	iv
TABLE OF CONTENTS	v
LIST OF FIGURES	vii
SECTION I INTRODUCTION	1
SECTION II NUMERICAL SOLUTION PROCEDURE FOR A BENT STRIP WITH TRANSVERSE MAGNETIC ILLUMINATION	4
Formulation of the Integral Equation	4
Effect of the Edge Condition on Numerical Solutions	10
Effect of the Bend on Numerical Solutions	11
Effect of Differing Subdomain Sizes on Numerical Solutions	14
SECTION III NUMERICAL SOLUTION PROCEDURE FOR A BENT STRIP WITH TRANSVERSE ELECTRIC ILLUMINATION	22
Formulation of the Integral Equation	22
Effect of Placement of Edge Subdomains on Numerical Solutions	32
Effect of the Bend on Numerical Solutions	33
Effect of Differing Subdomain Sizes on Numerical Solutions	38

	<u>Page</u>	
SECTION IV	FORMULATION OF NUMERICAL SOLUTION FOR SCATTERING BY A BENT PLATE	43
	Formulation of the Integral Equations	43
SECTION V	NUMERICAL RESULTS FOR PLATE STRUCTURES	62
SECTION VI	CONCLUSIONS AND RECOMMENDATIONS	91
APPENDIX A	BEHAVIOR OF CURRENTS NEAR BENDS AND EDGES	95
APPENDIX B	SURFACE CURRENT ON A THIN SCATTERER	102
APPENDIX C	INTEGRATION OF THE SELF PATCH	106
APPENDIX D	BEHAVIOR OF SURFACE CURRENT NEAR A CORNER	109
APPENDIX E	PATCH CURRENT CORRECTION FACTOR FOR CURRENTS FLOWING PARALLEL TO AN EDGE	115
APPENDIX F	ALTERNATE FORMS FOR THE INTEGRAL EQUATION FOR A BENT PLATE	121
APPENDIX G	DETERMINATION OF CURRENTS EXCITED ON A WIRE/PLATE STRUCTURE	126
	REFERENCES	142

LIST OF FIGURES

<u>Figure</u>		<u>Page</u>
2.1 Strip configuration for TM illumination.		5
2.2 Pulse basis functions and match points for the TM illuminated bent strip.		7
2.3 Induced current on a 0.1λ strip illuminated by a normally incident TM plane wave.		12
2.4 Induced current on a 1.0λ strip illuminated by a normally incident TM plane wave.		13
2.5 Induced current on a 1.0λ strip bent 30° at $s/\lambda = 0$ and illuminated by a TM plane wave normally incident to the section of the strip $s/\lambda < 0$.		15
2.6 Induced current on a 1.0λ strip bent 60° at $s/\lambda = 0$ and illuminated by a TM plane wave normally incident to the section of the strip $s/\lambda < 0$.		16
2.7 Induced current on a 1.0λ strip bent 90° at $s/\lambda = 0$ and illuminated by a TM plane wave normally incident to the section of the strip $s/\lambda < 0$.		17
2.8 Induced current on a 1.0λ strip illuminated by a normally incident TM plane wave. Subdomain size changes at $s/\lambda = 0$ by a ratio of 10 to 1. (Compare with Figure 2.4.)		19
2.9 Induced current on a 1.0λ strip illuminated by a normally incident TM plane wave. Subdomain size changes at $s/\lambda = 0$ by a ratio of 10 to 1.		20

<u>Figure</u>		<u>Page</u>
2.10	Induced current on a 1.0λ strip bent 60° at $s/\lambda = 0$ and illuminated by a TM plane wave normally incident to the section of the strip $s/\lambda < 0$. Subdomain size changes at $s/\lambda = 0$ by a ratio of 10 to 1. (Compare with Figure 2.6.)	21
3.1	Strip configuration for TE illumination.	23
3.2	Pulse basis functions and match points for the TE illuminated bent strip.	25
3.3	Pulse basis functions for the charge on the TE illuminated bent strip.	27
3.4	Comparison of convergence for a 0.5λ strip illuminated by a normally incident TE plane wave when full subdomains and half subdomains are used to represent the current at the edges.	34
3.5	Induced current on a 0.1λ strip bent 90° and illuminated by a TE plane wave normally incident to the section of the strip $s/\lambda < 0$.	36
3.6	Induced current on a 0.1λ strip bent 90° at $s/\lambda = 0$ and illuminated symmetrically by a TE plane wave ($\phi = 135^\circ$).	37
3.7	Comparsion of asymptotic behavior of current (solid line) at the bend for the case shown in Figure 3.6 with the numerically computed current behavior (crosses). The data are matched at the bend ($s = 0$) and at the third numerical value away from the bend.	39
3.8	Induced current on a 1.0λ strip illuminated by a normally incident TE plane wave. Subdomain size changes at $s/\lambda = 0$ by a ratio of 10 to 1.	41
3.9	Induced current on a 0.1λ strip bent 90° at $s/\lambda = 0$ and illuminated by a TE plane wave normally incident to the section of the strip $s/\lambda < 0$. Subdomain size changes at $s/\lambda = 0$ by a ratio of 10 to 1. (Compare with Figure 3.5.)	42

<u>Figure</u>	<u>Page</u>
4.1 Geometry of the bent plate and incident fields.	44
4.2 Subdomain scheme for s-directed currents.	46
4.3 Subdomain scheme for y-directed currents.	47
4.4 Subdomain scheme for charge patches.	52
5.1 Convergence curves for 0.15λ and 1.0λ square plates for normal and oblique angles of incidence.	63
5.2 Current induced on a square plate, $S_x = 0.15\lambda, Y_d = 0.15\lambda, \theta = 0^\circ, \phi = 0^\circ,$ $H_\theta = 0.0, H_\phi = -1.0, M = 11, N = 10;$ (a) $\text{Re}(J_s)$, (b) $\text{Im}(J_s)$, (c) $\text{Re}(J_y)$, (d) $\text{Im}(J_y)$.	65
5.3 Current induced on a square plate, $S_x = 0.15\lambda, Y_d = 0.15\lambda, \theta = 45^\circ, \phi = 0^\circ,$ $H_\theta = 0.0, H_\phi = -1.0, M = 11, N = 10;$ (a) $\text{Re}(J_s)$, (b) $\text{Im}(J_s)$, (c) $\text{Re}(J_y)$, (d) $\text{Im}(J_y)$.	66
5.4 Current induced on a square plate, $S_x = 0.15\lambda, Y_d = 0.15\lambda, \theta = 45^\circ, \phi = 0^\circ,$ $H_\theta = 1.0, H_\phi = 0.0, M = 11, N = 10;$ (a) $\text{Re}(J_y)$, (b) $\text{Im}(J_y)$, (c) $\text{Re}(J_s)$, (d) $\text{Im}(J_s)$.	67
5.5 Current induced on a square plate, $S_x = 0.15\lambda, Y_d = 0.15\lambda, \theta = 45^\circ,$ $\phi = 270^\circ, H_\theta = 1.0, H_\phi = 0.0, M = 11,$ $N = 10; (a) \text{Re}(J_s), (b) \text{Im}(J_s),$ (c) $\text{Re}(J_y)$, (d) $\text{Im}(J_y)$.	68

<u>Figure</u>	<u>Page</u>
5.6 Current induced on a square plate, $S_x = 1.0\lambda, Y_d = 1.0\lambda, \theta = 0^\circ, \phi = 0^\circ,$ $H_\theta = 0.0, H_\phi = -1.0, M = 11, N = 10;$ (a) $\operatorname{Re}(J_s)$, (b) $\operatorname{Im}(J_s)$, (c) $\operatorname{Re}(J_y)$, (d) $\operatorname{Im}(J_y)$.	69
5.7 Current induced on a square plate, $S_x = 1.0\lambda, Y_d = 1.0\lambda, \theta = 45^\circ, \phi = 0^\circ,$ $H_\theta = 0.0, H_\phi = -1.0, M = 11, N = 10;$ (a) $\operatorname{Re}(J_s)$, (b) $\operatorname{Im}(J_s)$, (c) $\operatorname{Re}(J_y)$, (d) $\operatorname{Im}(J_y)$.	70
5.8 Current induced on a square plate, $S_x = 1.0\lambda, Y_d = 1.0\lambda, \theta = 45^\circ, \phi = 0^\circ,$ $H_\theta = 1.0, H_\phi = 0.0, M = 11, N = 10;$ (a) $\operatorname{Re}(J_y)$, (b) $\operatorname{Im}(J_y)$, (c) $\operatorname{Re}(J_s)$, (d) $\operatorname{Im}(J_s)$.	71
5.9 Current induced on a square plate, $S_x = 1.0\lambda, Y_d = 1.0\lambda, \theta = 45^\circ, \phi = 270^\circ,$ $H_\theta = 1.0, H_\phi = 0.0, M = 11, N = 10;$ (a) $\operatorname{Re}(J_s)$, (b) $\operatorname{Im}(J_s)$, (c) $\operatorname{Re}(J_y)$, (d) $\operatorname{Im}(J_y)$.	72
5.10 Current induced on a rectangular plate bent at $s = 0$, $S_x = 0.10\lambda, S_c = 0.05\lambda$, $Y_d = 0.15\lambda, \alpha = 50^\circ, \theta = 0^\circ, \phi = 0^\circ$, $H_\theta = 0.0, H_\phi = -1.0, \text{MPB} = 9, \text{MFB} = 5$, $N = 9$; (a) $\operatorname{Re}(J_s)$, (b) $\operatorname{Im}(J_s)$, (c) $\operatorname{Re}(J_y)$, (d) $\operatorname{Im}(J_y)$.	73
5.11 Current induced on a rectangular plate bent at $s = 0$, $S_x = 0.10\lambda, S_c = 0.05\lambda$, $Y_d = 0.15\lambda, \alpha = 50^\circ, \theta = 0^\circ, \phi = 0^\circ$, $H_\theta = 1.0, H_\phi = 0.0, \text{MPB} = 9, \text{MFB} = 5$, $N = 9$; (a) $\operatorname{Re}(J_y)$, (b) $\operatorname{Im}(J_y)$, (c) $\operatorname{Re}(J_s)$, (d) $\operatorname{Im}(J_s)$.	74

<u>Figure</u>	<u>Page</u>
5.12 Current induced on a rectangular plate bent at $s = 0$, $S_x = 0.10\lambda$, $S_c = 0.05\lambda$, $Y_d = 0.15\lambda$, $\alpha = 50^\circ$, $\theta = 45^\circ$, $\phi = 0^\circ$, $H_\theta = 0.0$, $H_\phi = -1.0$, MPB = 9, MFB = 5, $N = 9$; (a) $\text{Re}(J_s)$, (b) $\text{Im}(J_s)$, (c) $\text{Re}(J_y)$, (d) $\text{Im}(J_y)$.	75
5.13 Current induced on a rectangular plate bent at $s = 0$, $S_x = 0.10\lambda$, $S_c = 0.05\lambda$, $Y_d = 0.15\lambda$, $\alpha = 50^\circ$, $\theta = 45^\circ$, $\phi = 0^\circ$, $H_\theta = 1.0$, $H_\phi = 0.0$, MPB = 9, MFB = 5, $N = 9$; (a) $\text{Re}(J_y)$, (b) $\text{Im}(J_y)$, (c) $\text{Re}(J_s)$, (d) $\text{Im}(J_s)$.	76
5.14 Current induced on a rectangular plate bent at $s = 0$, $S_x = 0.10\lambda$, $S_c = 0.05\lambda$, $Y_d = 0.15\lambda$, $\alpha = 50^\circ$, $\theta = 45^\circ$, $\phi = 180^\circ$, $H_\theta = 0.0$, $H_\phi = 1.0$, MPB = 9, MFB = 5, $N = 9$; (a) $\text{Re}(J_s)$, (b) $\text{Im}(J_s)$, (c) $\text{Re}(J_y)$, (d) $\text{Im}(J_y)$.	77
5.15 Current induced on a rectangular plate bent at $s = 0$, $S_x = 0.19\lambda$, $S_c = 0.05\lambda$, $Y_d = 0.15\lambda$, $\alpha = 50^\circ$, $\theta = 45^\circ$, $\phi = 120^\circ$, $H_\theta = -1.0$, $H_\phi = 0.0$, MPB = 9, MFB = 5, $N = 9$; (a) $\text{Re}(J_y)$, (b) $\text{Im}(J_y)$, (c) $\text{Re}(J_s)$, (d) $\text{Im}(J_s)$.	78
5.16 Current induced on a rectangular plate bent at $s = 0$, $S_x = 0.10\lambda$, $S_c = 0.05\lambda$, $Y_d = 0.15\lambda$, $\alpha = 50^\circ$, $\theta = 45^\circ$, $\phi = 270^\circ$, $H_\theta = 0.0$, $H_\phi = 1.0$, MPB = 9, MFB = 5, $N = 9$; (a) $\text{Re}(J_y)$, (b) $\text{Im}(J_y)$, (c) $\text{Re}(J_s)$, (d) $\text{Im}(J_s)$.	79
5.17 Current induced on a rectangular plate bent at $s = 0$, $S_x = 0.10\lambda$, $S_c = 0.05\lambda$, $Y_d = 0.15\lambda$, $\alpha = 50^\circ$, $\theta = 45^\circ$, $\phi = 270^\circ$, $H_\theta = 1.0$, $H_\phi = 0.0$, MPB = 9, MFB = 5, $N = 9$; (a) $\text{Re}(J_s)$, (b) $\text{Im}(J_s)$, (c) $\text{Re}(J_y)$, (d) $\text{Im}(J_y)$.	80

<u>Figure</u>	<u>Page</u>
5.18 Current induced on a rectangular plate bent at $s = 0$, $S_x = 0.667\lambda$, $S_c = 0.333\lambda$, $Y_d = 1.0\lambda$, $\alpha = 50^\circ$, $\theta = 0^\circ$, $\phi = 0^\circ$, $H_\theta = 0.0$, $H_\phi = -1.0$, MPB = 9, MFB = 5, N = 9; (a) $\text{Re}(J_s)$, (b) $\text{Im}(J_s)$, (c) $\text{Re}(J_y)$, (d) $\text{Im}(J_y)$.	81
5.19 Current induced on a rectangular plate bent at $s = 0$, $S_x = 0.667\lambda$, $S_c = 0.333\lambda$, $Y_d = 1.0\lambda$, $\alpha = 50^\circ$, $\theta = 0^\circ$, $\phi = 0^\circ$, $H_\theta = 1.0$, $H_\phi = 0.0$, MPB = 9, MFB = 5, N = 9; (a) $\text{Re}(J_y)$, (b) $\text{Im}(J_y)$, (c) $\text{Re}(J_s)$, (d) $\text{Im}(J_s)$.	82
5.20 Current induced on a rectangular plate bent at $s = 0$, $S_x = 0.667\lambda$, $S_c = 0.333\lambda$, $Y_d = 1.0\lambda$, $\alpha = 50^\circ$, $\theta = 45^\circ$, $\phi = 0^\circ$, $H_\theta = 0.0$, $H_\phi = -1.0$, MPB = 9, MFB = 5, N = 9; (a) $\text{Re}(J_s)$, (b) $\text{Im}(J_s)$, (c) $\text{Re}(J_y)$, (d) $\text{Im}(J_y)$.	83
5.21 Current induced on a rectangular plate bent at $s = 0$, $S_x = 0.667\lambda$, $S_c = 0.333\lambda$, $Y_d = 1.0\lambda$, $\alpha = 50^\circ$, $\theta = 45^\circ$, $\phi = 0^\circ$, $H_\theta = 1.0$, $H_\phi = 0.0$, MPB = 9, MFB = 5, N = 9; (a) $\text{Re}(J_y)$, (b) $\text{Im}(J_y)$, (c) $\text{Re}(J_s)$, (d) $\text{Im}(J_s)$.	84
5.22 Current induced on a rectangular plate bent at $s = 0$, $S_x = 0.667\lambda$, $S_c = 0.333\lambda$, $Y_d = 1.0\lambda$, $\alpha = 50^\circ$, $\theta = 45^\circ$, $\phi = 180^\circ$, $H_\theta = 0.0$, $H_\phi = 1.0$, MPB = 9, MFB = 5, N = 9; (a) $\text{Re}(J_s)$, (b) $\text{Im}(J_s)$, (c) $\text{Re}(J_y)$, (d) $\text{Im}(J_y)$.	85

<u>Figure</u>	<u>Page</u>
5.23 Current induced on a rectangular plate bent at $s = 0$, $S_x = 0.667\lambda$, $S_c = 0.333\lambda$, $Y_d = 1.0\lambda$, $\alpha = 50^\circ$, $\theta = 45^\circ$, $\phi = 180^\circ$, $H_\theta = -1.0$, $H_\phi = 0.0$, MPB = 9, MFB = 5, $N = 9$; (a) $\text{Re}(J_y)$, (b) $\text{Im}(J_y)$, (c) $\text{Re}(J_s)$, (d) $\text{Im}(J_s)$.	86
5.24 Current induced on a rectangular plate bent at $s = 0$, $S_x = 0.667\lambda$, $S_c = 0.333\lambda$, $Y_d = 1.0\lambda$, $\alpha = 50^\circ$, $\theta = 45^\circ$, $\phi = 270^\circ$, $H_\theta = 0.0$, $H_\phi = 1.0$, MPB = 9, MFB = 5, $N = 9$; (a) $\text{Re}(J_y)$, (b) $\text{Im}(J_y)$, (c) $\text{Re}(J_s)$, (d) $\text{Im}(J_s)$.	87
5.25 Current induced on a rectangular plate bent at $s = 0$, $S_x = 0.667\lambda$, $S_c = 0.333\lambda$, $Y_d = 1.0\lambda$, $\alpha = 50^\circ$, $\theta = 45^\circ$, $\phi = 270^\circ$, $H_\theta = 1.0$, $H_\phi = 0.0$, MPB = 9, MFB = 5, $N = 9$; (a) $\text{Re}(J_s)$, (b) $\text{Im}(J_s)$, (c) $\text{Re}(J_y)$, (d) $\text{Im}(J_y)$.	88
A.1 Cross section of an infinite cylindrical wedge.	96
A.2 Cross section of a bent plate or strip with currents flowing parallel to and perpendicular to the bend.	96
A.3 Exterior currents on either side of a conducting edge.	100
A.4 Net equivalent currents near a conducting edge.	100
B.1 Sequence of steps to arrive at a net equivalent current: (a) original scatterer of maximum thickness Δt , (b) scatterer replaced by equivalent currents radiating in free space, (c) equivalent currents for a vanishingly thin scatterer, and (d) replacement of currents on either side by a net equivalent current representing the scatterer.	103

<u>Figure</u>	<u>Page</u>
D.1 Sphero-conal coordinates on an infinite quarter plane.	110
D.2 Behavior of the magnitude of the y component of current (J_y) near the corner of an infinite quarter plane located in the first quadrant of the $x-y$ plane.	114 119
E.1 Plot of the quasi-static patch current correction factor for currents flowing parallel to an edge as a function of the subdomain ratio $\Delta x/\Delta y$.	127
G.1 Geometry of a wire near a bent plate.	133
G.2 Current induced on a square plate near a wire, $S_x = 0.5\lambda$, $Y_d = 0.5\lambda$, $L = 1.0\lambda$, $a = .001\lambda$, $\bar{r}_c = (-0.125\lambda, -0.125\lambda, 0.525\lambda)$, $\hat{\ell} = (0.0, 0.0, 1.0)$, $\theta = 0^\circ$, $\phi = 0^\circ$, $H_\theta = 0.0$, $H_\phi = -1.0$; (a) $\text{Re}(J_s)$, (b) $\text{Im}(J_s)$, (c) $\text{Re}(J_y)$, (d) $\text{Im}(J_y)$. The wire current is shown in Figure G.3.	134
G.3 Current induced on a wire near a square plate, $S_x = 0.5\lambda$, $Y_d = 0.5\lambda$, $L = 1.0\lambda$, $a = .001\lambda$, $\bar{r}_c = (-0.125\lambda, -0.125\lambda, 0.525\lambda)$, $\hat{\ell} = (0.0, 0.0, 1.0)$, $\theta = 0^\circ$, $\phi = 0^\circ$, $H_\theta = 0.0$, $H_\phi = -1.0$. The plate current is shown in Figure G.2.	134
G.4 Current induced on a square plate near a wire, $S_x = 0.5\lambda$, $Y_d = 0.5\lambda$, $L = 1.0\lambda$, $a = .001\lambda$, $\bar{r}_c = (-0.125\lambda, -0.125\lambda, 0.525\lambda)$, $\hat{\ell} = (0.0, 0.0, 1.0)$, $\theta = 90^\circ$, $\phi = 0^\circ$, $H_\theta = 0.0$, $H_\phi = 1.0$; (a) $\text{Re}(J_s)$, (b) $\text{Im}(J_s)$, (c) $\text{Re}(J_y)$, (d) $\text{Im}(J_y)$. The wire current is shown in Figure G.5.	137

<u>Figure</u>	<u>Page</u>
G.5 Current induced on a wire near a square plate, $S_x = 0.5\lambda$, $Y_d = 0.5\lambda$, $L = 1.0\lambda$, $a = .001\lambda$, $\bar{r}_c = (-0.125\lambda, -0.125\lambda, 0.525\lambda)$, $\hat{\lambda} = (0.0, 0.0, 1.0)$, $\theta = 90^\circ$, $\phi = 0^\circ$, $H_\theta = 0.0$, $H_\phi = 1.0$. The plate current is shown in Figure G.4.	138
G.6 Current induced on a square plate near a wire, $S_x = 0.5\lambda$, $Y_d = 0.5\lambda$, $L = 0.5\lambda$, $a = .001\lambda$, $\bar{r}_c = (-0.125\lambda, 0.0, 0.1\lambda)$, $\hat{\lambda} = (0.0, 1.0, 0.0)$, $\theta = 0^\circ$, $\phi = 0^\circ$, $H_\theta = 0.0$, $H_\phi = -1.0$; (a) $\text{Re}(J_s)$, (b) $\text{Im}(J_s)$, (c) $\text{Re}(J_y)$, (d) $\text{Im}(J_y)$. The wire current is shown in Figure G.7.	140
G.7 Current induced on a wire near a square plate, $S_x = 0.5\lambda$, $Y_d = 0.5\lambda$, $L = 0.5\lambda$, $a = .001\lambda$, $\bar{r}_c = (-0.125\lambda, 0.0, 0.1\lambda)$, $\hat{\lambda} = (0.0, 1.0, 0.0)$, $\theta = 0^\circ$, $\phi = 0^\circ$, $H_\theta = 0.0$, $H_\phi = -1.0$. The plate current is shown in Figure G.6.	141

I. INTRODUCTION

This report considers the numerical solution of scattering by a bent rectangular plate configuration. The formulation is based on the electric field integral equation for the induced current on the plate structure. The method of moments [1] is used to obtain a numerical solution for the current, from which all other scattered field quantities can be derived.

Previous approaches to solving for currents on fiat rectangular plate structures [2] or their Babinet equivalents, rectangular apertures in an infinite ground plane [3], suffered from slow convergence and from extremely complex formulations. During the course of this study, it was found that most of these difficulties can be overcome by a judicious choice of both the current representation and the numerical treatment of the derivatives in the electric field equation. The resulting technique is simple and efficient to apply and appears to be generalizable, with these same advantages, to treating arbitrary surfaces.

It may at first seem unusual in a report of this nature to include two chapters on scattering by infinite strips with both TE and TM illumination. However, during the course of this investigation, the authors found themselves repeatedly

returning to these problems to test their hypotheses and to compare various numerical treatments. Basically, the two strip problems contain all the same difficulties as the plate problem except for the fact that the two problems are uncoupled. Thus the numerical treatment of the plate edges, the bend, and the handling of the derivatives in the electric field integral equation have all resulted from extensive testing on strips, where the flexibility in the number of unknowns that can be used allows one to easily check convergence, dependence on subdomain size, and so on. Space prevents us from documenting many of these "test runs," but it can be said that the sample results shown in Sections II and III are quite representative of results obtained for many different combinations of frequency, bend location, bend angle, and angle of incidence.

Such extensive numerical experimentation for the plate has not been possible because of computer storage and time limitations. However, when it has been possible to do limited testing, the proposed numerical method has been observed to be extremely stable, quickly convergent, and to converge to currents which are physically reasonable.

Section IV discusses the numerical formulation for the bent plate structure and Section V shows extensive results for the current distributions on a flat and bent plate for ... frequencies and several different angles of incidence.

Several appendices are included which discuss ancillary issues, various aspects of the numerical procedure, and extensions of the method.

III. NUMERICAL SOLUTION PROCEDURE FOR A BENT STRIP WITH TRANSVERSE MAGNETIC ILLUMINATION

In this section an integral equation is formulated and the moment method is applied to obtain a numerical solution for the problem of TM plane wave scattering by a bent strip. Effects of the edge conditions, the bend, and abrupt changes in subdomain size on the numerical results are discussed. Some representative data for currents on strips of various configurations and illuminations are given.

Formulation of the Integral Equation

Consider a conducting strip, infinite in the z -dimension and bent at an angle α , as shown in Figure 2.1. A plane wave with only a z -component of electric field is incident in the x - y plane. The incident field is thus transverse magnetic (TM) to the z -axis. The corresponding scattered field is also TM and the surface current induced on the strip flows only in the z -direction. The surface current produces a scattered vector potential

$$A_z(\bar{\rho}) = \frac{\mu}{4j} \int_{\text{strip}} J_z(s') H_0^{(2)}(k|\bar{\rho}-\bar{s}'|) ds' \quad (2.1)$$

where μ is the permeability of free space, k is the wave-number, J_z is the z -directed surface current density on the strip, and $H_0^{(2)}$ is the Hankel function of second kind, zero

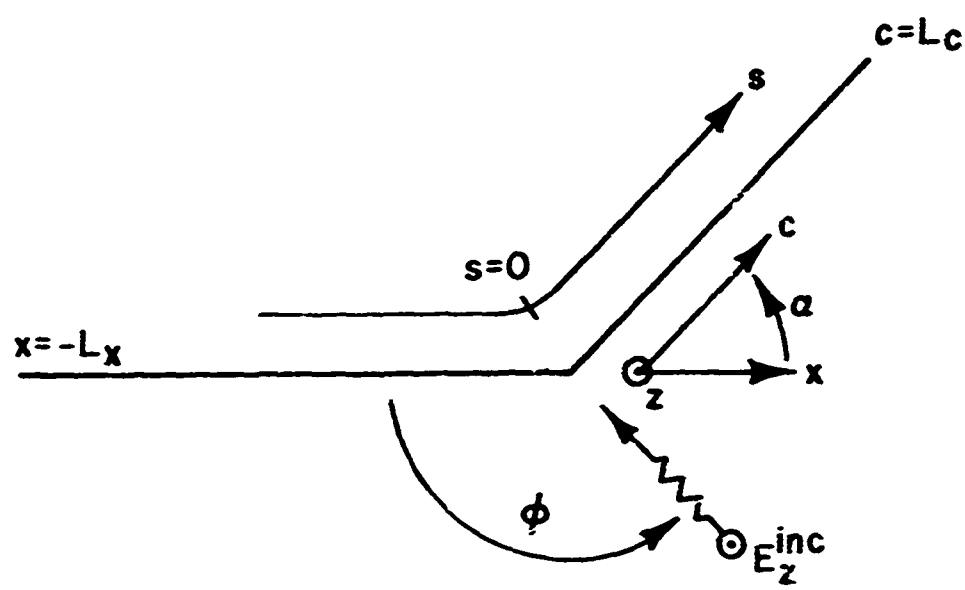


Figure 2.1. Strip configuration for TM illumination.

order. Requiring the z-component of the electric field to vanish on the strip surface results in the integral equation

$$-E_z^{\text{inc}}(\bar{\rho}) = -j\omega A_z(\bar{\rho}), \quad \bar{\rho} = s\hat{s}. \quad (2.2)$$

For a numerical solution of (2.2), we define N_x unit pulse functions along the portion of the strip on the x-axis and N_c unit pulse functions along the c-axis portion. These sets of pulse functions are of widths

$$\Delta x = \frac{L_x}{N_x}, \quad (2.3a)$$

and

$$\Delta c = \frac{L_c}{N_c}, \quad (2.3b)$$

respectively. There is a total of $N = N_x + N_c$ pulse functions. Thus the current may be approximately represented in the pulse basis as (Figure 2.2)

$$J_z(\bar{\rho}) \approx \sum_{n=1}^N J_n p_n(\bar{\rho}) \quad (2.4)$$

where

$$p_n(\bar{\rho}) = \begin{cases} 1 & , \quad s_n - \frac{\Delta s_n}{2} \leq s \leq s_n + \frac{\Delta s_n}{2} \\ 0 & , \quad \text{otherwise} \end{cases} \quad (2.5)$$

and

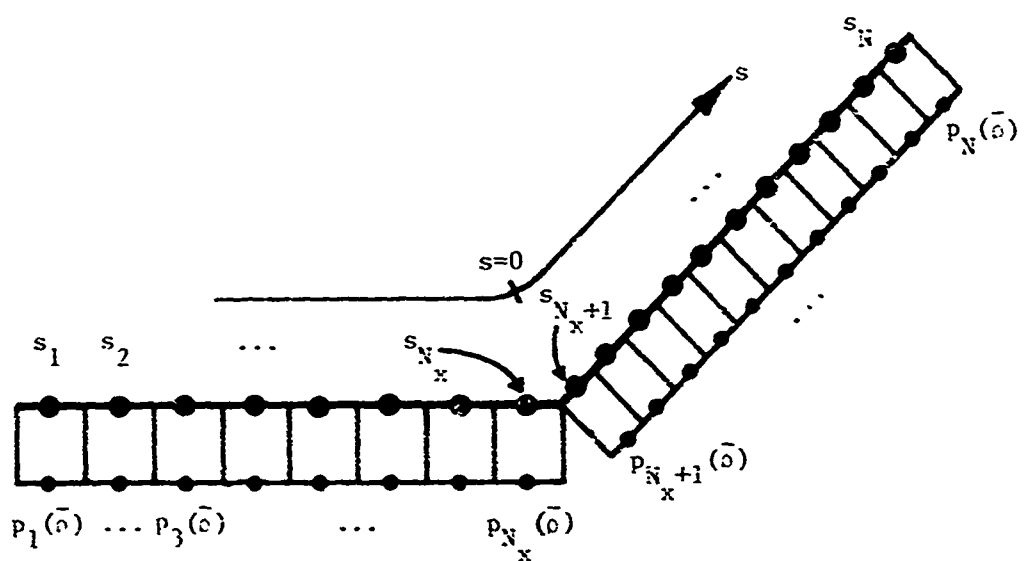


Figure 2.2. Pulse basis functions and match points for the TM illuminated bent strip.

$$s_n = \begin{cases} -L_x + (n-\frac{1}{2})\Delta x, & 1 \leq n \leq N_x \\ (n - N_x - \frac{1}{2})\Delta c, & N_x + 1 \leq n \leq N \end{cases},$$

$$\Delta s_n = \begin{cases} \Delta x, & 1 \leq n \leq N_x \\ \Delta c, & N_x + 1 \leq n \leq N \end{cases}.$$

Substituting (2.4) into (2.2) and requiring equality in (2.2) at $s = s_m$, $m = 1, \dots, N$, one has

$$-E_z^{inc}(\hat{s}s_m) = -j\omega A_z(\hat{s}s_m), \quad (2.6)$$

$m = 1, 2, \dots, N$

where

$$A_z(\hat{s}s_m) = \frac{u}{4j} \left[\sum_{n=1}^{N_x} J_n \psi_{sx} \left(\hat{s}s_m; s_n - \frac{\Delta x}{2}, s_n + \frac{\Delta x}{2} \right) \right. \\ \left. + \sum_{n=N_x+1}^N J_n \psi_{cc} \left(\hat{s}s_m; s_n - \frac{\Delta c}{2}, s_n + \frac{\Delta c}{2} \right) \right] \quad (2.7)$$

and the ψ functions are defined as

$$\psi_{sx} = \begin{cases} \psi_{cx}, & s_m > 0 \\ \psi_{xx}, & s_m < 0 \end{cases} \quad (2.8a)$$

$$\psi_{sc} = \begin{cases} \psi_{xc} & , s_m < 0 \\ \psi_{cc} & , s_m > 0 \end{cases} . \quad (2.8b)$$

The functions on the right hand side of (2.8) are defined as

$$\psi_{pq}(ss; s_1, s_2) = \int_{s_1}^{s_2} h_0^{(2)}(k R_{pq}) ds' , \quad (2.9)$$

$p = x$ or c ,

$q = x$ or c ,

where

$$R_{xx} = |x-x'| \quad (2.10a)$$

$$R_{xc} = \left[(x - c' \cos \alpha)^2 + c'^2 \sin^2 \alpha \right]^{\frac{1}{2}} \quad (2.10b)$$

$$R_{cx} = \left[(c \cos \alpha - x')^2 + c^2 \sin^2 \alpha \right]^{\frac{1}{2}} \quad (2.10c)$$

$$R_{cc} = |c-c'| \quad (2.10d)$$

Equations (2.6) and (2.7) constitute a linear system of equations which can be succinctly written in matrix form as

$$ZI = V \quad (2.11)$$

where

$$V = \begin{bmatrix} -E_z^{inc}(\hat{s}s_1) \Delta x \\ \vdots \\ -E_z^{inc}(\hat{s}s_{N_x}) \Delta x \\ -E_z^{inc}(\hat{s}s_{N_x+1}) \Delta c \\ \vdots \\ -E_z^{inc}(\hat{s}s_N) \Delta c \end{bmatrix} \quad (2.12)$$

$$I = \begin{bmatrix} J_1 \\ \vdots \\ \vdots \\ J_N \end{bmatrix} \quad (2.13)$$

and the elements of Z can be determined from (2.6) and (2.7).

Solution of the simultaneous equations (2.11) determines the coefficients of the basis representation (2.4).

Effect of the Edge Condition on Numerical Solutions

The behavior of current flow near a conducting edge is determined by the so-called edge condition [4]. Edge conditions for a bent strip and plate are summarized in Appendix A. In the TM case, the current flow is parallel to the strip edges and the edge condition requires that the current be singular there. Near the left and right hand edges of the strip in Figure 2.1, the current varies as $|L_x + s|^{-\frac{1}{2}}$ and $|L_c - s|^{-\frac{1}{2}}$, respectively. At lower frequencies, this edge behavior is dominant over the entire strip, while at higher frequencies, the behavior is confined more closely to the edges of the strip.

as Figures 2.3 and 2.4 illustrate for a flat strip ($a = 0$). In [5], it is shown that the pulse basis set of Figure 2.2 enjoys a number of advantages in a numerical determination of the current. First, the match points are logically chosen at the center of the pulses so that fields are not evaluated directly at the edges. In other schemes where match points are located at the edges (such as with half-pulses or half-triangles at the edges), it has been found that anomalous behavior in the current distribution at the edges results and that the anomalies in such cases can be alleviated only by permitting the edge current expansion functions to contain the correct edge singularity [5]. It seems to be a general rule with pulse basis functions that one should always avoid computing the vector (scalar) potential at a point where the associated current (charge) is known to be singular. In a pulse basis solution, the pulses at the edge tend to represent numerically the correct average current contained in the edge subdomains. While the magnitude of the average current in edge subdomains is typically larger than the actual current at the midpoint of the edge pulses, the numerically derived current at the edge can be corrected a posteriori [5].

Effect of the Bend on Numerical Solutions

The bend in the strip also causes singularities in the TM surface currents. As discussed in Appendix B, the surface current found in a numerical solution is the sum of the actual surface currents which flow on opposite sides of the strip.

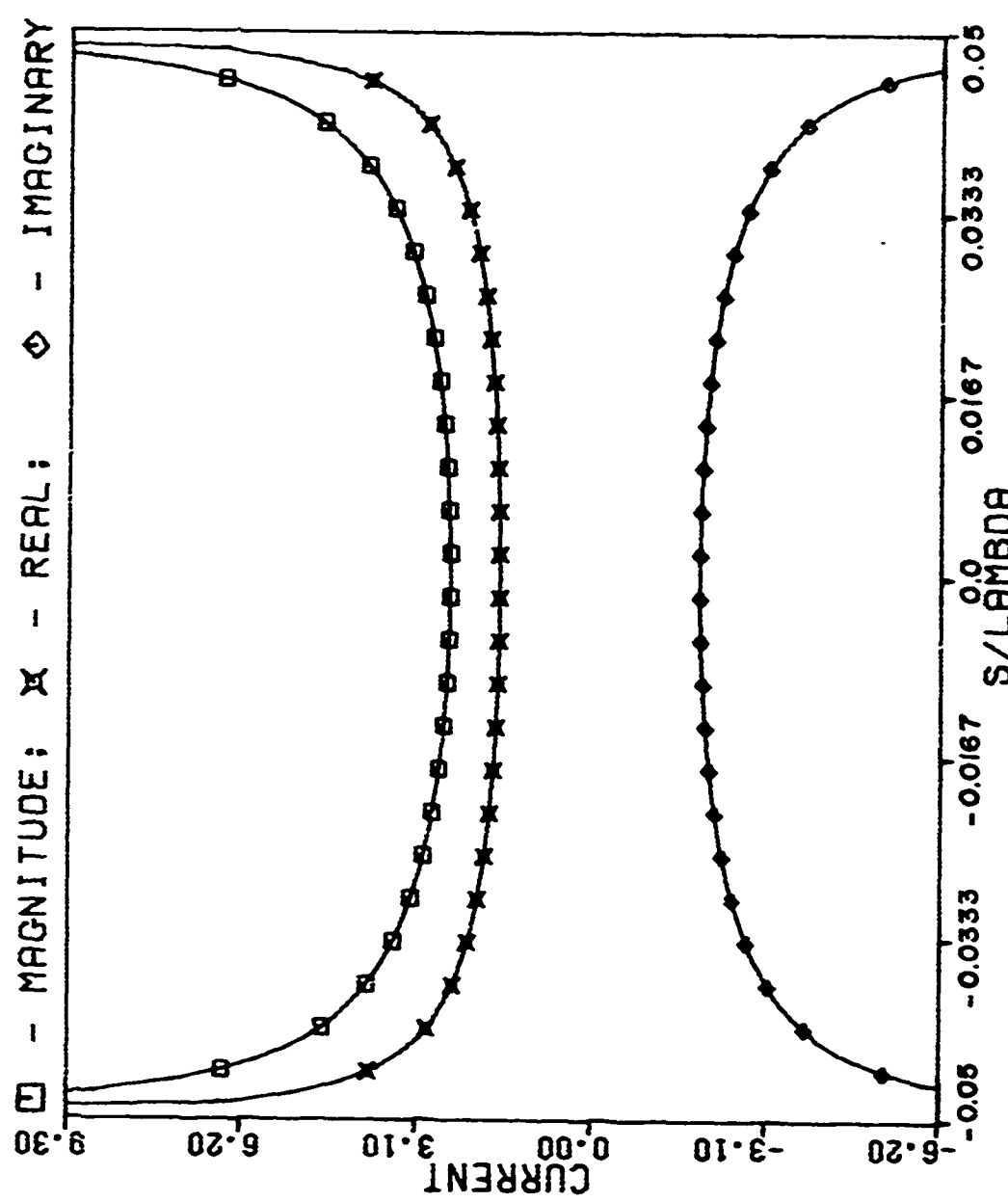


Figure 2.3. Induced current on a 0.1λ strip illuminated by a normally incident TM plane wave.

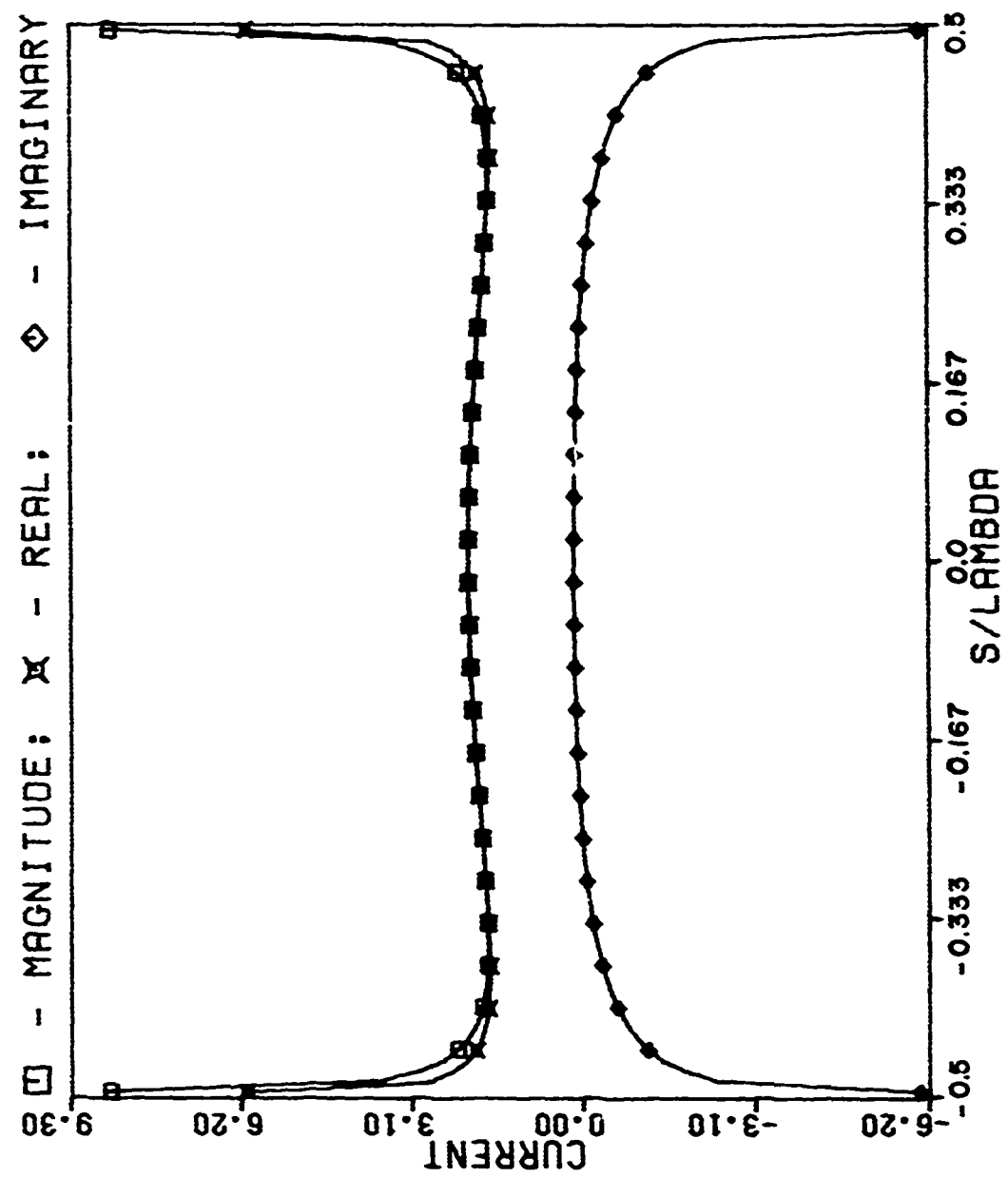


Figure 2.4. Induced current on a 1.0λ strip illuminated by a normally incident plane wave.

In the neighborhood of the bend the surface current must behave like that on an infinite wedge of the same wedge angle; but this behavior is different for an interior and an exterior wedge angle. Only the exterior wedge angle causes singular currents, however, so that the singularity in the current can be determined from the exterior wedge angle. In terms of Figure 2.1, the current in the neighborhood of the edge behaves like (see Appendix A)

$$J(s) \xrightarrow[s \rightarrow 0]{} A|s|^{-\frac{|\alpha|}{\pi+|\alpha|}}. \quad (2.14)$$

While a detailed investigation to check that (2.14) is satisfied in a numerical sense has not been carried out, it is verified in Figures 2.5, 2.6, and 2.7 that increasing the bend angle does indeed cause the singularity to become more pronounced as (2.14) suggests. Furthermore, it is seen that the behavior on either side of the bend can be very different. For this reason and for reasons similar to those mentioned in connection with edges, it appears that the pulses should indeed be placed on either side of the bend with match points at their centers, away from the bend itself. Splitting a pulse around the bend would be expected to cause the same anomalies in the current distribution as is found when match points are placed at edges.

Effect of Differing Subdomain Sizes on Numerical Solutions

In many numerical procedures, it has been observed that anomalies in the current distribution result when abrupt changes

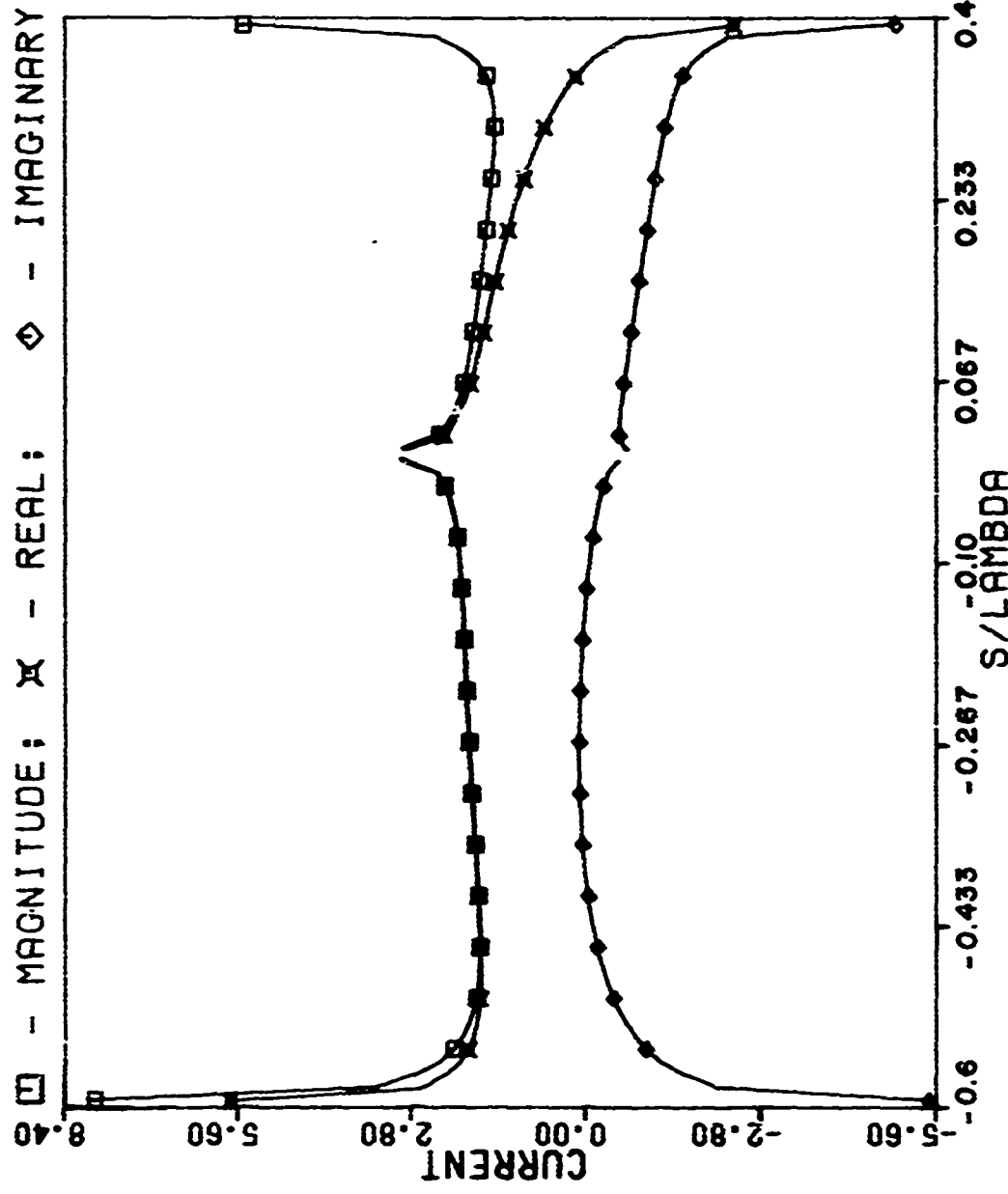


Figure 2.5. Induced current on a 1.0λ strip bent 30° at $s/\lambda = 0$ and illuminated by a TM plane wave normally incident to the section of the strip $s/\lambda < 0$.

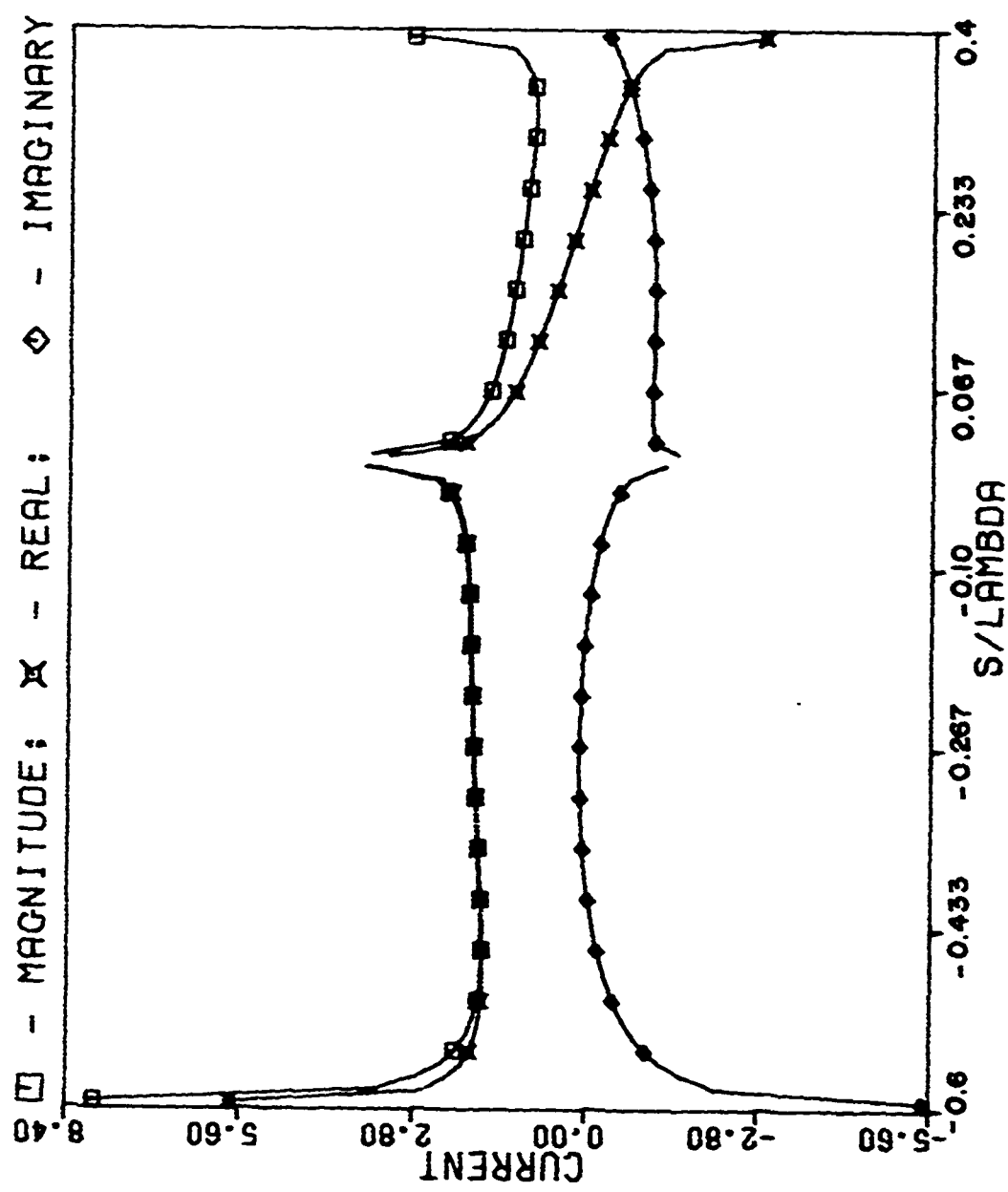


Figure 2.6. Induced current on a 1.0λ strip bent 60° at $s/\lambda = 0$ and illuminated by a TM plane wave normally incident to the section of the strip $s/\lambda < 0$.

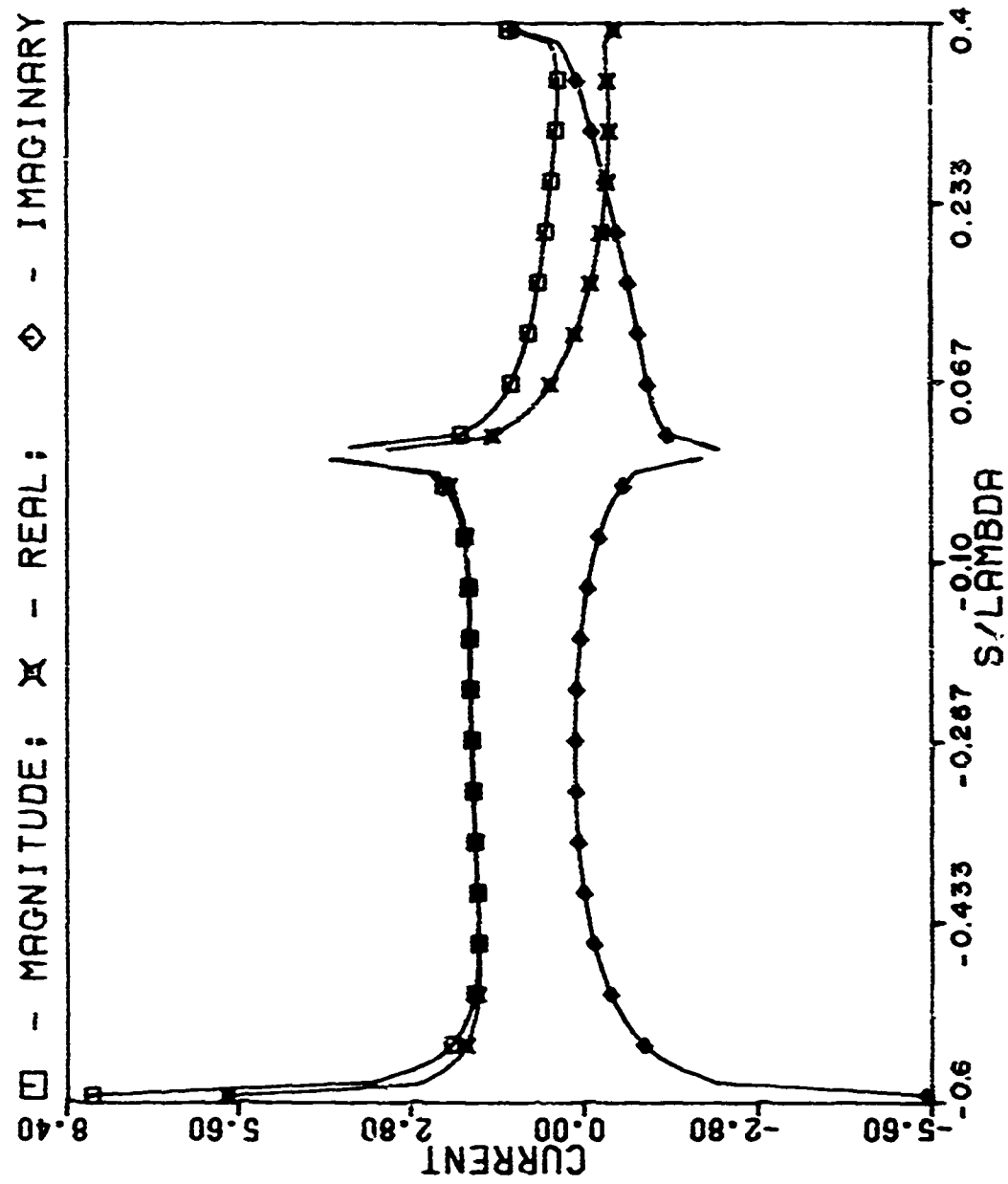


Figure 2.7. Induced current on a 1.0λ strip bent 90° at $s/\lambda = 0$ and illuminated by a TM plane wave normally incident to the section of the strip $s/\lambda < 0$.

in subdomain sizes are made. In strip problems, enough subdomains can be used such that if unequal subdomain sizes are necessary on opposite sides of the bend, the differences in subdomain sizes can be made rather small. In the plate problem to be considered, however, where the number of subdomains in each dimension is severely limited, it may turn out that in order to adequately sample currents on opposite sides of the bend, drastic differences in subdomain sizes must be used. To investigate the dependence of the numerical solution on abrupt changes in subdomain sizes, Figures 2.8 and 2.9 show the effect on the solution of changes in subdomain size on a flat strip where the change is made in the central portion and near an edge of the strip, respectively. It is seen that only a very small anomaly occurs when the change is made near an edge, where the slope of the true current is the greatest. This anomaly is so small as to be of no concern in a numerical solution. This independence of subdomain size has been verified for a wide range of strip sizes and incidence angles, provided that one always begins with a sufficient number of pulses (and match points) that the variation of the incident field is adequately sampled. Figure 2.10 shows that changing subdomain size at the bend also has no appreciable effect, except that the currents next to the bend, which approximate the average current in their respective subdomains, always appear to be slightly too large in magnitude.

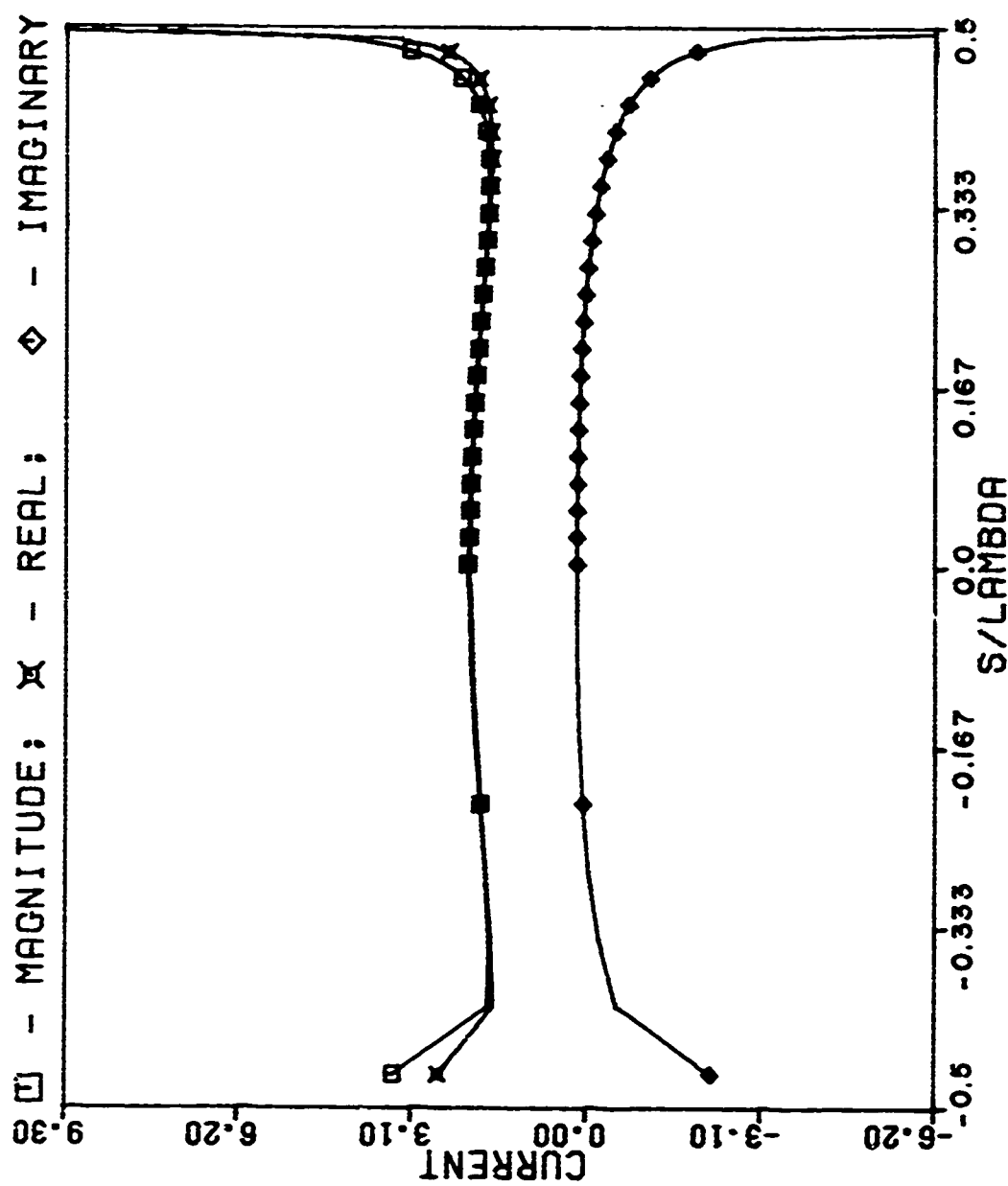


Figure 2.8. Induced current on a 1.0λ strip illuminated by a normally incident TM plane wave. Subdomain size changes at $s/\lambda = 0$ by a ratio of 10 to 1. (Compare with Figure 2.4.)

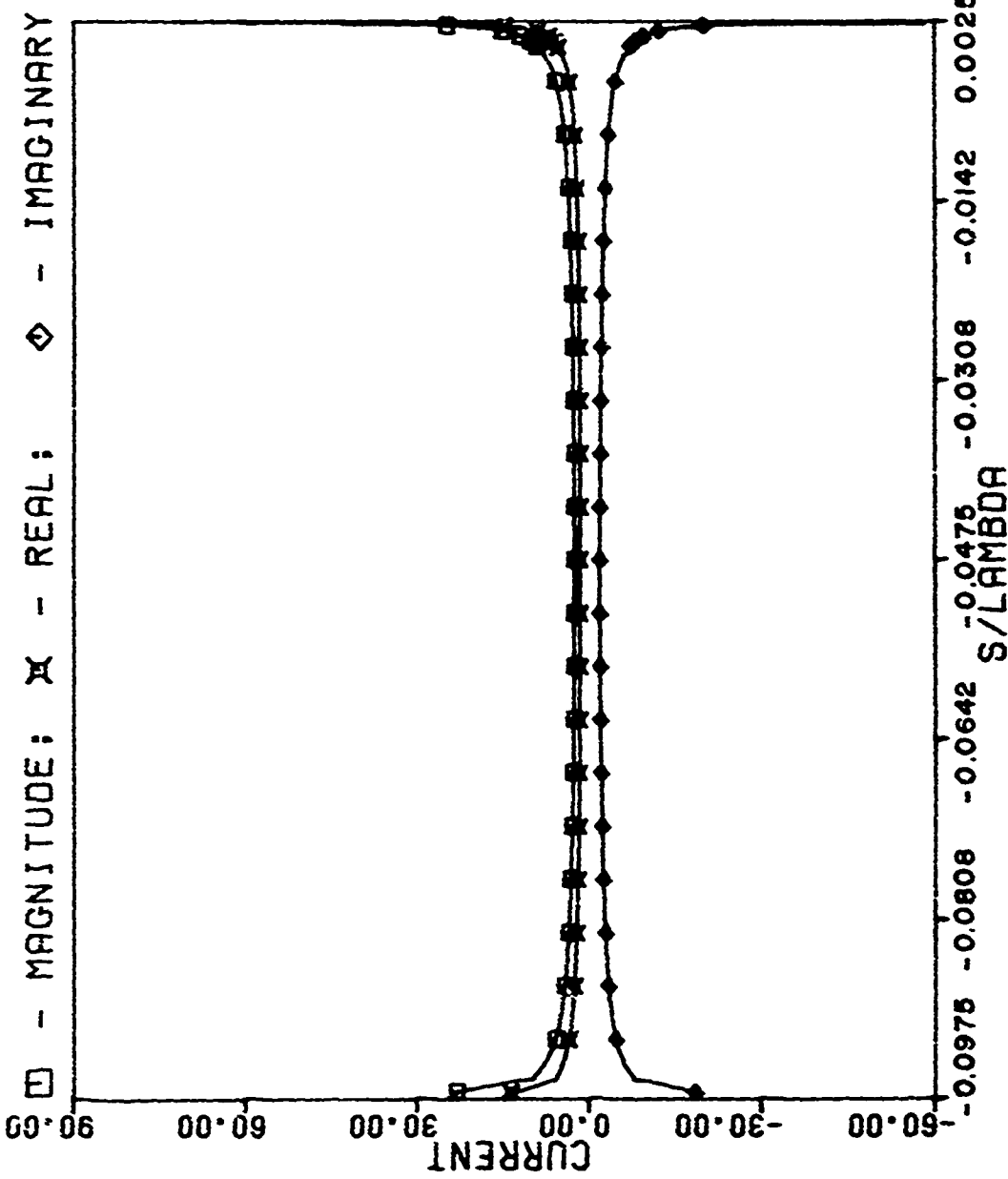


Figure 2.9. Induced current on a 1.0λ strip [1] illuminated by a normally incident TM plane wave. Subdomain size changes at $s/\lambda = 0$ by a ratio of 10 to 1.

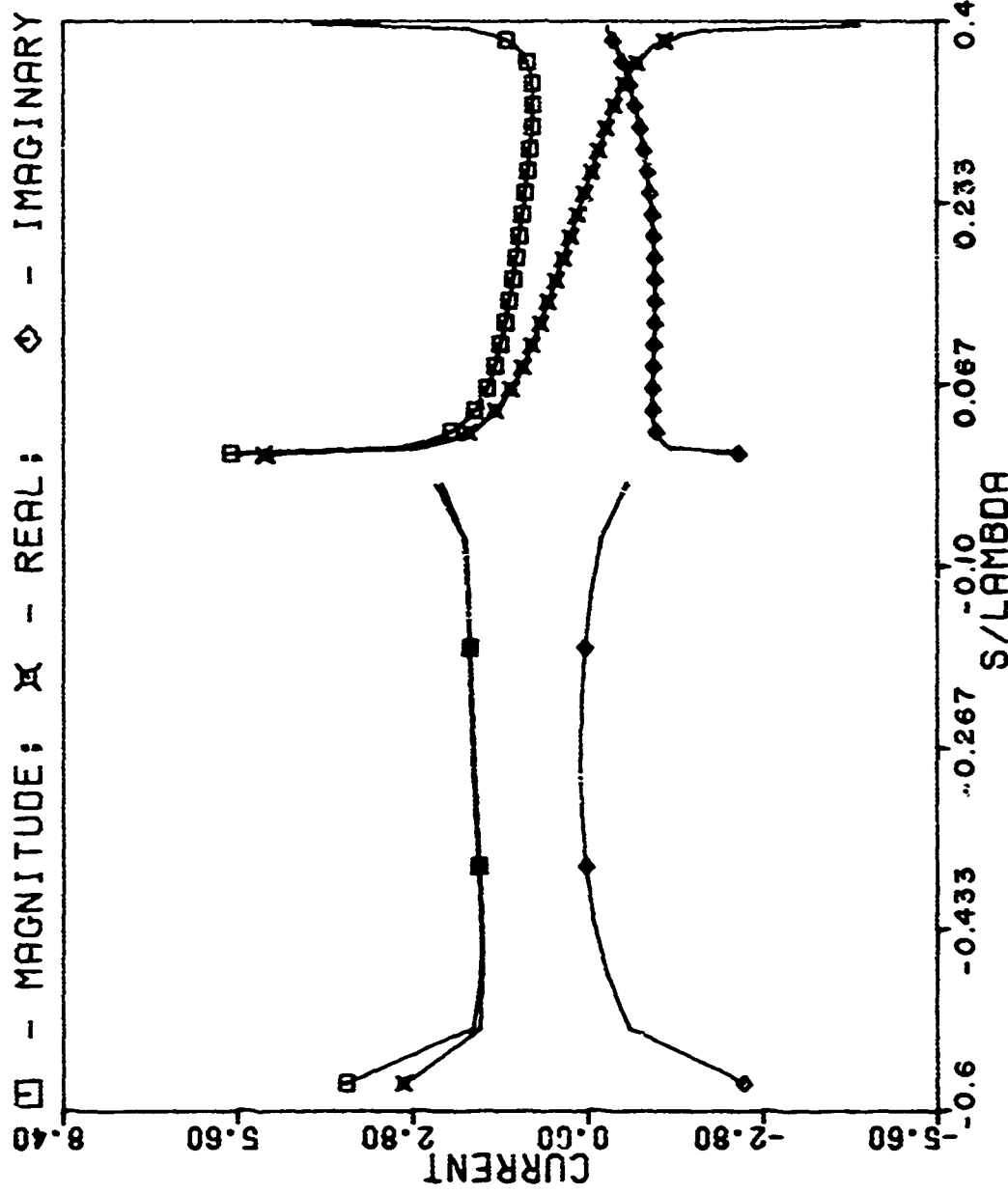


Figure 2.10. Induced current on a 1.0λ strip bent 60° at $s/\lambda = 0$ and illuminated by a TM plane wave normally incident to the section of the strip $s/\lambda < 0$. Subdomain size changes at $s/\lambda = 0$ by a ratio of 10 to 1. (Compare with Figure 2.6.)

III. NUMERICAL SOLUTION PROCEDURE FOR A BENT STRIP WITH TRANSVERSE ELECTRIC ILLUMINATION

In this section an integral equation is formulated and the moment method is applied to obtain a numerical solution for the problem of TE plane wave scattering by a bent strip. The placement of the current subdomains at the edges and the effects of the bend and abrupt changes in subdomain size on the numerical results are discussed. Some representative data for TE currents on strips of various configurations and illuminations are given.

Formulation of the Integral Equation

Consider a conducting strip, infinite in the z-dimension and bent at an angle α , as shown in Figure 3.1. A plane wave with only a z-component of magnetic field is incident along the x-y plane. The incident field is thus transverse electric (TE) to the z-axis. The corresponding scattered field is also TE and the surface current induced on the strip flows only in the s-direction. Since the total tangential electric field must vanish on the strip surface, we have

$$-\bar{\mathbf{E}}^{\text{inc}}(\bar{o}) \cdot \hat{s} = \left[-j\omega\bar{A}(\bar{o}) - \nabla\phi(\bar{o}) \right] \cdot \hat{s} , \quad (3.1)$$
$$\bar{o} = s\hat{s} .$$

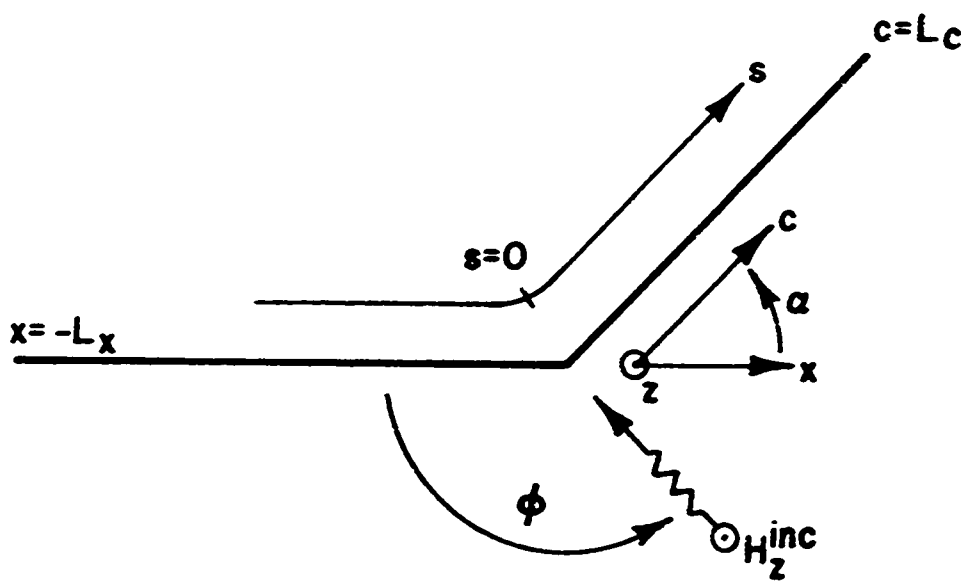


Figure 3.1. Strip configuration for TE illumination.

The vector and scalar potentials in (3.1) are defined by

$$\bar{A}(\bar{\rho}) = \frac{\mu}{4\pi} \int_{\text{strip}} \bar{J}(\bar{\rho}') H_0^{(2)}(k|\bar{\rho}-\bar{\rho}'|) ds' \quad (3.2)$$

and

$$\phi(\bar{\rho}) = \frac{1}{4\pi\epsilon} \int_{\text{strip}} \rho(\bar{\rho}') H_0^{(2)}(k|\bar{\rho}-\bar{\rho}'|) ds' , \quad (3.3)$$

respectively, where $\bar{J}(\bar{\rho}) = \hat{s} J(\bar{\rho})$ is the s -directed current density and ρ is the surface charge density which is related to the current through the equation of continuity,

$$\rho(\bar{\rho}) = \frac{i}{\omega} \frac{dJ(\bar{\rho})}{ds} . \quad (3.4)$$

To effect a numerical solution of (3.1), we divide both straight segments of the strip into subdomains as in Figure 3.2. Pulse functions representing the current are defined such that half pulses represent the current on either side of the bend and at the edges where the current vanishes. The half pulses at the edges improve the convergence of the solution (see the following subsection) while the half pulses on either side of the bend have identical magnitudes, thereby enforcing continuity of the current flowing around the bend. Thus the current is expanded as

$$J(\bar{\rho}) = \sum_{n=1}^N J_n p_n(\bar{\rho}) \quad (3.5)$$

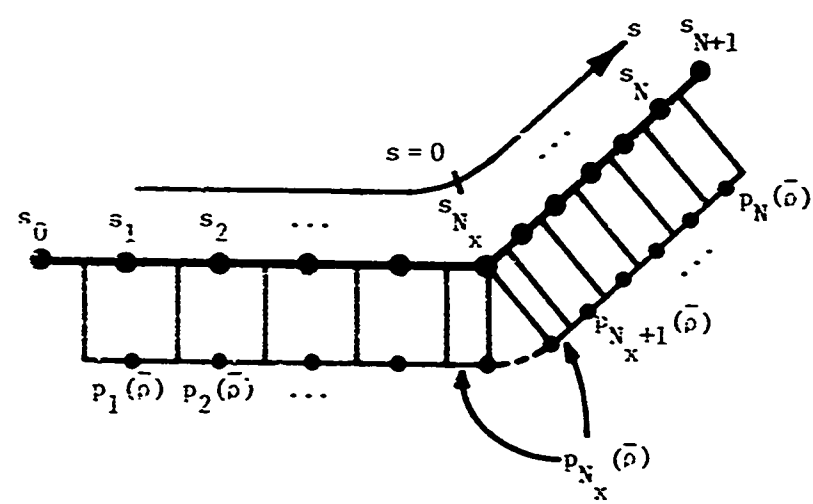


Figure 3.2. Pulse basis functions and match points for the TM illuminated bent strip.

where

$$p_n(\bar{\rho}) = \begin{cases} 1, & \frac{s_n + s_{n-1}}{2} \leq s \leq \frac{s_n + s_{n+1}}{2} \\ 0, & \text{otherwise} \end{cases} \quad (3.6)$$

and $\bar{\rho} = \hat{ss}$. The coordinate quantities in (3.6) are

$$s_n = \begin{cases} -L_x + n\Delta x, & 0 \leq n \leq N_x \\ (n-N_x)\Delta c, & N_x + 1 \leq n \leq N+1 \end{cases} \quad (3.7)$$

where N_x is the number of non-zero current pulses (including the current at the bend) along the x-directed portion of the strip (see Figure 3.2). The pulse widths for x-directed and c-directed currents are

$$\Delta x = \frac{L}{N_x} \quad (3.8a)$$

$$\Delta c = \frac{c}{N - N_x + 1}, \quad (3.8b)$$

respectively. There is a total of N unknown currents represented by pulse functions. Substitution of (3.5) into (3.2) permits the computation of the vector potential. To compute the scalar potential, we use a finite difference approximation of the continuity equation to obtain a pulse representation of the charge density (Figure 3.3):

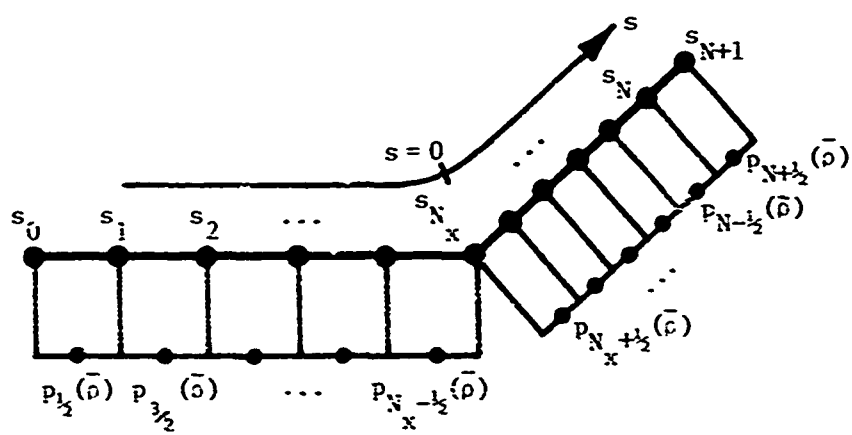


Figure 3.3. Pulse basis functions for the charge on the TE illuminated bent strip.

$$\rho(\bar{\phi}) = \frac{j}{\omega} \sum_{n=1}^{N+1} \frac{j_n - j_{n-1}}{\Delta s_n} p_{n-\frac{1}{2}}(\bar{\phi}) \quad (3.9)$$

where

$$\Delta s_n = \begin{cases} \Delta x, & n \leq N_x \\ \Delta c, & n \geq N_x + 1 \end{cases} \quad (3.10)$$

and

$$p_{n-\frac{1}{2}}(\bar{\phi}) = \begin{cases} 1, & s_n \leq s \leq s_{n-1} \\ 0, & \text{otherwise} \end{cases} \quad (3.11)$$

In writing (3.9), we assume that

$$j_0 \equiv j_{N+1} \equiv 0. \quad (3.12)$$

Equation (3.1) is enforced at the centers of the current sub-domains (Figure 3.2) on the straight segments of the strip. Replacing the term involving the derivative of the scalar potential by a finite difference approximation, we obtain,

$$\begin{aligned} -\hat{E}_x^{\text{inc}}(xs_m)\Delta x &= -j\omega A_x(xs_m)\Delta x - \phi \left[\hat{x} \left(s_m + \frac{\Delta x}{2} \right) \right] \\ &\quad + \phi \left[\hat{x} \left(s_m - \frac{\Delta x}{2} \right) \right], \\ m &= 1, 2, \dots, N_x - 1 \quad (3.13a) \end{aligned}$$

$$-\hat{E}_c^{\text{inc}}(\hat{c}s_m)\Delta c = -j\omega A_c(\hat{c}s_m)\Delta c - \phi \left[\hat{c} \left(s_m + \frac{\Delta c}{2} \right) \right] \\ + \phi \left[\hat{c} \left(s_m - \frac{\Delta c}{2} \right) \right] ,$$

$$m = N_x + 1, N_x + 2, \dots, N \quad (3.13b)$$

At the bend, we employ a backwards difference approximation to the derivative of the scalar potential at $s = 0^-$ (on the left side of the bend in Figure 3.2) and a corresponding forward difference approximation at $s = 0^+$ (on the right side of the bend in Figure 3.2):

$$-\hat{E}_x^{\text{inc}}(\bar{0}) = -j\omega A_x(\bar{0}) - \frac{\phi(\bar{0}) - \phi\left(-\hat{x} \frac{\Delta x}{2}\right)}{\Delta x/2} , \quad (3.14a)$$

$$-\hat{E}_c^{\text{inc}}(\bar{0}) = -j\omega A_c(\bar{0}) - \frac{\phi\left(\hat{c} \frac{\Delta c}{2}\right) - \phi(\bar{0})}{\Delta c/2} . \quad (3.14b)$$

Only one equation is required at the bend so that some appropriate combination of (3.14a) and (3.14b) must be taken. Heretofore, we have successfully avoided evaluating any potentials due to singular quantities directly at the point of the singularity (see Section II and reference [5]). Equations (3.14a) and (3.14b), however, seem to require the evaluation of the scalar potential directly at the bend where the charge density is, in general, infinite. To avoid any difficulty with this questionable procedure, we merely multiply (3.14a) by $\Delta x/2$ and (3.14b) by $\Delta c/2$ and add the resulting equations, obtaining

$$-\left(\frac{E_x^{inc}(\bar{0})\Delta x + E_c^{inc}(\bar{0})\Delta c}{2}\right) = -j\omega \left(\frac{A_x(\bar{0})\Delta x + A_c(\bar{0})\Delta c}{2}\right)$$

$$-\phi\left(\hat{c} \frac{\Delta c}{2}\right) + \phi\left(-\hat{x} \frac{\Delta x}{2}\right). \quad (3.15)$$

In this equation for the match point at the bend, the scalar potential at the bend is never needed. The use of (3.15) at the bend is an important development because it ensures that (1) no potential functions are evaluated at singularities of the corresponding source quantities, (2) it quite properly gives more weight to the longer subdomain on either side of the bend, and (3) it reduces to (3.13) when the bend angle is zero and $\Delta x = \Delta c$. It will also be demonstrated in a following subsection that the use of (3.15) at the bend yields numerical results which are relatively independent of the subdomain size.

The vector and scalar potential terms can be written more explicitly by introducing the vectors

$$\vec{\phi}_x = x\hat{x} \quad (3.16a)$$

$$\vec{\phi}_c = c\hat{c} \quad (3.16b)$$

and a rather unconventional but convenient definition for the Kronecker delta,

$$\delta_{st} = \begin{cases} 1, & \text{if } s = t \\ 0, & \text{if } s \neq t \end{cases}$$

where s and t are variable subscripts rather than integers.

The potentials are then written as

$$\begin{aligned}
A_p(\bar{\rho}_p) = & \frac{u}{4j} \left\{ \sum_{n=1}^{N_x-1} J_n \psi_{px}\left(\bar{\rho}_p; s_n - \frac{\Delta x}{2}, s_n + \frac{\Delta x}{2}\right) \left(\delta_{px} + \delta_{pc} \cos \alpha \right) \right. \\
& + J_{N_x} \left[\psi_{px}\left(\bar{\rho}_p; s_{N_x} - \frac{\Delta x}{2}, s_{N_x}\right) \left(\delta_{px} + \delta_{pc} \cos \alpha \right) \right. \\
& \left. \left. + \psi_{pc}\left(\bar{\rho}_p; s_{N_x}, s_{N_x} + \frac{\Delta c}{2}\right) \left(\delta_{pc} + \delta_{px} \cos \alpha \right) \right] \right\} \\
& + \sum_{n=N_x+1}^N J_n \psi_{pc}\left(\bar{\rho}_p; s_n - \frac{\Delta c}{2}, s_n + \frac{\Delta c}{2}\right) \left(\delta_{pc} + \delta_{px} \cos \alpha \right), \\
& p = x \text{ or } c \quad (3.17)
\end{aligned}$$

and

$$\begin{aligned}
\phi(\bar{\rho}_p) = & \frac{1}{4\omega\varepsilon} \left\{ \sum_{n=1}^{N_x} \left[\frac{J_n - J_{n-1}}{\Delta x} \right] \psi_{px}\left(\bar{\rho}_p; s_{n-1}, s_n\right) \right. \\
& \left. + \sum_{n=N_x+1}^{N+1} \left[\frac{J_n - J_{n-1}}{\Delta c} \right] \psi_{pc}\left(\bar{\rho}_p; s_{n-1}, s_n\right) \right\} \\
& p = x \text{ or } c \quad (3.18)
\end{aligned}$$

The functions ψ_{px} and ψ_{pc} are defined in (2.9) and (2.10).

Equations (3.13) and (3.15) together with (3.17) and (3.18) constitute a linear system of equations which can be succinctly written in matrix form as

$$ZI = V \quad (3.19)$$

where

$$V = \begin{bmatrix} -\epsilon_x^{inc} (\hat{s}s_1) \Delta x \\ \vdots \\ -\epsilon_x^{inc} (\hat{s}s_{N_x-1}) \Delta x \\ -k \left[\epsilon_x^{inc}(\bar{0}) \Delta x + \epsilon_c^{inc}(\bar{0}) \Delta c \right] \\ -\epsilon_c^{inc} (\hat{s}s_{N_x+1}) \Delta c \\ \vdots \\ -\epsilon_c^{inc} (\hat{s}s_N) \Delta c \end{bmatrix}, \quad (3.20)$$

$$I = \begin{bmatrix} J_1 \\ \vdots \\ J_N \end{bmatrix} \quad (3.21)$$

and the elements of Z can be determined from (3.13), (3.15), (3.17), and (3.18). Solution of the simultaneous equations (3.19) determines the coefficients in the basis representation for the current, Equation (3.5).

Effect of Placement of Edge Subdomains on Numerical Solutions

The proper placement of the end subdomains where one requires the current to vanish is critical for obtaining good convergence in numerical solutions. It has been found repeatedly for such problems, (i.e., scattering by wires

and TE strips) that requiring the current to vanish in the region within a half subdomain width (compared to the adjacent subdomain widths) of edges correctly models the actual electrical length of the structure. As an example, Figure 3.4 compares the convergence of the center current for a normally illuminated TE strip where the current is assumed to be zero within a half subdomain and within a full subdomain of the edge. The slow convergence that results when the current vanishes within a full subdomain of the edge is attributed to the fact that increasing the number of subdomains simultaneously appears to increase the electrical length of the strip. Hence it is the length, and not the numerical solution procedure, which is converging slowly.

Note also that the current tends to zero with an infinite slope at the edges. The edge condition (Appendix A) requires that the variation of the current near the left and right hand edges of the strip in Figure 3.1 be $|L_x + s|^{\frac{1}{2}}$ and $|L_c - s|^{\frac{1}{2}}$, respectively. At lower frequencies, this edge behavior influences the shape of the current over the entire strip, while at the higher frequencies, the edge behavior is confined more to the region near the edges.

Effect of the Bend on Numerical Solutions

The bend in the strip causes the current which flows around the bend to have an infinite slope, in general, at the bend. In Appendix B, it is shown that the surface current in a numerical solution is the vector sum of the actual

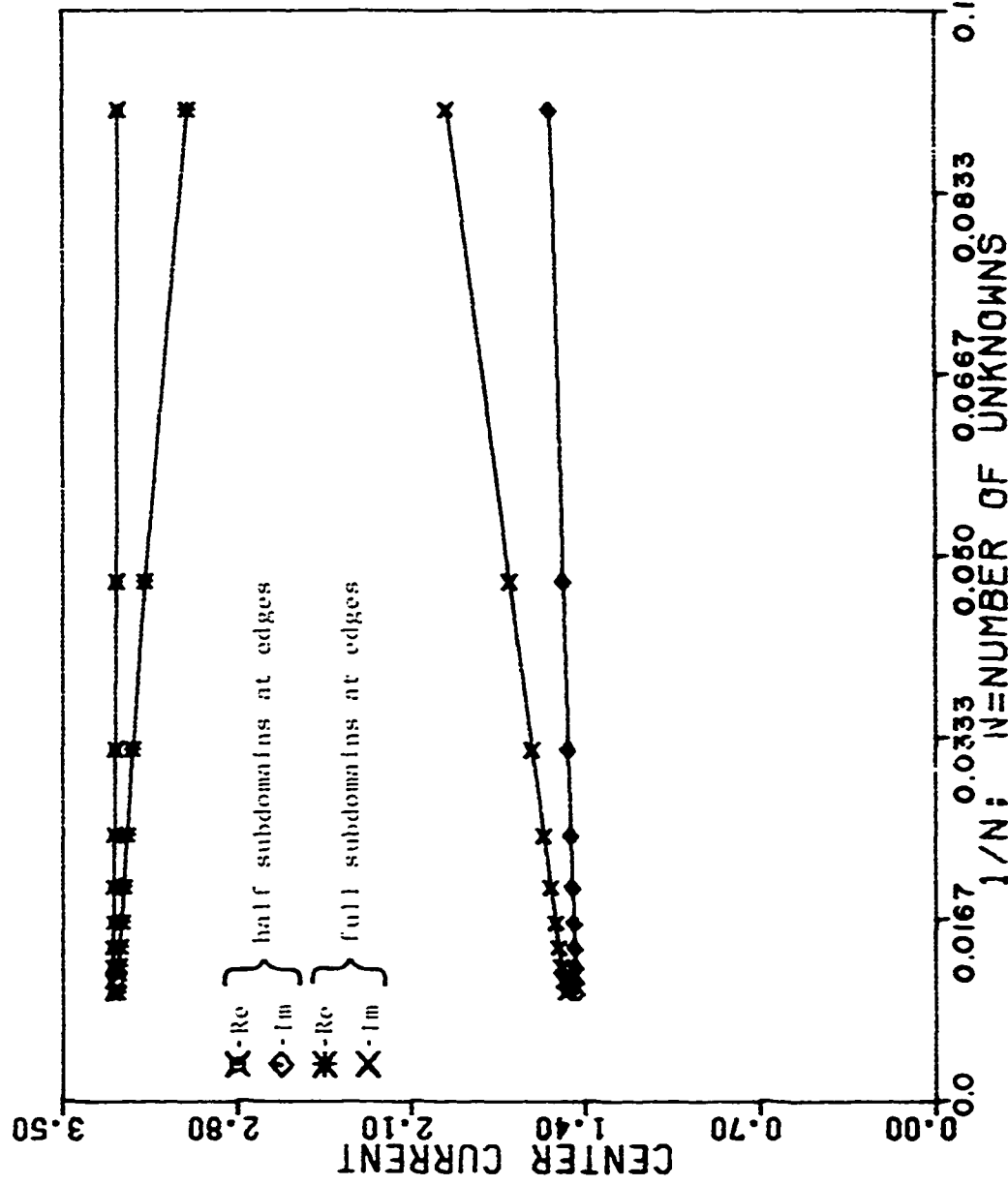


Figure 3.4. Comparison of convergence for a 0.5λ strip illuminated by a normally incident TE plane wave when full subdomains and half subdomains are used to represent the current at the edges.

surface currents which flow on opposite sides of the strip.

In the neighborhood of the bend, the variation of current near the bend must approach that of the current near the edge of an infinite wedge of the same angle. Since the variation of the current is more rapid on an exterior than on an interior wedge, the exterior wedge current will tend to provide the dominant behavior of the current at the bend, particularly when the interior is in the shadow region of the incident field. Thus the exterior current near the bend, from Appendix A, varies as

$$J(s) \xrightarrow[s \neq 0]{} A + B \operatorname{sgn}(s) |s|^{\frac{|\alpha|}{\pi+|\alpha|}} \quad (3.22)$$

where

$$\operatorname{sgn}(s) = \begin{cases} 1, & s > 0 \\ -1, & s < 0 \end{cases}$$

Figure 3.5 shows this type of behavior for current flowing around a 90° bend. As with the edge behavior, this condition becomes confined to a more limited region about the bend as the frequency increases.

Figure 3.6 shows the current c. a 90° bend for the case when the illumination is incident along the symmetry plane between the two symmetrical halves of the strip. Because of the symmetry in both the geometry and the incident field, the current must be symmetric about the bend and hence the second term in (3.22) must have a zero coefficient. One can

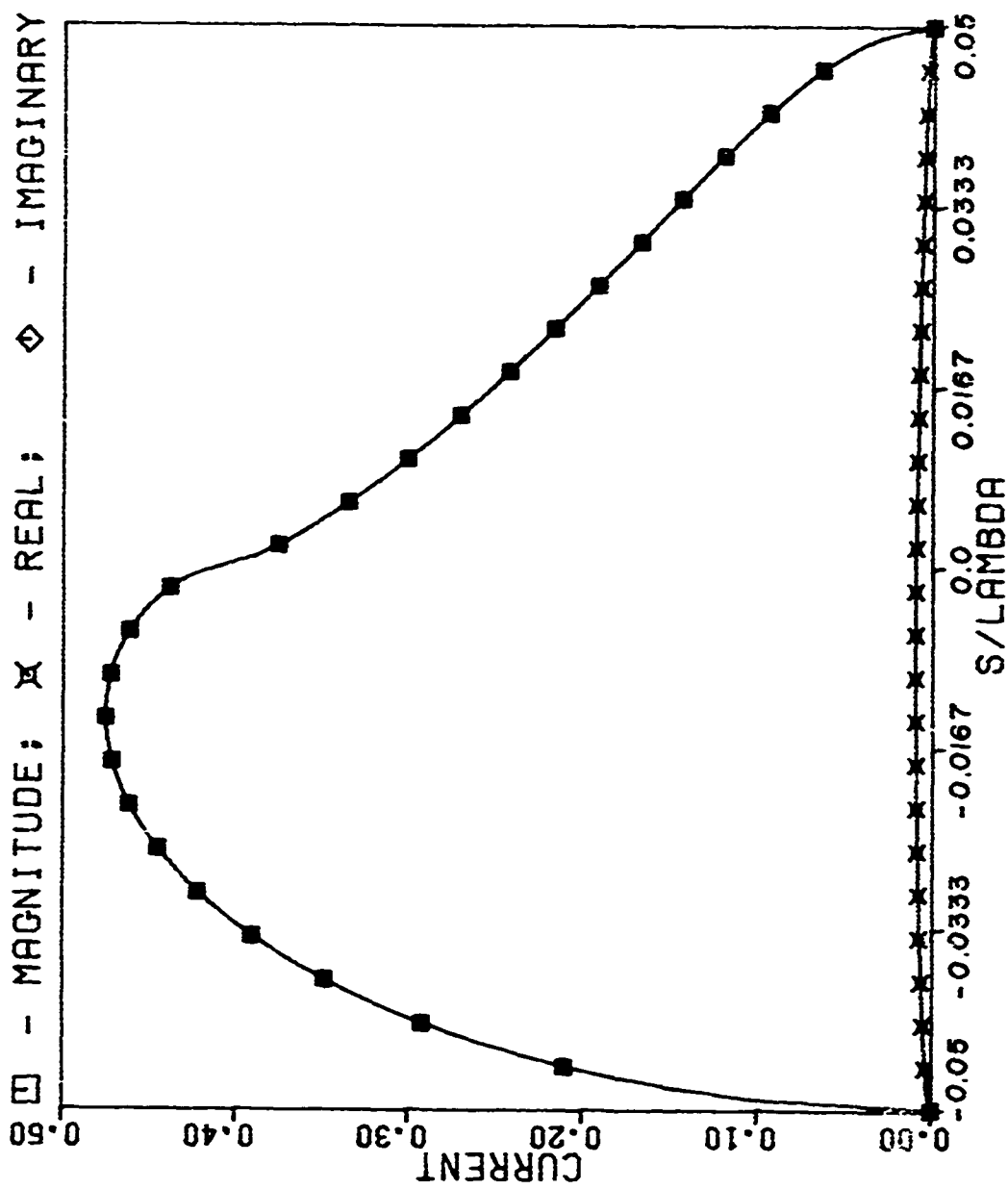


Figure 3.5. Induced current on a 0.1λ strip bent 90° at $s/\lambda = 0$ and illuminated by a TE plane wave normally incident to the section of the strip $s/\lambda < 0$.

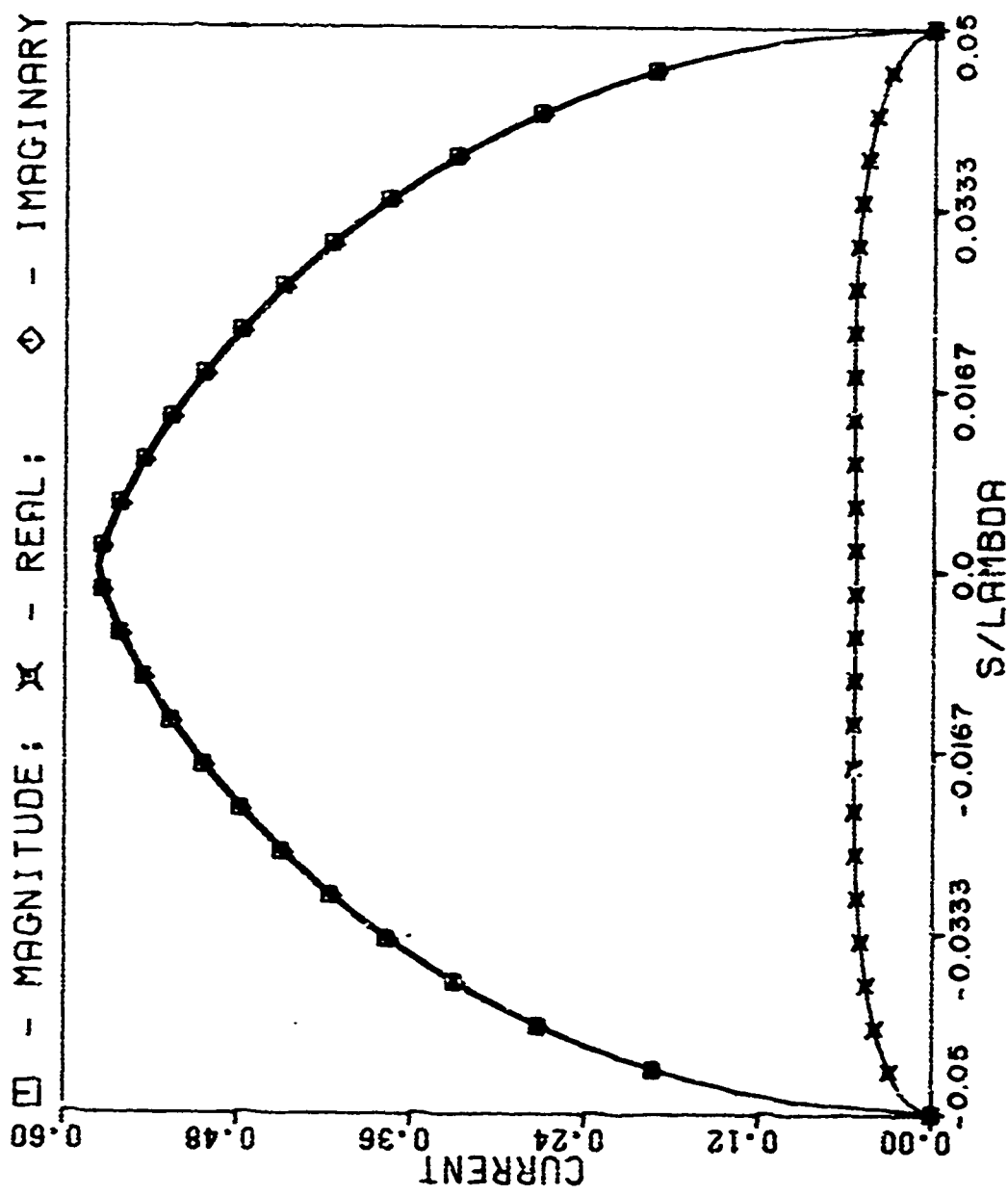


Figure 3.6. Induced current on a 0.1λ strip bent 90° at $s/\lambda = 0$ and illuminated symmetrically by a TE plane wave ($\phi = 135^\circ$).

easily show in this case that the current near the bend must then vary as

$$J(s) \xrightarrow[s \rightarrow 0]{} A + C|s|^{4/3} . \quad (3.23)$$

If the constant term is removed from the numerical data by subtracting the computed current at the bend and C in (3.23) is determined by requiring the computed result to match the second term of (3.23) at a point near the bend, a comparison of the computed variation with the theoretical variation of the current is obtained, as shown in Figure 3.7. Although we are not assured that the computed current magnitudes are correct, the excellent agreement of the computed and theoretical current behavior near the bend does show that the computed results have the right variation in the critical region near the bend.

Effect of Differing Subdomain Sizes on Numerical Solutions

In many numerical procedures, it has been observed that anomalies in the current distribution result when abrupt changes in subdomain sizes are made. In strip problems, enough subdomains can generally be used so that if unequal subdomain sizes are necessary on opposite sides of the bend, the differences in subdomain sizes can be made rather small. In the plate problem to be considered, however, where the number of subdomains in each dimension is severely limited, it may turn out that in order to adequately sample currents on opposite sides of the bend, drastic differences in sub-

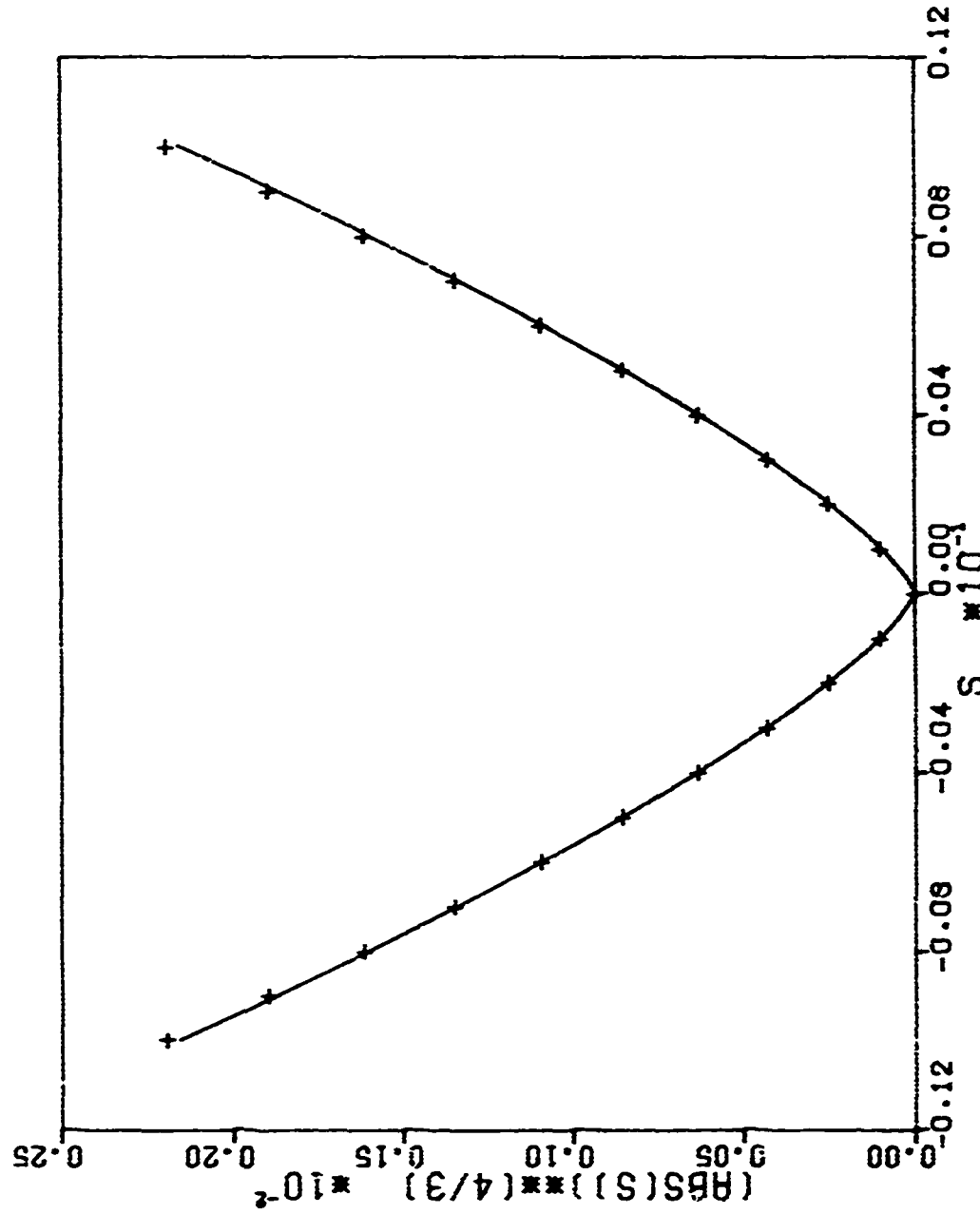


Figure 3.7. Comparison of asymptotic behavior of current (solid line) at the bend for the case shown in Figure 3.6 with the numerically computed current behavior (crosses). The data are matched at the bend ($s = 0$) and at the third numerical value away from the bend.

domain sizes must be used. Figure 3.8 shows the effect on the solution of a change in subdomain size on a flat strip where the change is made in the central portion of the strip. This independence of subdomain size has been verified for a wide range of strip sizes and incidence angles, provided that one always begins with a sufficient number of pulses (and match points) that the variation of the incident field is adequately sampled. Figure 3.9 shows that changing subdomain size at the bend also has no appreciable effect.

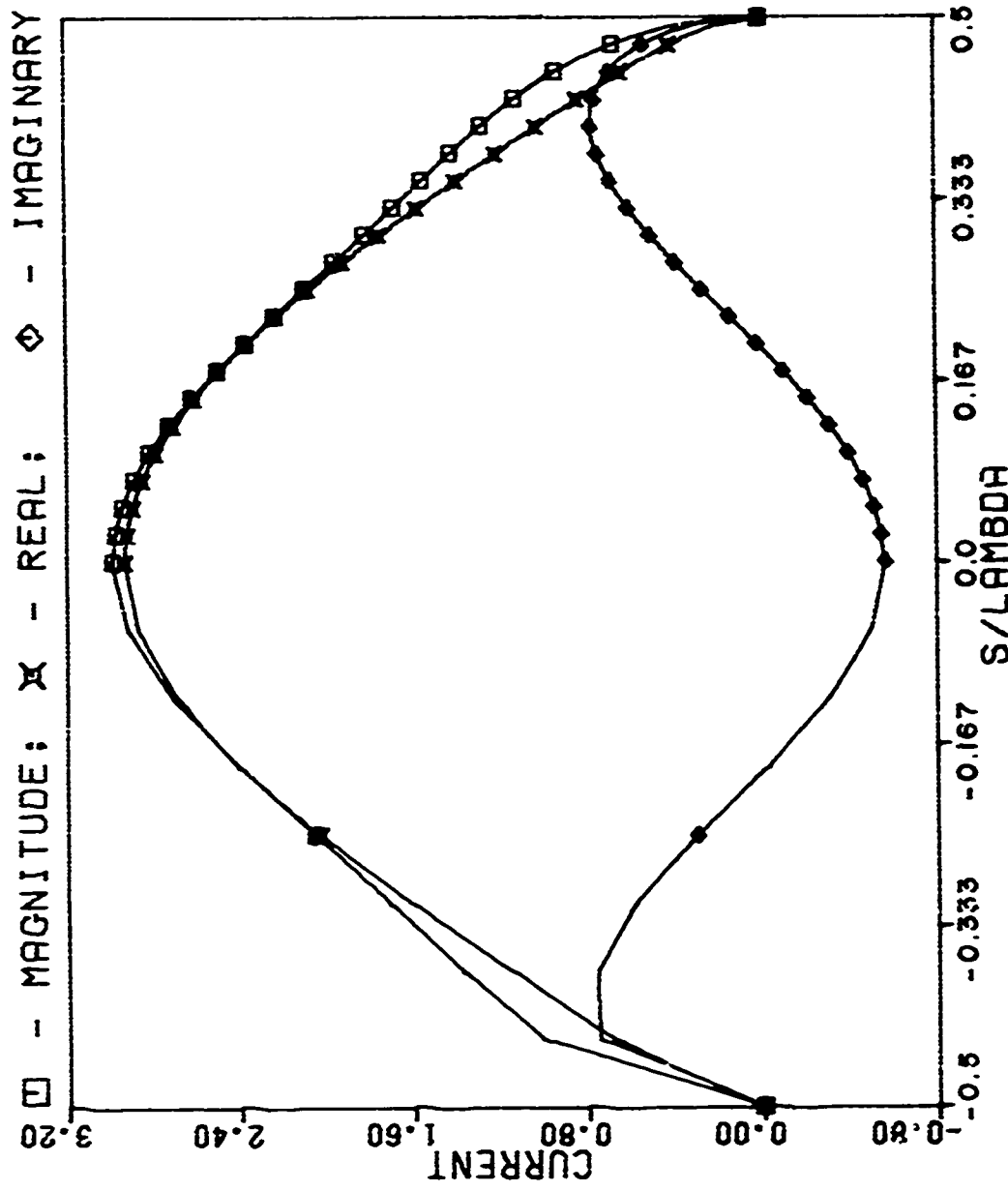


Figure 3.8. Induced current on a 1.0λ strip illuminated by a normally incident TE plane wave. Subdomain size changes at $s/\lambda = 0$ by a ratio of 10 to 1.

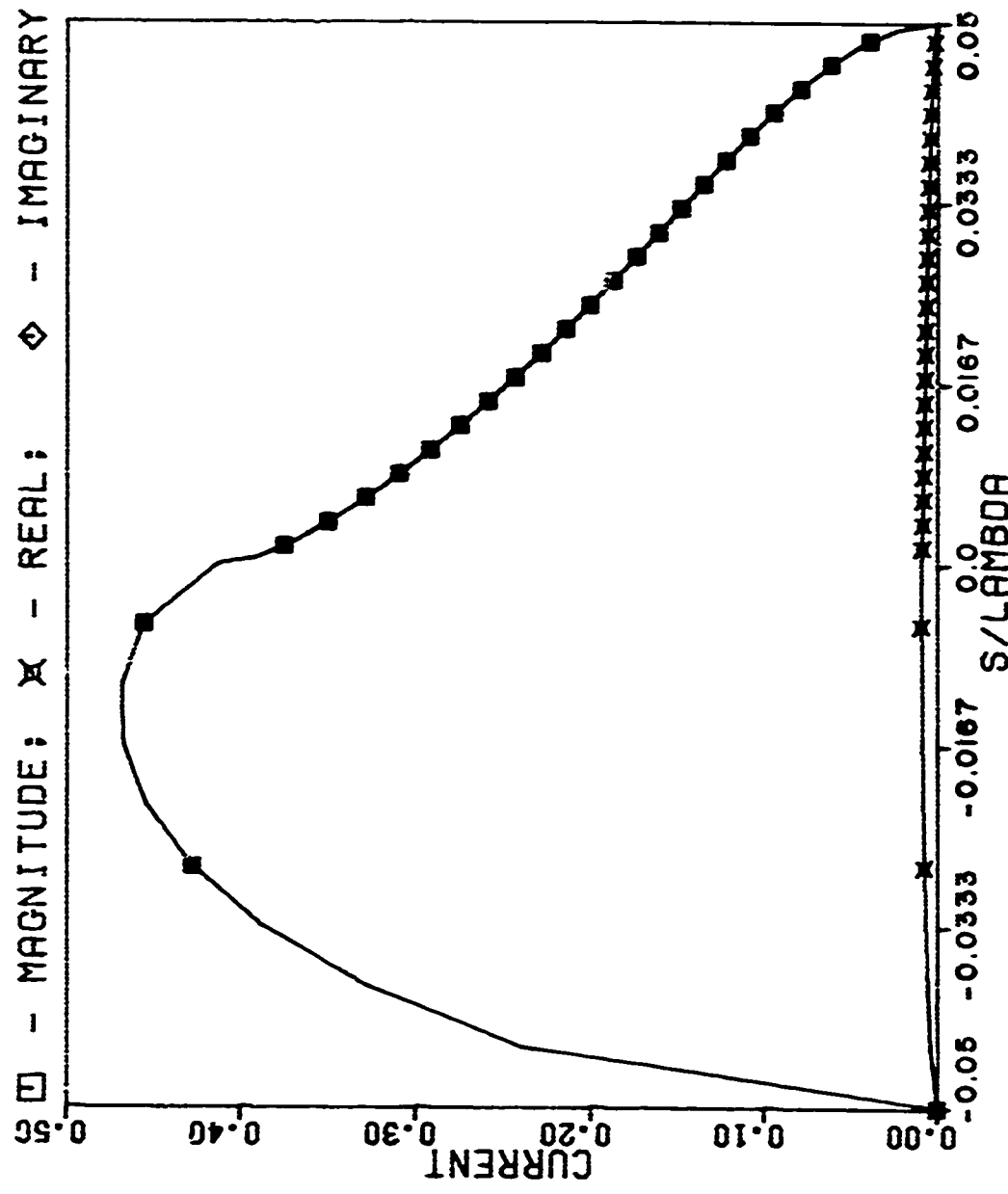


Figure 3.9. Induced current on a 0.1λ strip bent 90° at $s/\lambda = 0$ and illuminated by a TE plane wave normally incident to the section of the strip $s/\lambda < 0$. Subdomain size changes at $s/\lambda = 0$ by a ratio of 10 to 1. (Compare with Figure 3.5.)

IV. FORMULATION OF NUMERICAL SOLUTION FOR SCATTERING BY A BENT PLATE

In this section integral equations are derived for the surface currents induced on a bent rectangular plate subject to plane wave illumination. The solution is complete in the sense that all components of current which can exist on the structure are properly accounted for. A numerical procedure which incorporates the numerical principles developed in Sections II and III is described.

Formulation of the Integral Equations

In developing the equations for the bent plate structure, we refer to the coordinate system of Figure 4.1, where \hat{s} is a unit vector which is perpendicular to the bend and which lies on the plate. The flat rectangular plate is treated merely as a special case where the bend angle is zero.

The currents induced on the scatterer are found via the numerical solution of a set of coupled integro-differential equations. Referring to the coordinate system of Figure 4.1, the coupled equations may be written as

$$-\bar{E}^{inc}(\bar{r}) \cdot \hat{s} = \left[-j\omega \bar{A}(\bar{r}) - \nabla \phi(\bar{r}) \right] \cdot \hat{s} \quad (4.1a)$$

$$-\bar{E}_y^{inc}(\bar{r}) = -j\omega A_y(\bar{r}) - \frac{\partial}{\partial y} \phi(\bar{r}) , \quad (4.1b)$$

\bar{r} on the plate

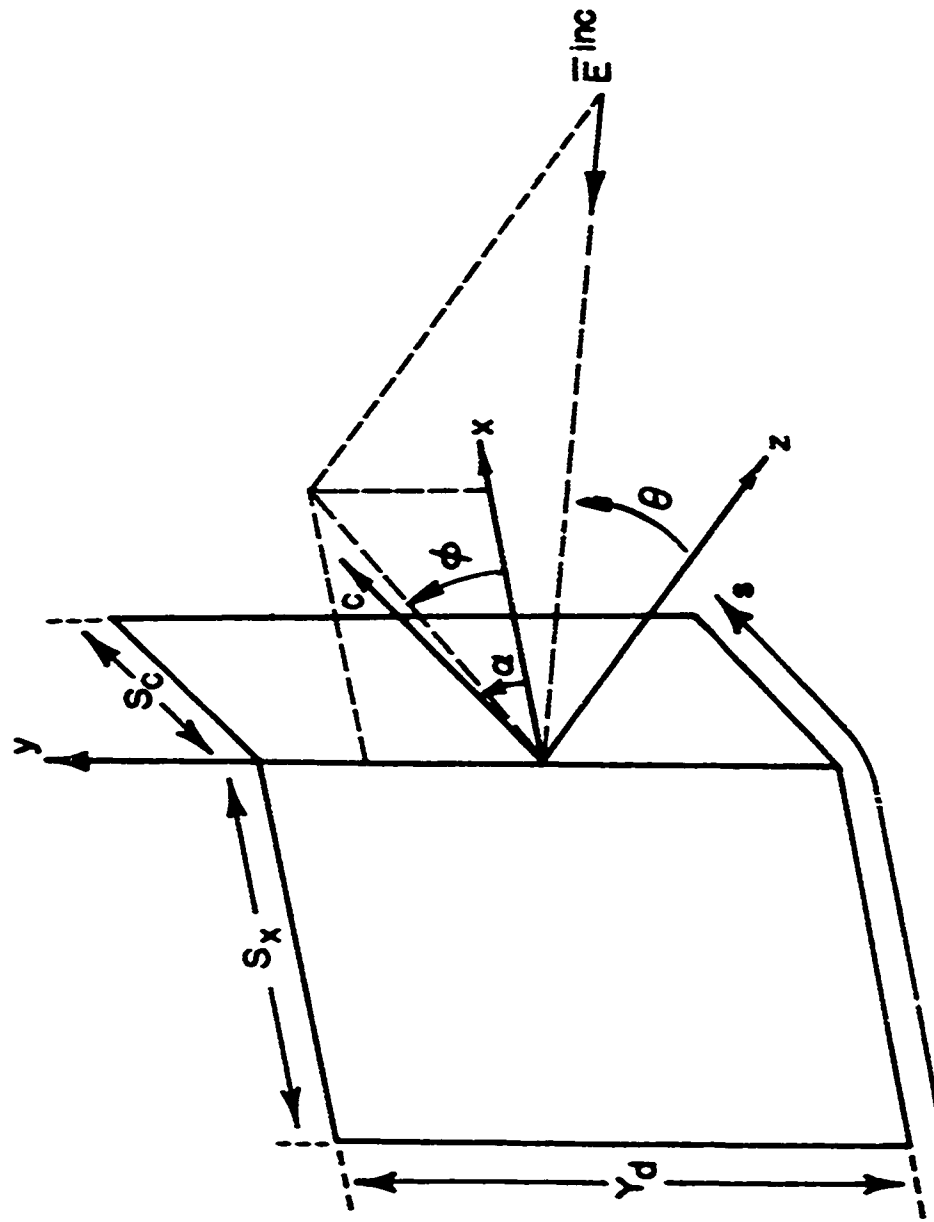


Figure 4.1. Geometry of the bent plate and incident fields.

where

$$\bar{A}(\bar{r}) = \frac{\mu}{4\pi} \iint_{\text{plate}} \bar{J}(\bar{r}') \frac{e^{-jk|\bar{r}-\bar{r}'|}}{|\bar{r}-\bar{r}'|} ds'dy' \quad (4.2)$$

and

$$\phi(\bar{r}) = \frac{1}{4\pi\epsilon} \iint_{\text{plate}} \bar{o}(\bar{r}') \frac{e^{-jk|\bar{r}-\bar{r}'|}}{|\bar{r}-\bar{r}'|} ds'dy' \quad (4.3)$$

The quantities \bar{J} and \bar{o} are the surface current and the surface charge densities on the plate, respectively, and are related through the equation of continuity.

To effect a numerical solution, the plate is divided into a separate set of patches for each current component, J_s and J_y , as shown in Figures 4.2 and 4.3. Note that the current patches for J_s and J_y are staggered relative to each other. The staggering of the subdomains has several advantages. Full subdomains are used to represent currents parallel to an edge, as in the corresponding TM strip problems. Half subdomains are then used to represent the zero currents of components normal to an edge, as in the corresponding TE strip problems. Furthermore, subdomains for current components normal to the bend are wrapped around the bend, ensuring continuity of current flowing around the bend, while components parallel to the bend are represented by separate subdomains on either side of the bend, ensuring the independence of currents on opposite sides of the bend. The staggering of the orthogonal current

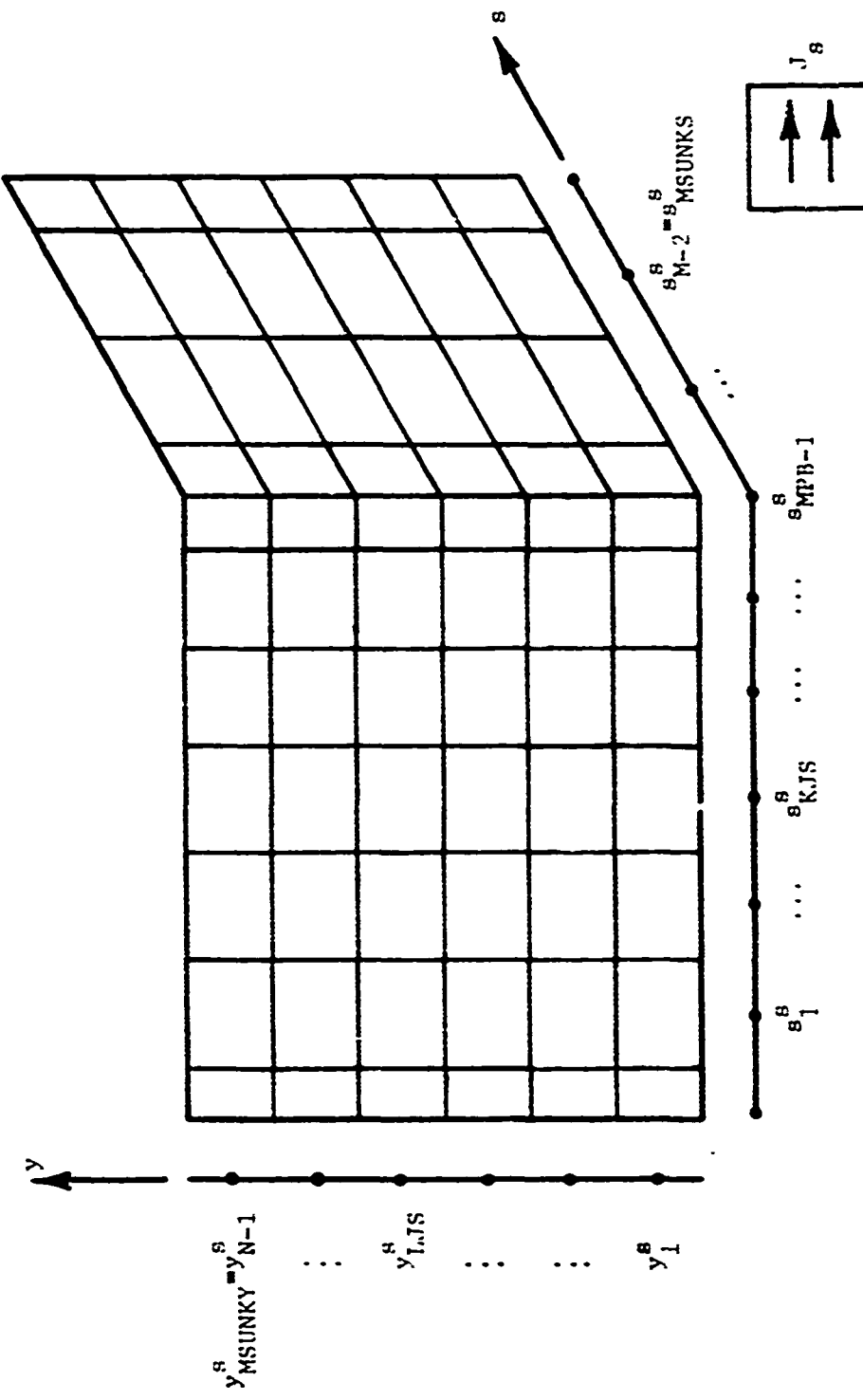


Figure 4.2. Subdomain scheme for a-directed currents.

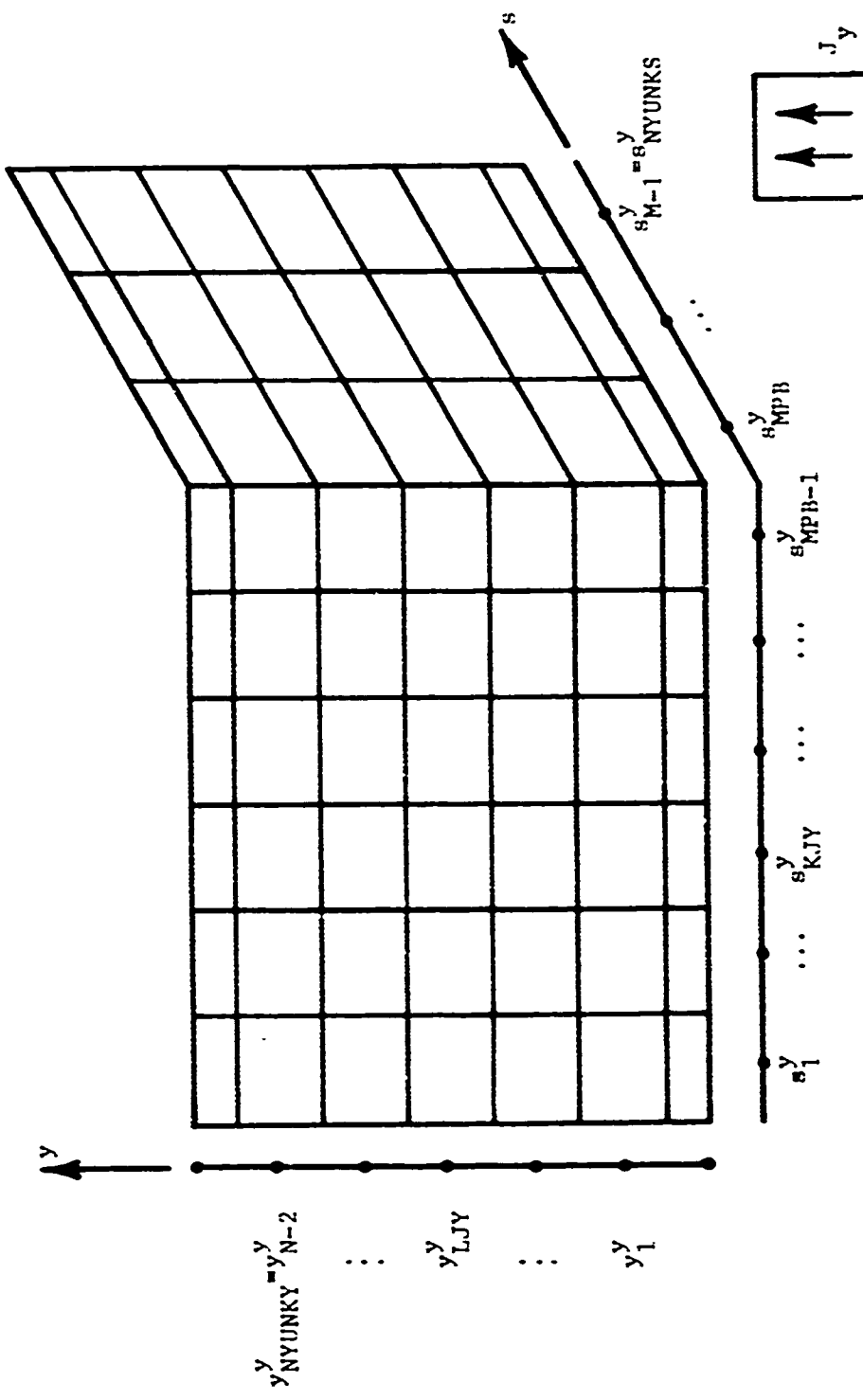


Figure 4.3. Subdomain scheme for y -directed currents.

subdomains is also important because it minimizes the error in the central difference formulas that are used to approximate the derivatives in (4.1) and permits one to use the same numerical algorithm for edge subdomains as for interior subdomains. Furthermore, the method seems readily generalizable to treating surfaces of arbitrary shape. Within each patch, the current is assumed constant so that the expansions for the current components, referring to Figures 4.2 and 4.3, are

$$\bar{J}_s(\bar{r}) \approx \hat{s} \sum_{LJS=1}^{MSUNKY} \sum_{KJS=1}^{MSUNKS} J_{s,LJS}^{KJS} p_{KJS,LJS}^s(\bar{r}) \quad (4.4a)$$

$$J_y(\bar{r}) \approx \sum_{LJY=1}^{NYUNKY} \sum_{KJY=1}^{NYUNKS} J_{y,LJY}^{KJY} p_{KJY,LJY}^y(\bar{r}) \quad (4.4b)$$

where

$$p_{KJS,LJS}^s(\bar{r}) = \begin{cases} 1, & \left\{ \begin{array}{l} \frac{s_{KJS} + s_{KJS-1}}{2} \leq s \leq \frac{s_{KJS} + s_{KJS+1}}{2} \\ y_{LJS}^s - \frac{\Delta y}{2} \leq y \leq y_{LJS}^s + \frac{\Delta y}{2} \end{array} \right. \\ 0, & \text{otherwise} \end{cases} \quad (4.5a)$$

$$p_{KJY, LJY}^y(\bar{r}) = \begin{cases} 1, & \begin{cases} s_{KJY}^y - \frac{\Delta s_x}{2} \leq s \leq s_{KJY}^y + \frac{\Delta s_x}{2}, & KJY \leq MPB-1 \\ s_{KJY}^y - \frac{\Delta s_c}{2} \leq s \leq s_{KJY}^y + \frac{\Delta s_c}{2}, & MPB \leq KJY \end{cases} \\ & y_{LJY}^y - \frac{\Delta y}{2} \leq y \leq y_{LJY}^y + \frac{\Delta y}{2} \\ 0, & \text{otherwise} \end{cases} \quad (4.5b)$$

and where $\bar{r} = \hat{ss} + \hat{yy}$.

Coordinate quantities are (see Figures 4.2 and 4.3)

$$s_{KJS}^s = \begin{cases} -s_x + (KJS)\Delta s_x, & 1 \leq KJS \leq MPB-1 \\ (KJS - MPB+1)\Delta s_c, & MPB \leq KJS \leq MSUNKS \end{cases} \quad (4.6a)$$

$$y_{LJS}^s = -\frac{Y_d}{2} + (LJS - \frac{1}{2})\Delta y, \quad 1 \leq LJS \leq MSUNKY \quad (4.6b)$$

$$s_{KJY}^y = \begin{cases} -s_x + (KJY - \frac{1}{2})\Delta s_x, & 1 \leq KJY \leq MPB-1 \\ (KJY - MPB + \frac{1}{2})\Delta s_c, & MPB \leq KJY \leq NYUNKS \end{cases} \quad (4.6c)$$

$$y_{LJY}^y = -\frac{Y_d}{2} + (LJY)\Delta y, \quad 1 \leq LJY \leq NYUNKY \quad (4.6d)$$

where

$$\Delta y = \frac{Y_d}{N-1} \quad (4.7a)$$

$$\Delta s_x = \frac{s_x}{MPB-1} \quad (4.7b)$$

$$\Delta s_c = \frac{s_c}{MFB-1} \quad (4.7c)$$

$$M = MFB + MPB - 1 .$$

The quantities s_x , s_c , and y_d are dimensions of the plate along the x , c , and y axes, respectively, and M and N are defined in Figures 4.2 and 4.3. The unknown pulse current coefficients $J_s^{KJS,LJS}$ and $J_y^{KJY,LJY}$ in (4.4) may be taken to represent the current at the center of their corresponding subdomains or directly on the bend and centered in the y -direction for sub-domains which straddle the bend. The substitution of (4.4) into (4.2) permits the computation of the vector potential. To compute the scalar potential, the surface charge density is needed. It is conveniently computed, as in the TE strip case, by a finite difference approximation to the equation of continuity. The result is

$$\rho(\bar{r}) = \frac{i}{\omega} \sum_{LJ=1}^{N-1} \sum_{KJ=1}^{M-1} \left\{ \left[\frac{J_{KJ,LJ}^s - J_{KJ-1,LJ}^s}{s_{KJ}^s - s_{KJ-1}^s} \right] + \left[\frac{J_{KJ,KJ}^y - J_{KJ,LJ-1}^y}{y_{LJ}^y - y_{LJ-1}^y} \right] \right\} p_{KJ,LJ}(\bar{r}) \quad (4.8)$$

where the components of current normal to the edge satisfy

$$J_s^{0,LJ} \equiv J_s^{M-1,LJ} \equiv J_y^{KJ,0} \equiv J_y^{KJ,N-1} \equiv 0 \quad . \quad (4.9)$$

The pulse basis functions for the charge are defined as
(Figure 4.4)

$$p_{KJ,LJ}(\bar{r}) = \begin{cases} 1, & \begin{cases} s_{KJ}^y - \frac{\Delta s_x}{2} \leq s \leq s_{KJ}^y + \frac{\Delta s_x}{2}, & KJ \leq MPB-1 \\ s_{KJ}^y - \frac{\Delta s_c}{2} \leq s \leq s_{KJ}^y + \frac{\Delta s_c}{2}, & MPB \leq KJ \\ y_{LJ}^s - \frac{\Delta y}{2} \leq s \leq y_{LJ}^s + \frac{\Delta y}{2} \end{cases} \\ 0, & \text{otherwise} . \end{cases} \quad (4.10)$$

Substitution of (4.8) into (4.3) permits the scalar potential to be computed in terms of the currents. Equations (4.1a) and (4.1b) are enforced at the match points

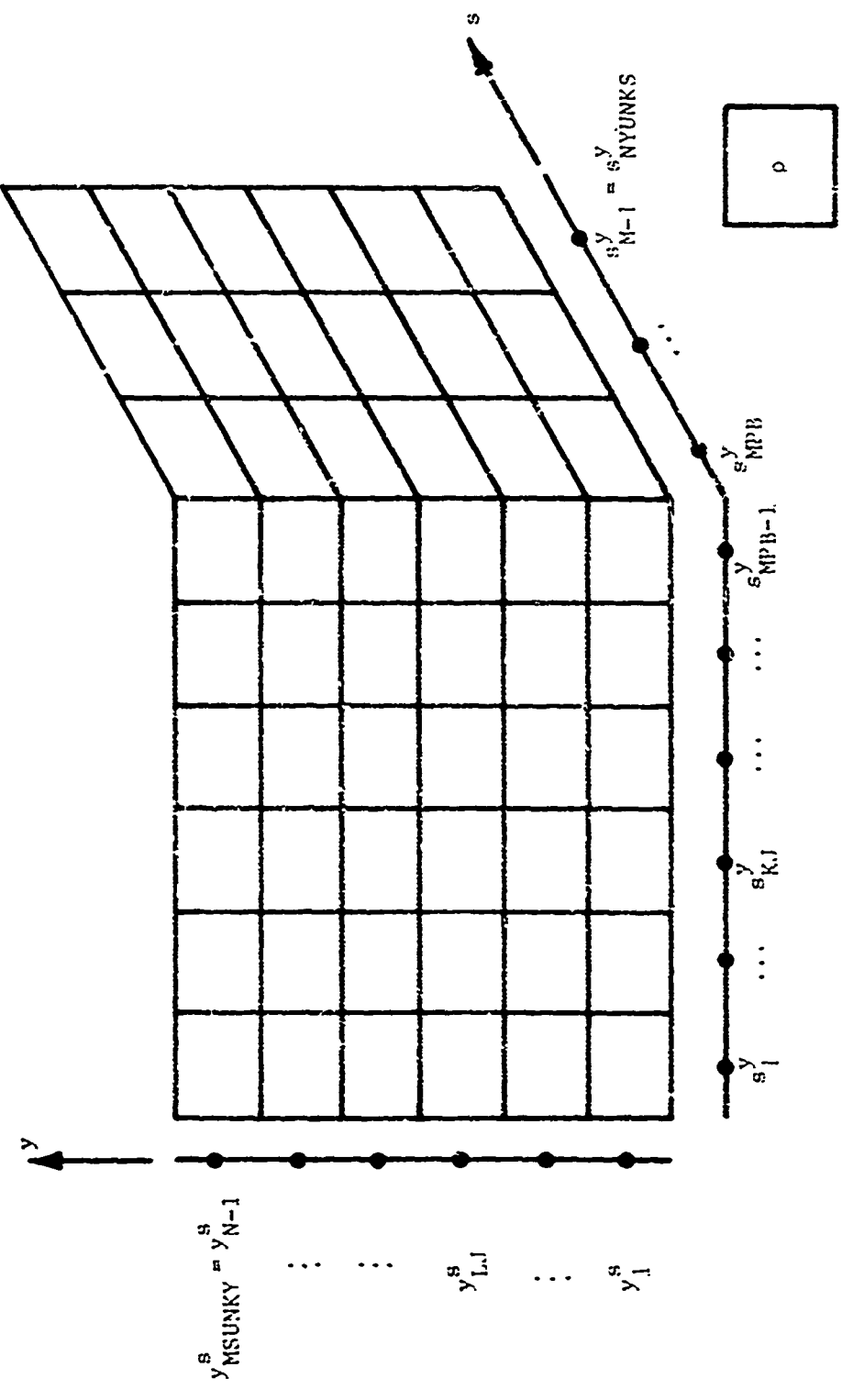


Figure 4.4. Subdomain scheme for charge patches.

$$\bar{r}_{IJ,JS}^S = s_{IS}^S \hat{s} + y_{JS}^S \hat{y}, \quad 1 \leq IS \leq MSUNKS, \\ 1 \leq JS \leq MSUNKY, \quad (4.11a)$$

and

$$\bar{r}_{IY,JY}^Y = s_{IY}^Y \hat{s} + s_{JY}^Y \hat{y}, \quad 1 \leq IY \leq NYUNKS, \\ 1 \leq JY \leq NYUNKY, \quad (4.11b)$$

respectively. Except at the bend, we may merely replace the partial derivatives of scalar potential by central finite difference operators. Showing the s-y coordinates of each term explicitly, we have

$$-\bar{\epsilon}_x^{inc}(s_{IS}^S, y_{JS}^S) \Delta s_x = -j\omega A_x(s_{IS}^S, y_{JS}^S) \Delta s_x \\ - [\phi(s_{IS+1}^S, y_{JS}^S) - \phi(s_{IS}^S, y_{JS}^S)], \quad (4.12a)$$

IS=1 to MPB-2
JS=1 to MSUNKY,

valid on the surface in the x-y plane,

$$-\bar{\epsilon}_c^{inc}(s_{IS}^S, y_{JS}^S) \Delta s_c = -j\omega A_c(s_{IS}^S, y_{JS}^S) \Delta s_c \\ - [\phi(s_{IS+1}^S, y_{JS}^S) - \phi(s_{IS}^S, y_{JS}^S)], \quad (4.12b)$$

IS=MPB to MSUNKS
JS=1 to MSUNKY,

valid on the surface in the c-y plane, and

$$-\mathbf{E}_y^{\text{inc}}(s_{IY}^y, y_{JY}^y) \Delta y = -j\omega A_y(s_{IY}^y, y_{JY}^y) \Delta y$$

$$- \left[\phi(s_{IY}^y, y_{JY+1}^s) - \phi(s_{IY}^y, y_{JY}^s) \right] , \quad (4.12c)$$

IY=1, NYUNKS

JY=1, NYUNKY,

valid everywhere on the plate. At the bend, we require the tangential components of electric field along both the x- and c-directions to vanish. For these field components, we write the directional derivative of the scalar potential along the x-direction as a backward difference and that along the c-direction as a forward difference operator:

$$-\mathbf{E}_x^{\text{inc}}(s_{IS}^s, y_{JS}^s) = -j\omega A_x(s_{IS}^s, y_{JS}^s) - \frac{\phi(s_{IS}^s, y_{JS}^s) - \phi(s_{IS}^y, y_{JS}^s)}{\Delta s_x / 2}$$

and

$$-\mathbf{E}_c^{\text{inc}}(s_{IS}^s, y_{JS}^s) = -j\omega A_c(s_{IS}^s, y_{JS}^s) - \frac{\phi(s_{IS+1}^y, y_{JS}^s) - \phi(s_{IS}^s, y_{JS}^s)}{\Delta s_c / 2} ,$$

IS=MPB-1, 1 ≤ JS ≤ MSUNKY .

Note the appearance of the scalar potential term $\phi(s_{IS}^s, y_{JS}^s)$ which is evaluated at the bend where the charge is normally singular. As discussed in Section II, this would normally be expected to introduce numerical anomalies when pulse functions are used. However, we need only one equation at the bend and we obtain it by multiplying the two equations above by $\Delta s_x / 2$

and $\Delta s_c / 2$, respectively, and adding the resulting equations together. The term involving the potential at the edge then disappears altogether:

$$\begin{aligned}
 & - \frac{1}{2} \left[E_x^{\text{inc}}(s_{IS}^s, y_{JS}^s) \Delta s_x + E_c^{\text{inc}}(s_{IS}^s, y_{JS}^s) \Delta s_c \right] \\
 & = - j \frac{\omega}{2} \left[A_x(s_{IS}^s, y_{JS}^s) \Delta s_x + A_c(s_{IS}^s, y_{JS}^s) \Delta s_c \right] \\
 & - \left[\phi(s_{IS+i}^y, y_{JS}^s) - \phi(s_{IS}^y, y_{JS}^s) \right], \quad (4.12d)
 \end{aligned}$$

IS=MPB-1

JS=1, MSUNKY .

Obviously, if $\Delta s_x = \Delta s_c$, (4.12b) and (4.12d) reduce to (4.12a) when the bend angle is set to $\alpha = 0$, reducing the structure to a flat plate. In order to define the quantities appearing in equations (4.12) more easily, it is convenient to define two new vectors

$$\bar{r}_x = \hat{x}\hat{x} \div \hat{y}\hat{y} \quad (4.13a)$$

$$\bar{r}_c = \hat{c}\hat{c} + \hat{y}\hat{y}, \quad (4.13b)$$

so that \bar{r}_x defines a point on the portion of the plate in the x-y plane, and \bar{r}_c defines a point on the portion of the plate in the c-v plane. Then the terms appearing in equations (4.12) are defined in (4.14) and (4.15) which follow.

$$\Lambda_y(\tilde{r}_p) = \frac{\mu}{4\pi} \sum_{L,JY=1}^M \left\{ \sum_{KJY=1}^{M_{PB}-1} J_y^{JY, LJY} \psi_{px} \left(\tilde{r}_p; s_{KJY}^y - \frac{\Delta s_x}{2}, s_{KJY}^y + \frac{\Delta s_x}{2}, y_{LJY}^y - \frac{\Delta y}{2}, y_{LJY}^y + \frac{\Delta y}{2} \right) \right.$$

$$+ \sum_{KJY=M_{PB}}^{M_{PB}} J_y^{KJY, LJY} \psi_{pc} \left(\tilde{r}_p; s_{KJY}^y - \frac{\Delta s_c}{2}, s_{KJY}^y + \frac{\Delta s_c}{2}, y_{LJY}^y - \frac{\Delta y}{2}, y_{LJY}^y + \frac{\Delta y}{2} \right) \left. \right\} \quad (4.14a)$$

p = x or c ,

$$\Lambda_p(\tilde{r}_p) = \frac{\mu}{4\pi} \sum_{L,JJS=1}^{M_{PB}-2} \left\{ \sum_{KJS=1}^{M_{PB}-2} J_s^{KJS, LJS} \psi_{px} \left(\tilde{r}_p; s_{KJS}^s - \frac{\Delta s_x}{2}, s_{KJS}^s + \frac{\Delta s_x}{2}, y_{LJS}^s - \frac{\Delta y}{2}, y_{LJS}^s + \frac{\Delta y}{2} \right) \right. \\ \times \left. \left(\delta_{px} + \delta_{pc} \cos \alpha \right) \right\}$$

$$+ J_s^{M_{PB}-1, LJS} \left[\psi_{px} \left(\tilde{r}_p; s_{M_{PB}-1}^s - \frac{\Delta s_x}{2}, s_{M_{PB}-1}^s + \frac{\Delta s_x}{2}, y_{LJS}^s - \frac{\Delta y}{2}, y_{LJS}^s + \frac{\Delta y}{2} \right) \left(\delta_{px} + \delta_{pc} \cos \alpha \right) \right]$$

$$+ \psi_{pc} \left(\tilde{r}_p; s_{M_{PB}-1}^s, s_{M_{PB}-1}^s + \frac{\Delta s_c}{2}, y_{LJS}^s - \frac{\Delta y}{2}, y_{LJS}^s + \frac{\Delta y}{2} \right) \left(\delta_{pc} + \delta_{px} \cos \alpha \right)]$$

$$MSUNKS \sum_{KJS=M_{PB}}^{M_{PB}} J_s^{KJS, LJS} \psi_{pc} \left(\tilde{r}_p; s_{KJS}^s - \frac{\Delta s_c}{2}, s_{KJS}^s + \frac{\Delta s_c}{2}, y_{LJS}^s - \frac{\Delta y}{2}, y_{LJS}^s + \frac{\Delta y}{2} \right) \left(\delta_{pc} + \delta_{px} \cos \alpha \right) \} \quad (4.14b)$$

p = x or c

$$\Phi(\tilde{r}_p) = \frac{1}{4\pi r_0} \sum_{l,j=1}^{N-1} \left\{ \sum_{K,l=1}^{M_p B-1} \psi_{px} \left(\tilde{r}_p; s_{K,l}^y - \frac{\Delta s_x}{2}, s_{K,l}^y + \frac{\Delta s_x}{2}, s_{l,j}^y - \frac{\Delta y}{2}, s_{l,j}^y + \frac{\Delta y}{2} \right) \right.$$

$$\times \left[\frac{j^{KJ,LJ}}{\lambda s_x} - \frac{j^{KJ-1,LJ}}{\lambda s_x} + \frac{j^{KJ,LJ-1}}{\lambda y} - \frac{j^{KJ-1,LJ-1}}{\lambda y} \right]$$

$$+ \sum_{K,j=M_p B}^{N-1} \psi_{pc} \left(\tilde{r}_p; s_{K,j}^y - \frac{\Delta s_c}{2}, s_{K,j}^y + \frac{\Delta s_c}{2}, s_{l,j}^y - \frac{\Delta y}{2}, s_{l,j}^y + \frac{\Delta y}{2} \right)$$

$$\times \left[\frac{j^{KJ,LJ}}{\lambda s_c} - \frac{j^{KJ-1,LJ}}{\lambda s_c} + \frac{j^{KJ,LJ-1}}{\lambda y} - \frac{j^{KJ-1,LJ-1}}{\lambda y} \right] \} \quad (4.15)$$

In (4.14), δ_{st} is a rather unconventional but convenient use of the Kronecker delta,

$$\delta_{st} = \begin{cases} 1, & \text{if } s = t \\ 0, & \text{if } s \neq t \end{cases}, \quad (4.16)$$

and the ψ functions are defined as

$$\psi_{pq}(\bar{r}_p; s_1, s_2, y_1, y_2) = \int_{s_1}^{s_2} \int_{y_1}^{y_2} \frac{e^{-jkR_{pq}(\bar{r}_p, \bar{r}'_q)}}{R_{pq}(\bar{r}_p, \bar{r}'_q)} ds' dy', \quad (4.17)$$

$p = x$ or c ,

$q = x$ pr c ,

$$R_{xx} = |\bar{r}_x - \bar{r}'_x| = \left[(x-x')^2 + (y-y')^2 \right]^{\frac{1}{2}} \quad (4.18a)$$

$$R_{cc} = |\bar{r}_c - \bar{r}'_c| = \left[(c-c')^2 + (y-y')^2 \right]^{\frac{1}{2}} \quad (4.18b)$$

$$R_{xc} = |\bar{r}_x - \bar{r}'_c| = \left[(x-c'\cos\alpha)^2 + (y-y')^2 + (c'\sin\alpha)^2 \right]^{\frac{1}{2}} \quad (4.18c)$$

$$R_{cx} = |\bar{r}_c - \bar{r}'_x| = \left[(c\cos\alpha - x')^2 + (y-y')^2 + (c\sin\alpha)^2 \right]^{\frac{1}{2}} \quad (4.18d)$$

All the quantities appearing on the right-hand sides of equations (4.12) are now defined. The incident field is expressed as

$$\hat{E}^{inc} = (E_{\theta}\hat{s} + E_{\phi}\hat{\phi}) e^{jkn \cdot \bar{r}} \quad (4.19)$$

where \hat{s} and $\hat{\phi}$ are the standard spherical coordinates with respect to the x, y, z coordinate system. The components of

the incident field in the x-y plane can be found by a simple coordinate transformation to be

$$\begin{aligned}
 E_x^{\text{inc}}(x, y)\hat{x} + E_y^{\text{inc}}(x, y)\hat{y} &= \left[(E_{\theta} \cos\theta \cos\phi - E_{\phi} \sin\phi) \hat{x} \right. \\
 &\quad \left. + (E_{\theta} \cos\theta \sin\phi + E_{\phi} \cos\phi) \hat{y} \right] \\
 &\quad \times e^{jk(x \sin\theta \cos\phi - y \sin\theta \sin\phi)} \\
 &= \left[E_x^{\text{inc}}(0, 0)\hat{x} + E_y^{\text{inc}}(0, 0)\hat{y} \right] \\
 &\quad \times e^{jk(x \sin\theta \cos\phi + y \sin\theta \sin\phi)}
 \end{aligned} \tag{4.20a}$$

while the corresponding fields in the c-y plane are

$$\begin{aligned}
 E_c^{\text{inc}}(c, y)\hat{c} + E_y^{\text{inc}}(c, y)\hat{y} &= \left[(E_{\theta} \cos\theta \cos\phi \cos\alpha + E_{\phi} \sin\phi \sin\alpha - E_{\phi} \sin\theta \cos\alpha) \hat{c} \right. \\
 &\quad \left. + (E_{\phi} \cos\theta \sin\phi + E_{\phi} \cos\phi) \hat{y} \right] \\
 &\quad \times e^{jk(c \sin\theta \cos\phi \cos\alpha - c \cos\theta \sin\alpha + y \sin\theta \sin\phi)} \\
 &= \left[E_c^{\text{inc}}(0, 0)\hat{c} + E_y^{\text{inc}}(0, 0)\hat{y} \right] \\
 &\quad \times e^{jk(c \sin\theta \cos\phi \cos\alpha - c \cos\theta \sin\alpha + y \sin\theta \sin\phi)}
 \end{aligned} \tag{4.20b}$$

Equations (4.12) constitute a system of linear equations for the unknown current coefficients in (4.4).

The system can be written as a matrix equation

$$ZI = V \quad (4.21)$$

where Z is the impedance matrix, I is a column vector of the unknown current coefficients, and V is a column vector containing the dependence on the incident field. The impedance matrix elements consist of appropriate linear combinations of integrals of the form (4.17). The evaluation of (4.17) is by two-dimensional Gaussian quadrature. In the case where \bar{r}_p is interior to the patch over which the integration is to be performed, the integrand has an integrable singularity. For a discussion of the numerical evaluation of (4.17) in this case, refer to Appendix C.

The staggered subdomain scheme has the advantage of avoiding the evaluation of any field components or potential quantities at edges or corners which would be adversely affected by the absence of the correct singularity in the current or charge expansion. The actual behavior of current at an edge is discussed in Appendix A while the behavior of current near a corner is discussed in Appendix D. In Appendix E a possible correction factor for edge currents is suggested. More extensive convergence studies, however, are necessary to validate the legitimacy of the formulas given there.

An alternative form of Equations (4.12) is given in Appendix F. This form describes the scattered field entirely in terms of vector potential quantities and has advantages

for a flat plate. For a bent plate, however, Equations (4.12) are both succinct and convenient to apply.

V. NUMERICAL RESULTS FOR PLATE STRUCTURES

In this section we present numerical results for flat and bent structures illuminated by plane waves. The numerical formulation and approach of Section IV was used in the computation of all results shown in this section. Other numerical approaches were tried during this study but, for brevity, none of those results are given here even though they are quite helpful in illustrating the advantages of the adopted approach.

In plate problems, of course, one is severely constrained by the number of subdomains that can be used because of computer central core limitations. Thus, even though the problem may be numerically formulated correctly in the sense that it will converge to the correct answer as the number of subdomains tends to infinity, in a practical sense, it is a high rate of convergence that is important so that one may obtain "converged" answers with as few subdomains as possible. Figure 5.1 shows the convergence of the dominant component of the current at the center of a square plate at two frequencies and for two angles of incidence. The good convergence is attributed primarily to the more accurate modeling of the electrical size of the plate that is afforded by the staggered subdomain scheme. At the lower

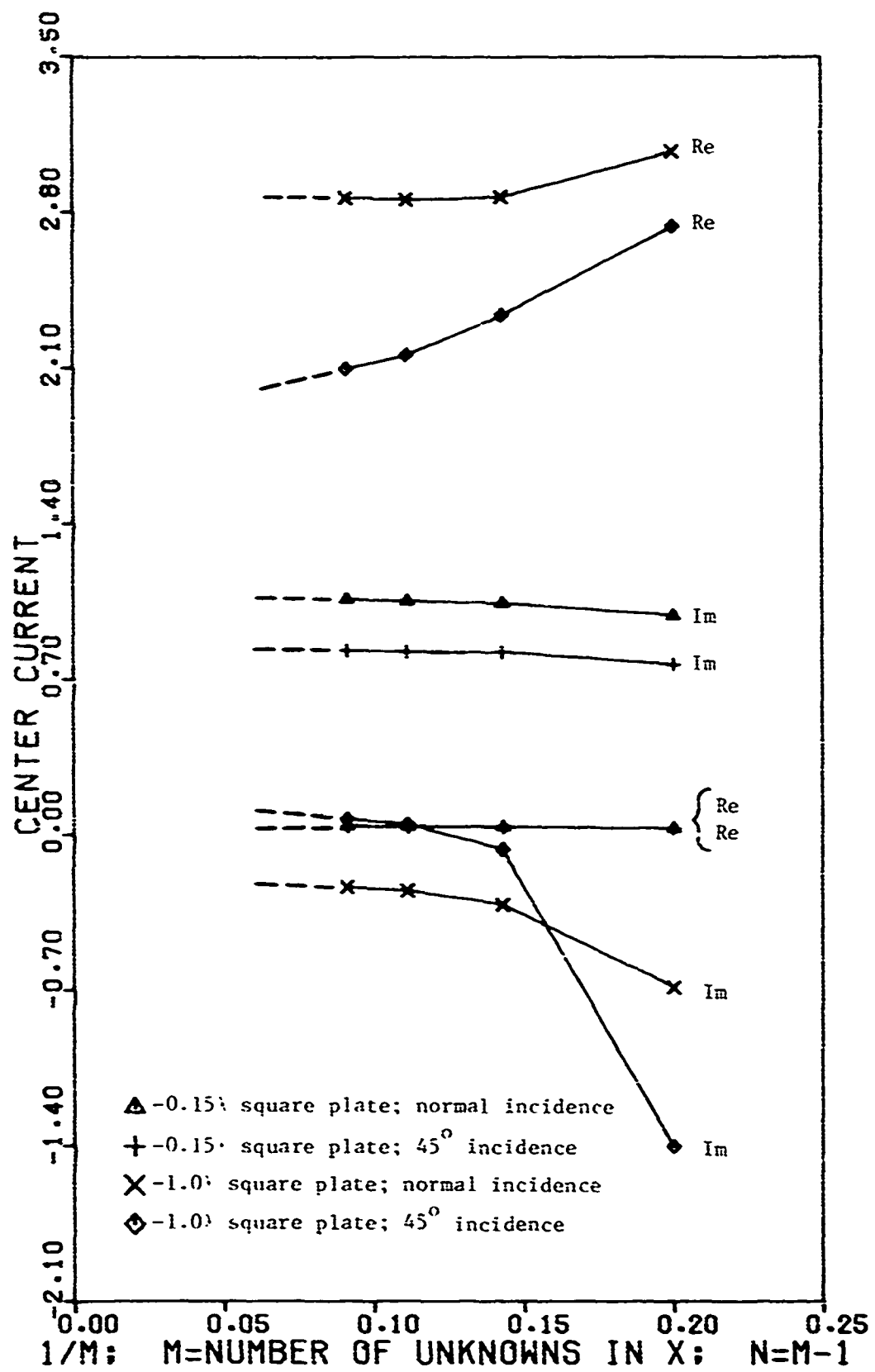


Figure 5.1. Convergence curves for 0.15λ and 1.0λ square plates for normal and oblique angles of incidence.

frequency, convergence is achieved very quickly; at the higher frequency, the figure indicates that about seven subdomains per wavelength are needed for normal incidence. As the angle of incidence increases, more pulses are needed not only to represent the more complex current distribution, but also to adequately sample the incident field.

Figures 5.2 - 5.25 show computed current distributions for flat and bent plates for two frequencies and for various angles of incidence. In all the figures, if the plate is thought of as folded out flat (the resulting rectangular plate outline is shown in the figures), the value of the current at each point is the vertical distance from the plane of the flattened plate to the surface that is plotted in the figure. The perspective view has been chosen to obtain the best overall view of each current distribution. While use of a digital plotter is mandatory in graphically displaying such a large volume of data, this mechanization is not without some peculiarities which require our explanation. First, the bend is denoted merely by the notation "s = 0" which locates the point at which the bend (if present) of the unfolded plate intersects the edge of the plate. This intersected edge (in the left foreground of the flattened plate in all the figures) is parallel to the s-axis (Figure 4.1); the edge in the right foreground in all the figures is parallel to the y-axis. The incident magnetic field intensity in all cases is unity and each figure shows

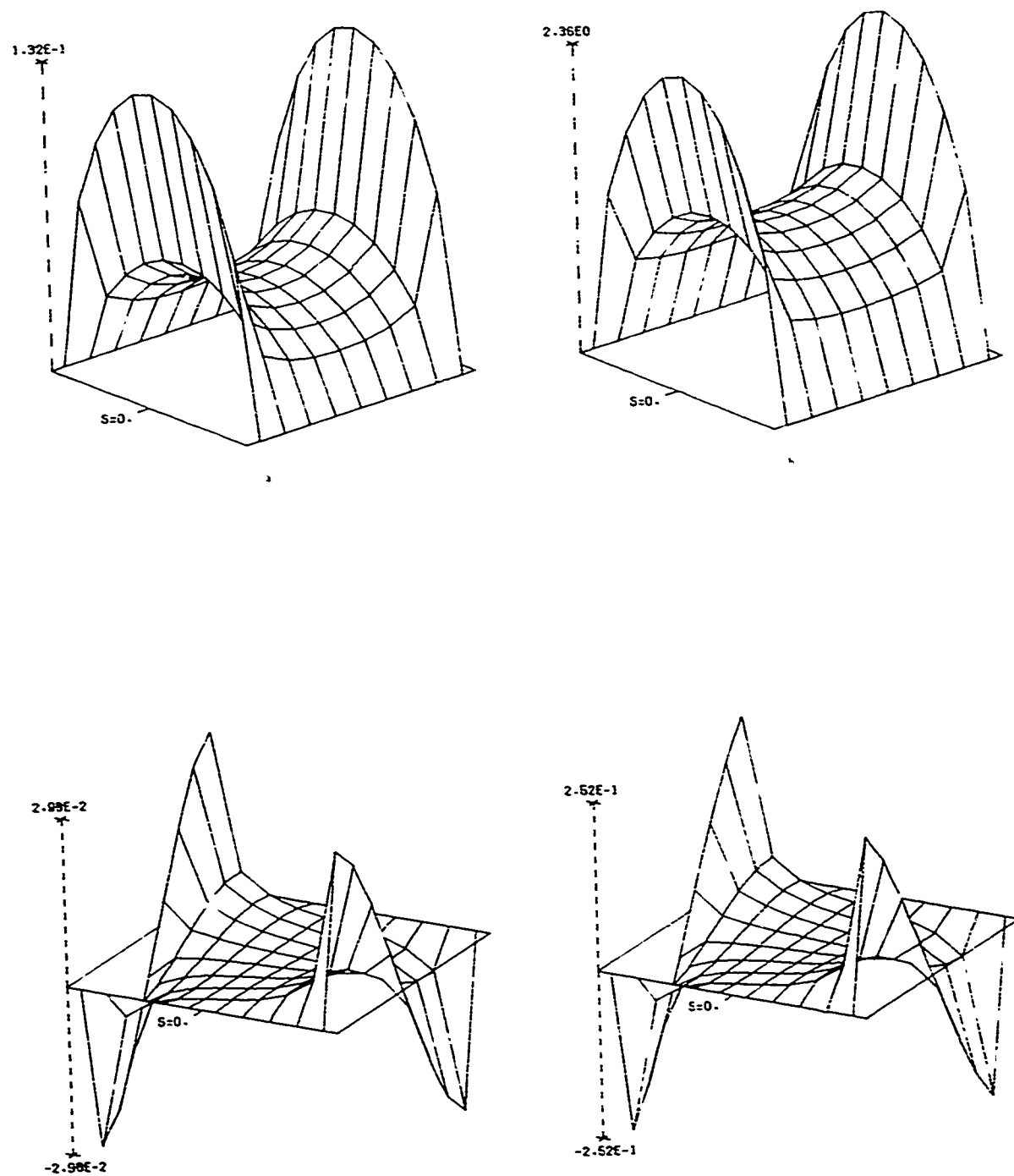


Figure 5.2. Current induced on a square plate, $S_x = 0.15\lambda$,
 $y_d = 0.15\lambda$, $\theta = 0^\circ$, $\phi = 0^\circ$, $H_\theta = 0.0$, $H_\phi = -1.0$, $M = 11$,
 $N = 10$; (a) $\text{Re}(J_s)$, (b) $\text{Im}(J_s)$, (c) $\text{Re}(J_y)$, (d) $\text{Im}(J_y)$.

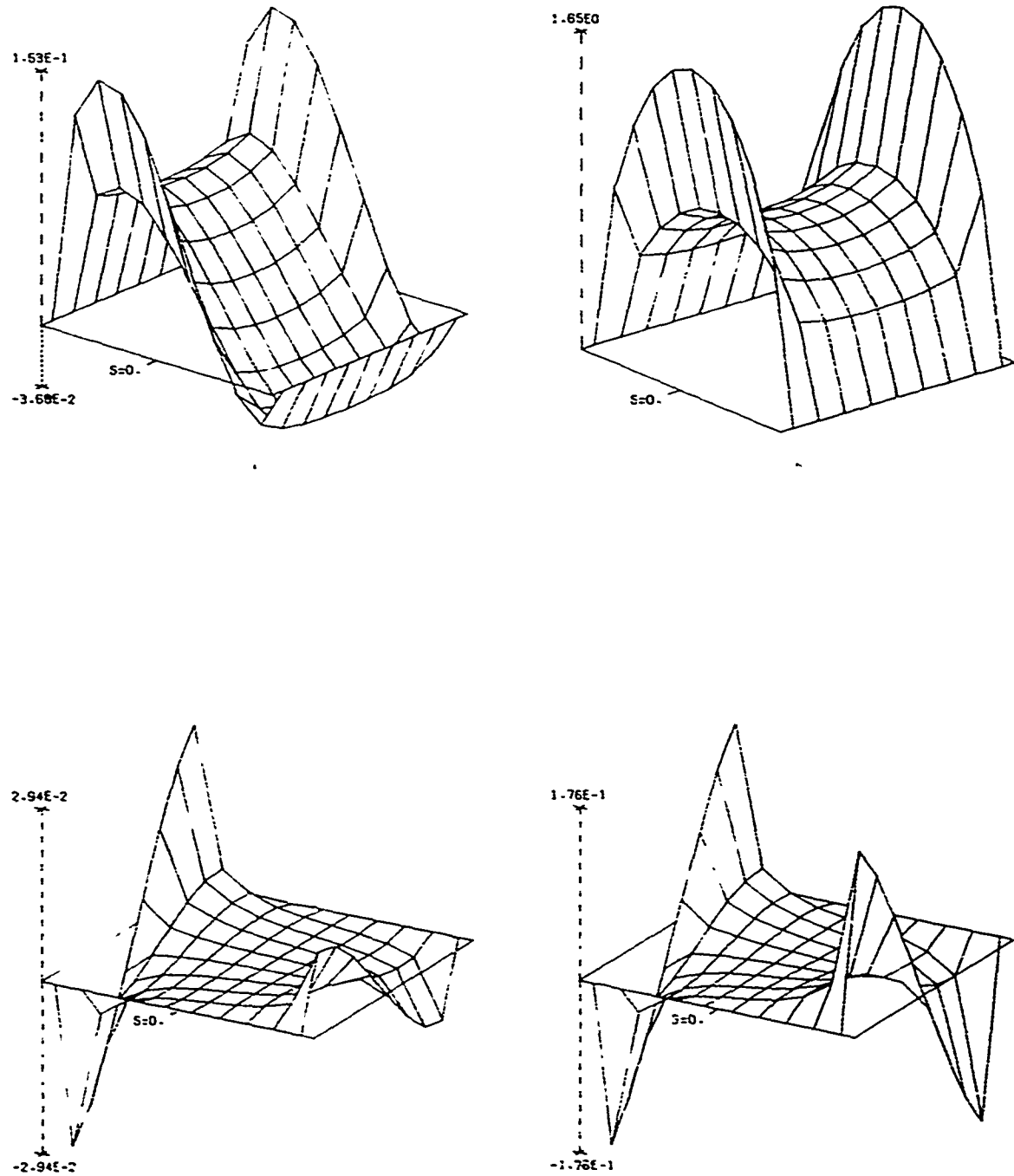


Figure 5.3. Current induced on a square plate, $S_x = 0.15\lambda$,
 $Y_d = 0.15\lambda$, $\theta = 45^\circ$, $c = 0^\circ$, $H_\theta = 0.0$, $H_\phi = -1.0$, $M = 11$,
 $N = 10$; (a) $\text{Re}(J_s)$, (b) $\text{Im}(J_s)$, (c) $\text{Re}(J_y)$, (d) $\text{Im}(J_y)$.

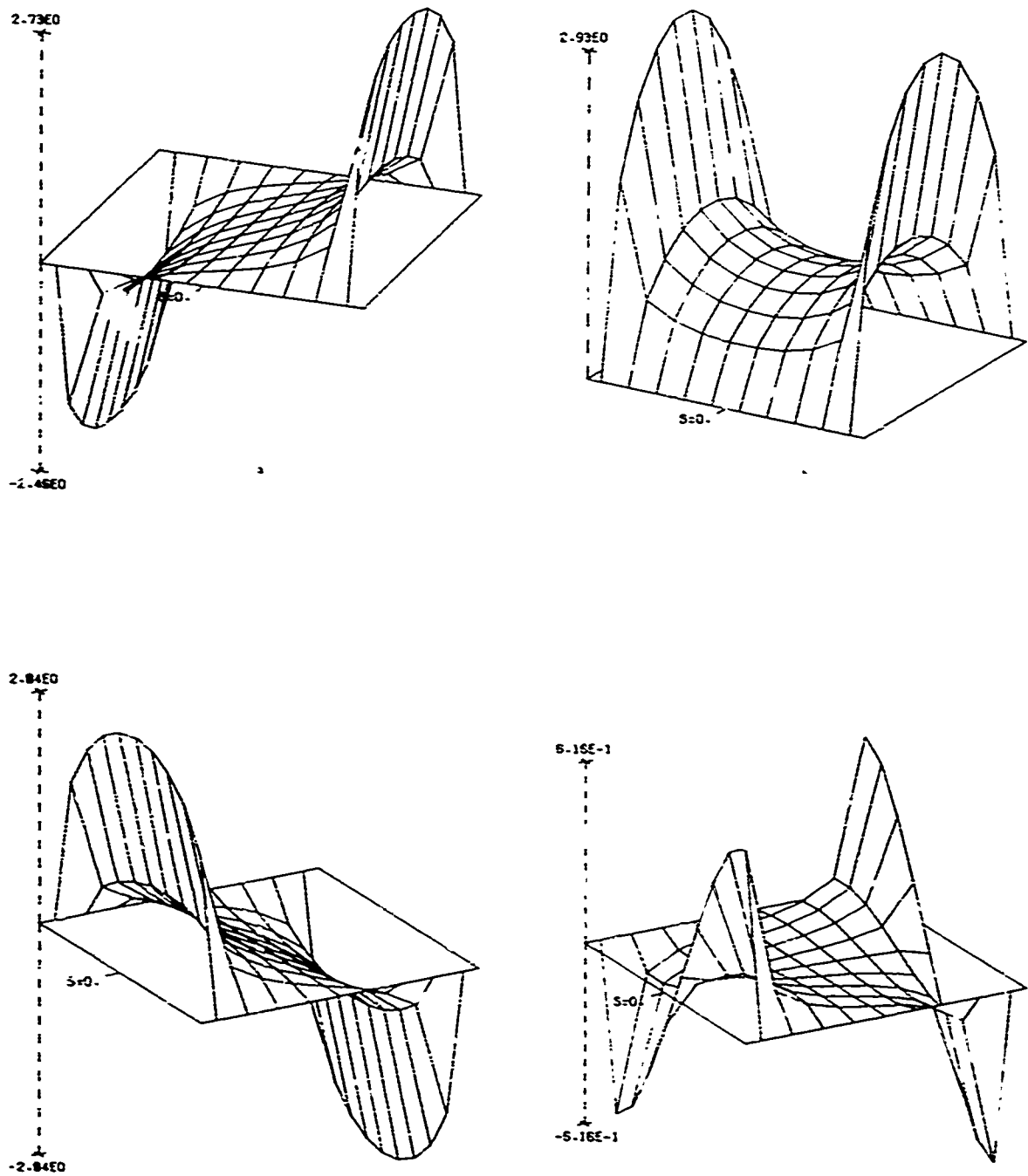


Figure 5.4. Current induced on a square plate, $S_x = 0.15\lambda$,
 $y_d = 0.15\lambda$, $\theta = 45^\circ$, $\phi = 0^\circ$, $H_a = 1.0$, $H_\zeta = 0.0$, $M = 11$,
 $N = 10$; (a) $\text{Re}(J_y)$, (b) $\text{Im}(J_y)$, (c) $\text{Re}(J_s)$, (d) $\text{Im}(J_s)$.

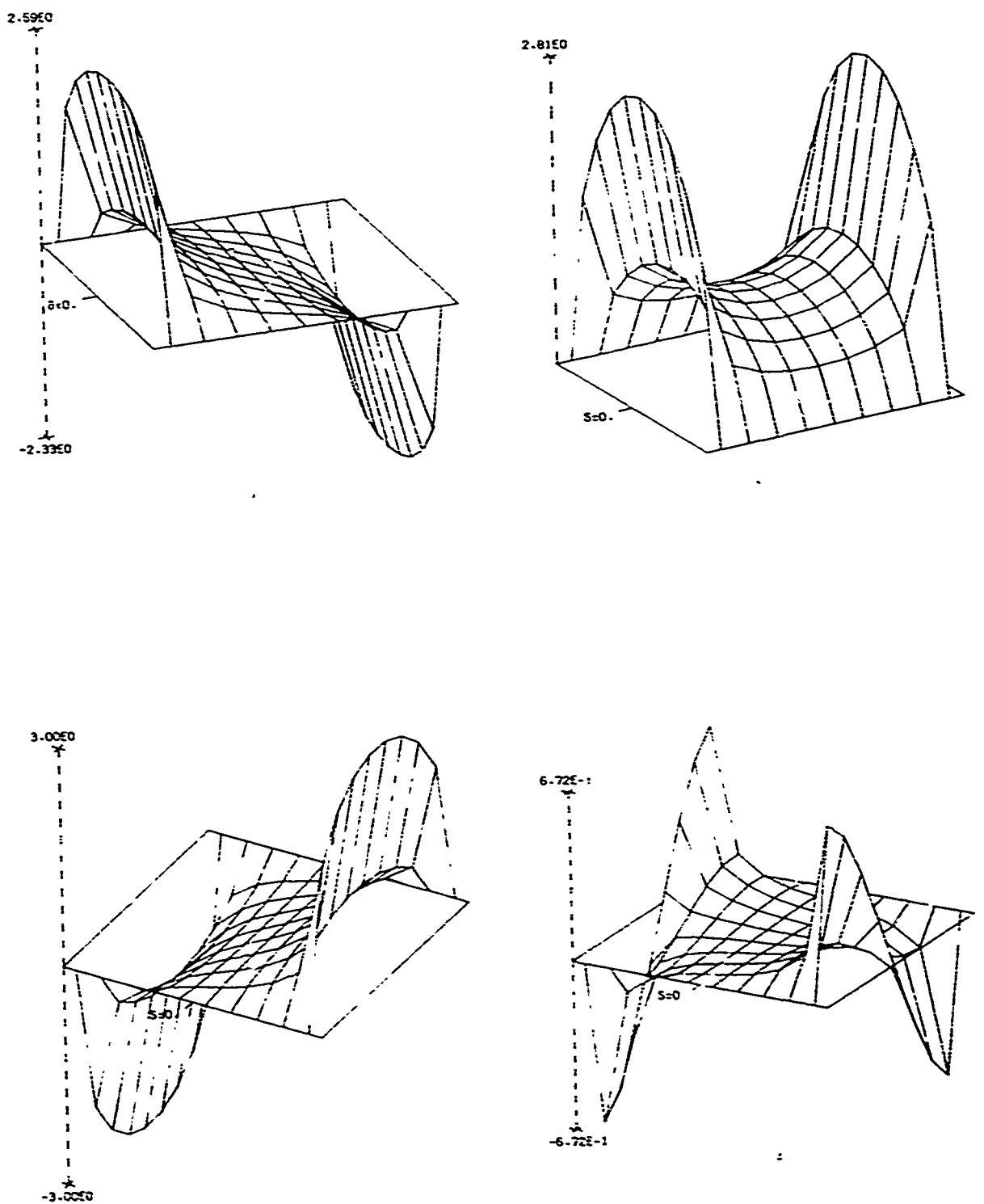


Figure 5.5. Current induced on a square plate, $S_x = 0.15\lambda$,
 $V_d = 0.15\lambda$, $\theta = 45^\circ$, $\phi = 270^\circ$, $H_z = 1.0$, $H_o = 0.0$, $M = 11$,
 $N = 10$; (a) $\text{Re}(J_s)$, (b) $\text{Im}(J_s)$, (c) $\text{Re}(J_y)$, (d) $\text{Im}(J_y)$.

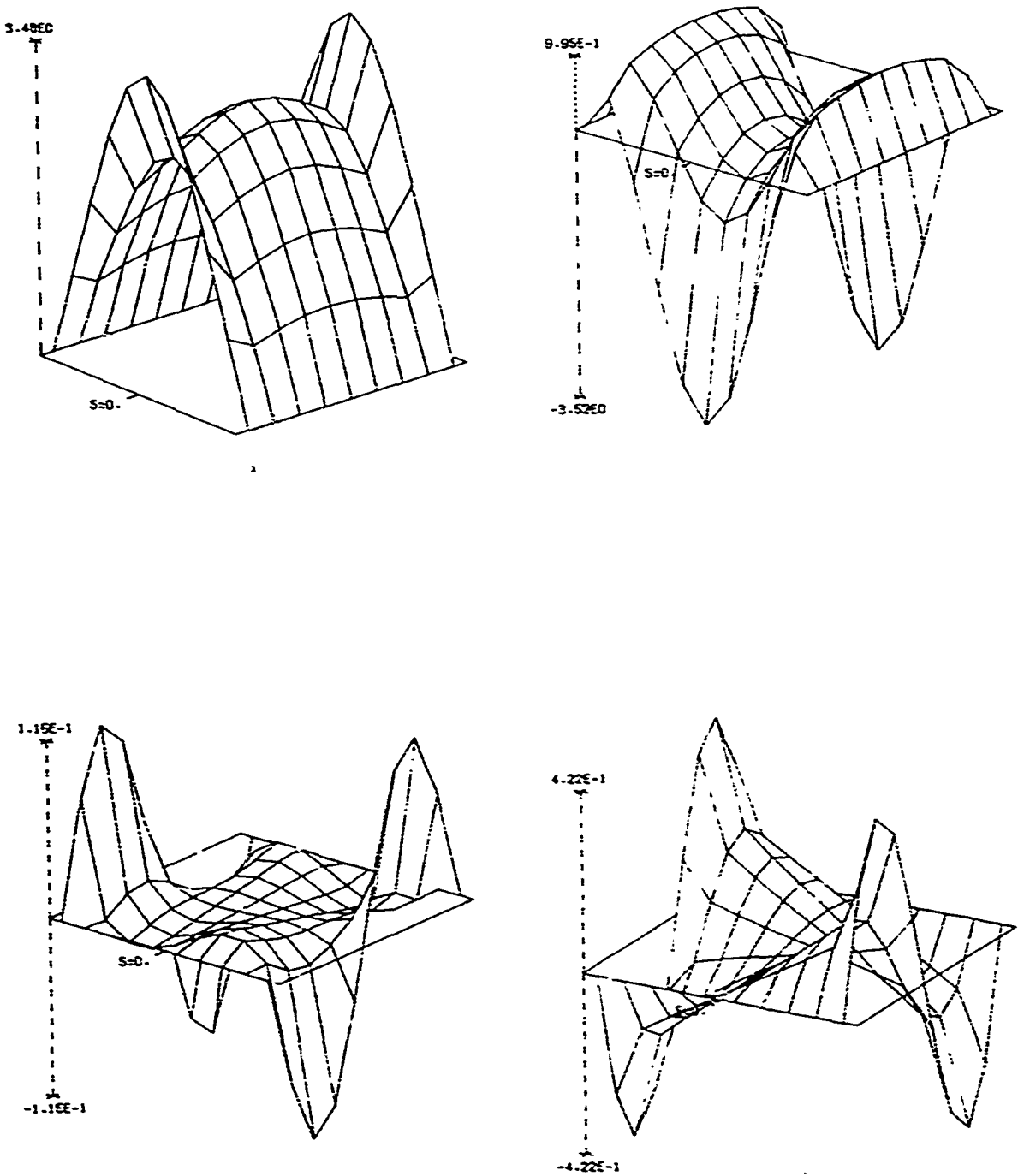


Figure 5.6. Current induced on a square plate, $S_x = 1.0\lambda$, $V_d = 1.0\lambda$,
 $\alpha = 0^\circ$, $\varphi = 0^\circ$, $H_x = 0.0$, $H_y = -1.0$, $M = 11$, $N = 10$;
(a) $\operatorname{Re}(J_s)$, (b) $\operatorname{Im}(J_s)$, (c) $\operatorname{Re}(J_v)$, (d) $\operatorname{Im}(J_v)$.

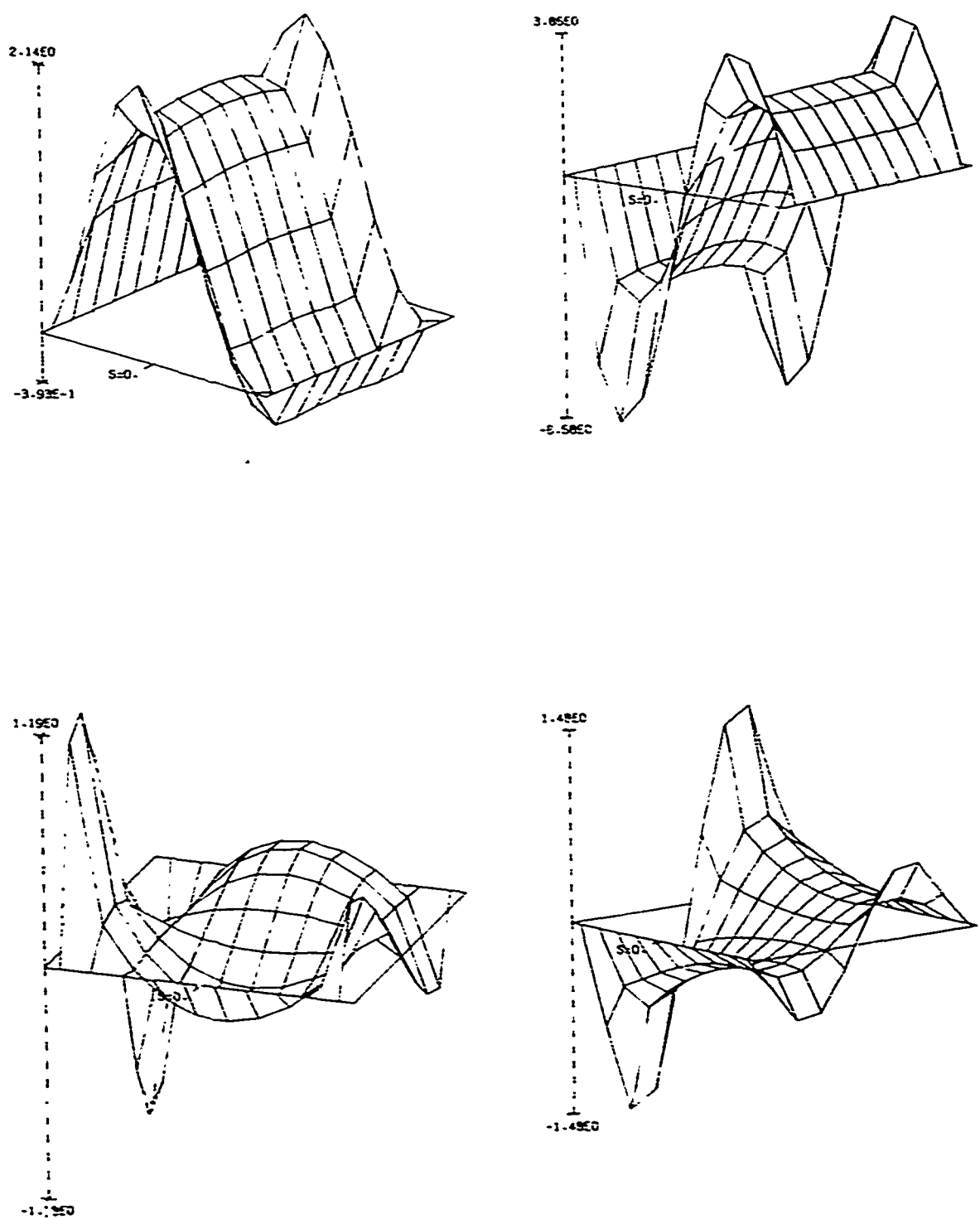


Figure 5.7. Current induced on a square plate, $S_x = 1.0\lambda$, $Y_d = 1.0^\circ$,
 $\theta = 45^\circ$, $\phi = 0^\circ$, $H_a = 0.0$, $H_0 = -1.0$, $M = 11$, $N = 10$;
(a) $\text{Re}(J_s)$, (b) $\text{Im}(J_s)$, (c) $\text{Re}(J_v)$, (d) $\text{Im}(J_v)$.

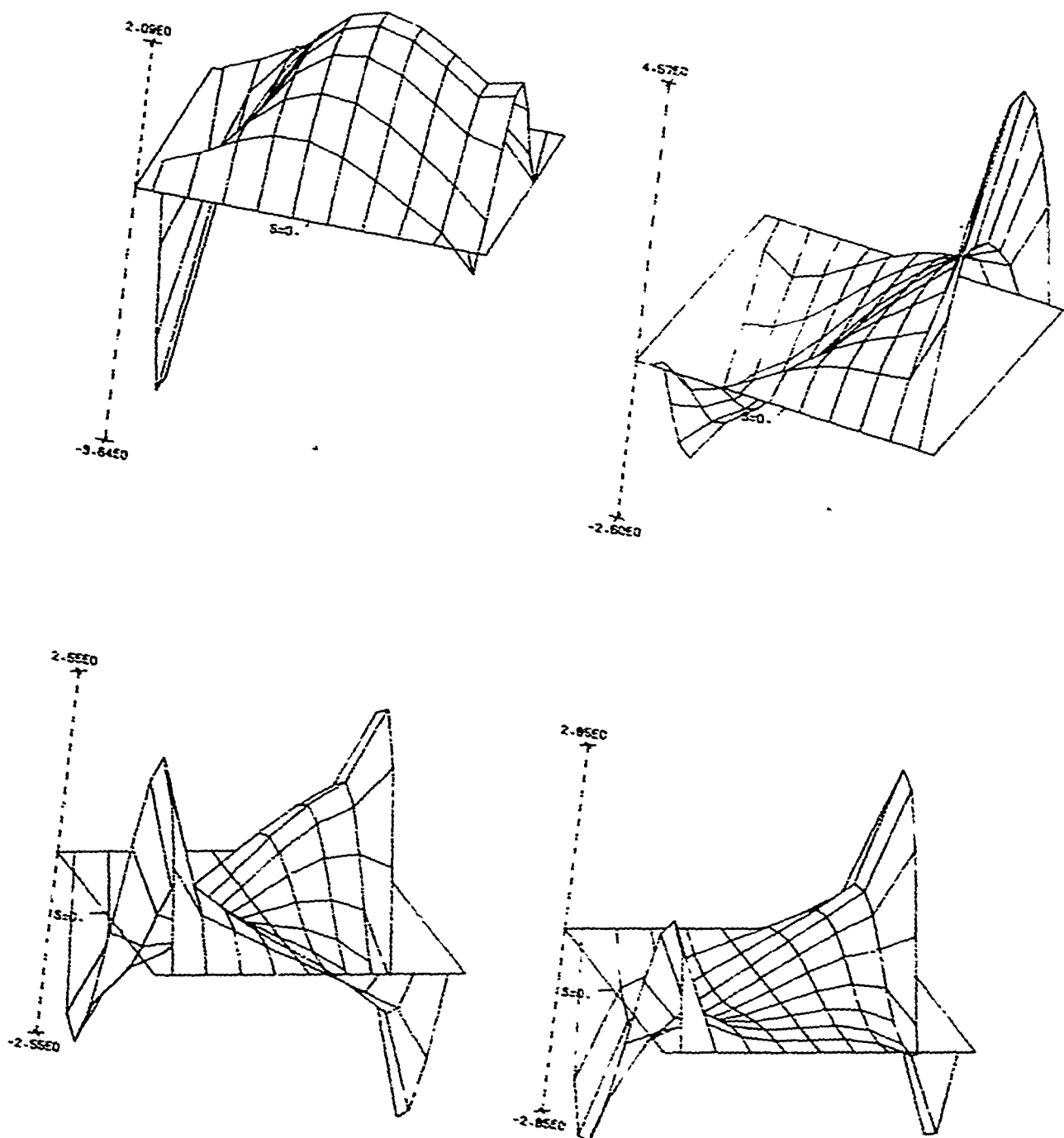


Figure 5.8. Current induced on a square plate, $S_x = 1.0$, $S_y = 1.0$,
 $\theta = 45^\circ$, $\varphi = 0^\circ$, $H_0 = 1.0$, $H_d = 0.0$, $M = 11$, $N = 10$;
(a) $\text{Re}(J_y)$, (b) $\text{Im}(J_y)$, (c) $\text{Re}(J_s)$, (d) $\text{Im}(J_s)$.

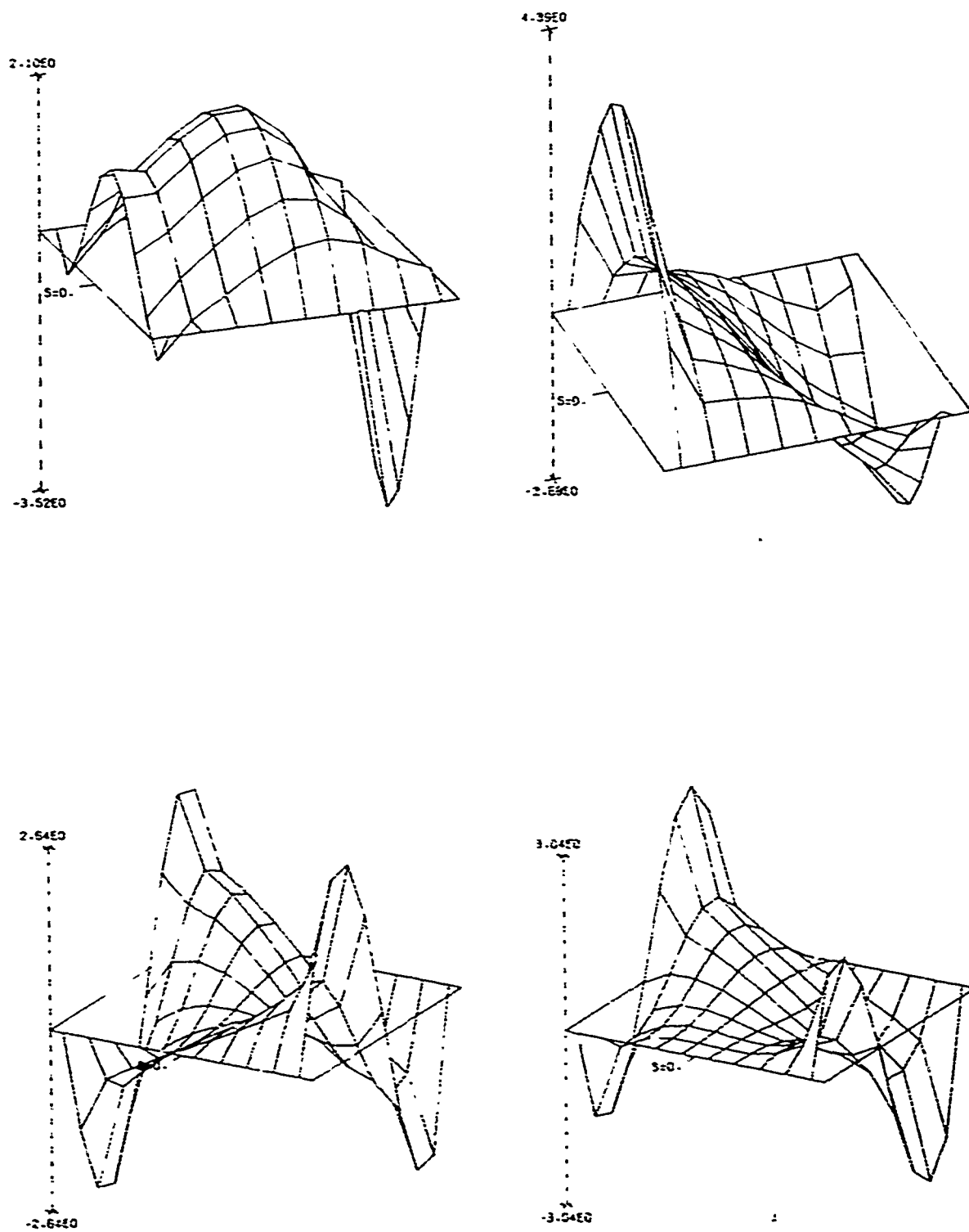


Figure 5.9. Current induced on a square plate, $S_x = 1.0\lambda$, $Y_d = 1.0\lambda$,
 $\phi = 45^\circ$, $\delta = 270^\circ$, $H_\xi = 1.0$, $H_c = 0.6$, $M = 11$, $N = 10$;
(a) $\text{Re}(J_s)$, (b) $\text{Im}(J_s)$, (c) $\text{Re}(J_v)$, (d) $\text{Im}(J_v)$.

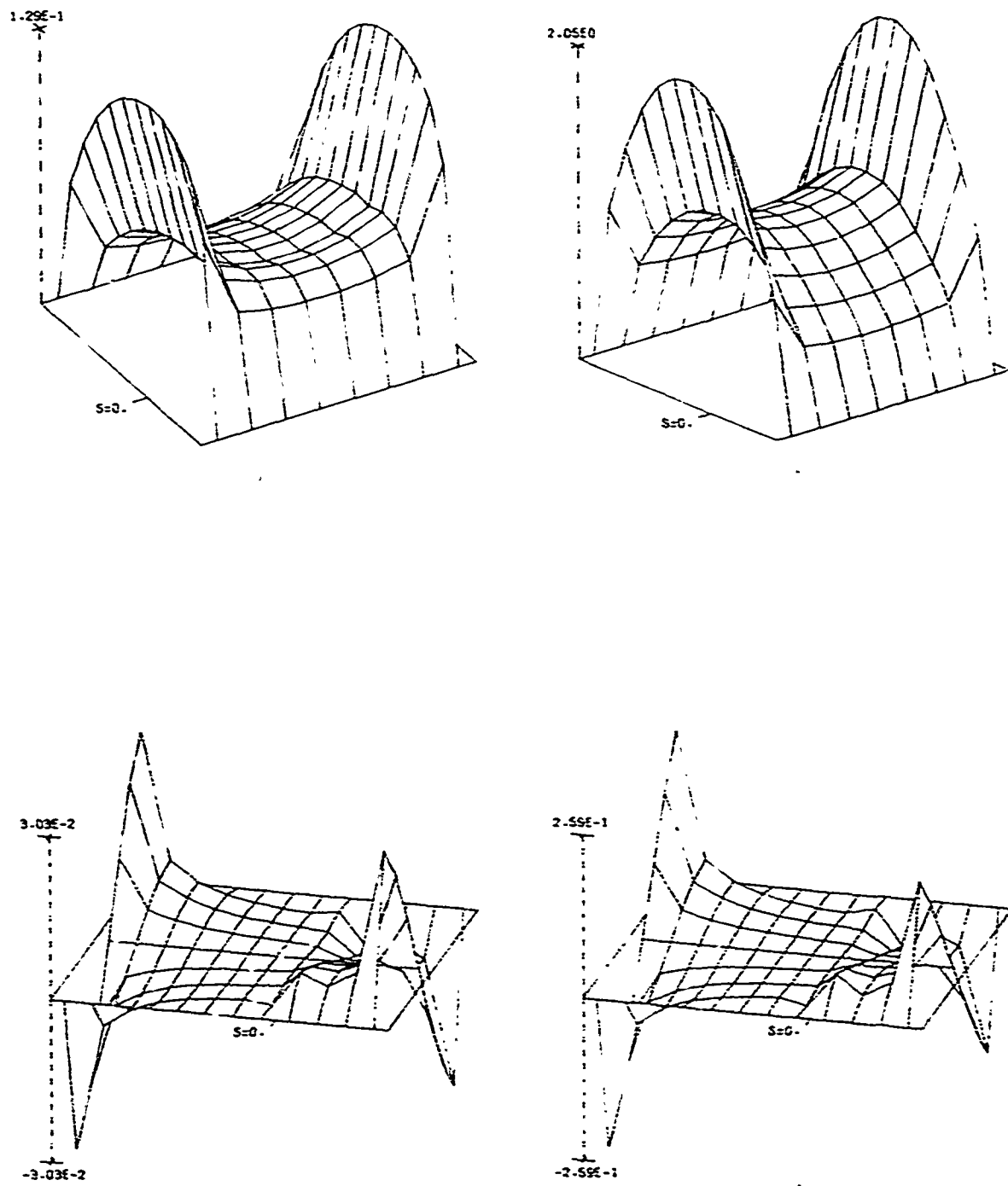


Figure 5.10. Current induced on a rectangular plate bent at $s = 0$,
 $S_x = 0.10\lambda$, $S_c = 0.05\lambda$, $Y_d = 0.15\lambda$, $\alpha = 50^\circ$, $\theta = 0^\circ$,
 $\delta = 0^\circ$, $H_x = 0.0$, $H_d = -1.0$, $NPB = 9$, $MFB = 5$, $N = 9$;
(a) $\operatorname{Re}(J_s)$, (b) $\operatorname{Im}(J_s)$, (c) $\operatorname{Re}(J_y)$, (d) $\operatorname{Im}(J_y)$.

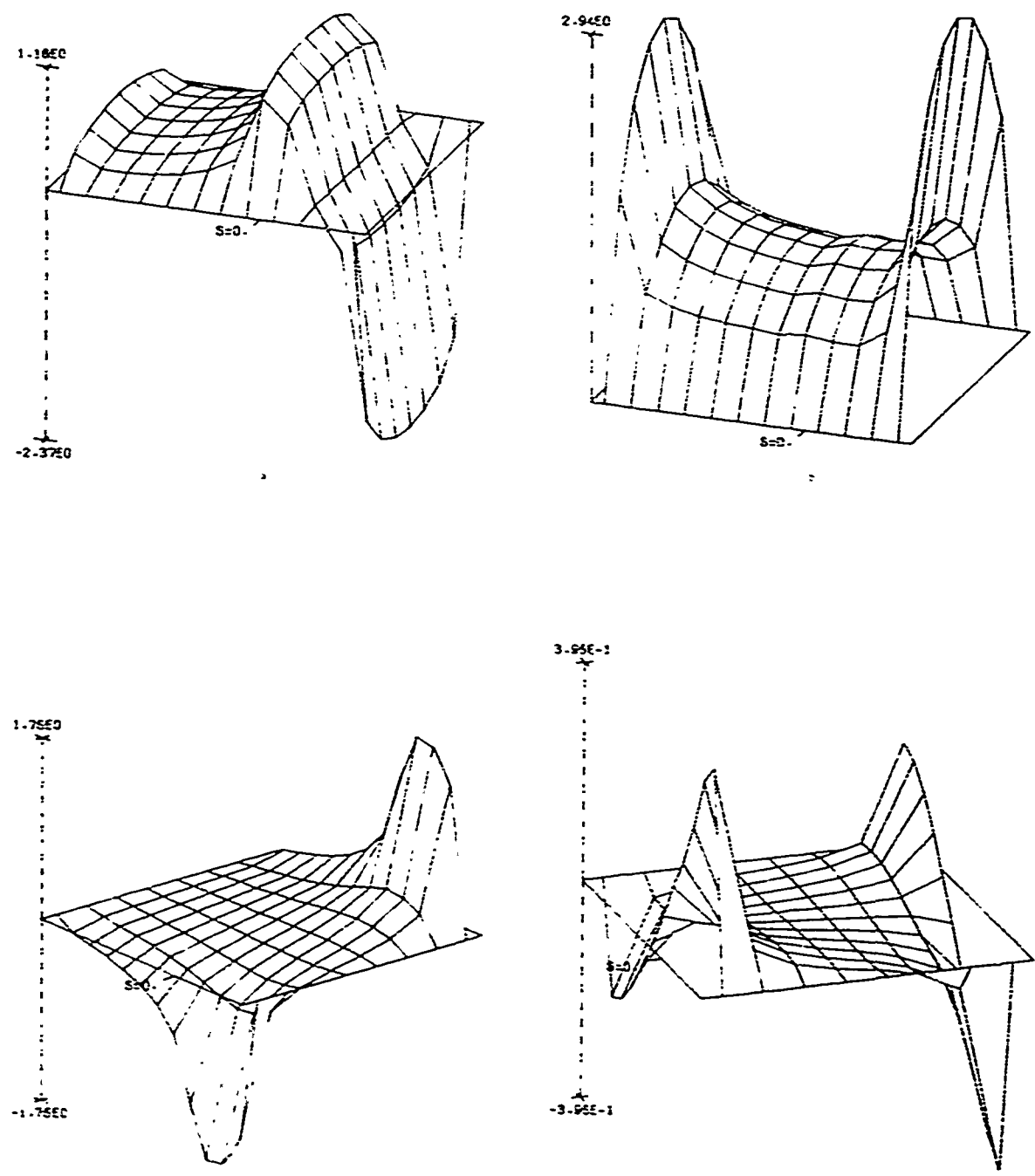


Figure 5.11. Current induced on a rectangular plate bent at $s = 0$,
 $S_x = 0.10\lambda$, $S_c = 0.05\lambda$, $Y_d = 0.15\lambda$, $\alpha = 50^\circ$, $\theta = 0^\circ$,
 $\phi = 0^\circ$, $H_g = 1.0$, $H_j = 0.0$, MPB = 0, MFB = 5, N = 9;
 (a) $\text{Re}(J_y)$, (b) $\text{Im}(J_y)$, (c) $\text{Re}(J_s)$, (d) $\text{Im}(J_s)$.

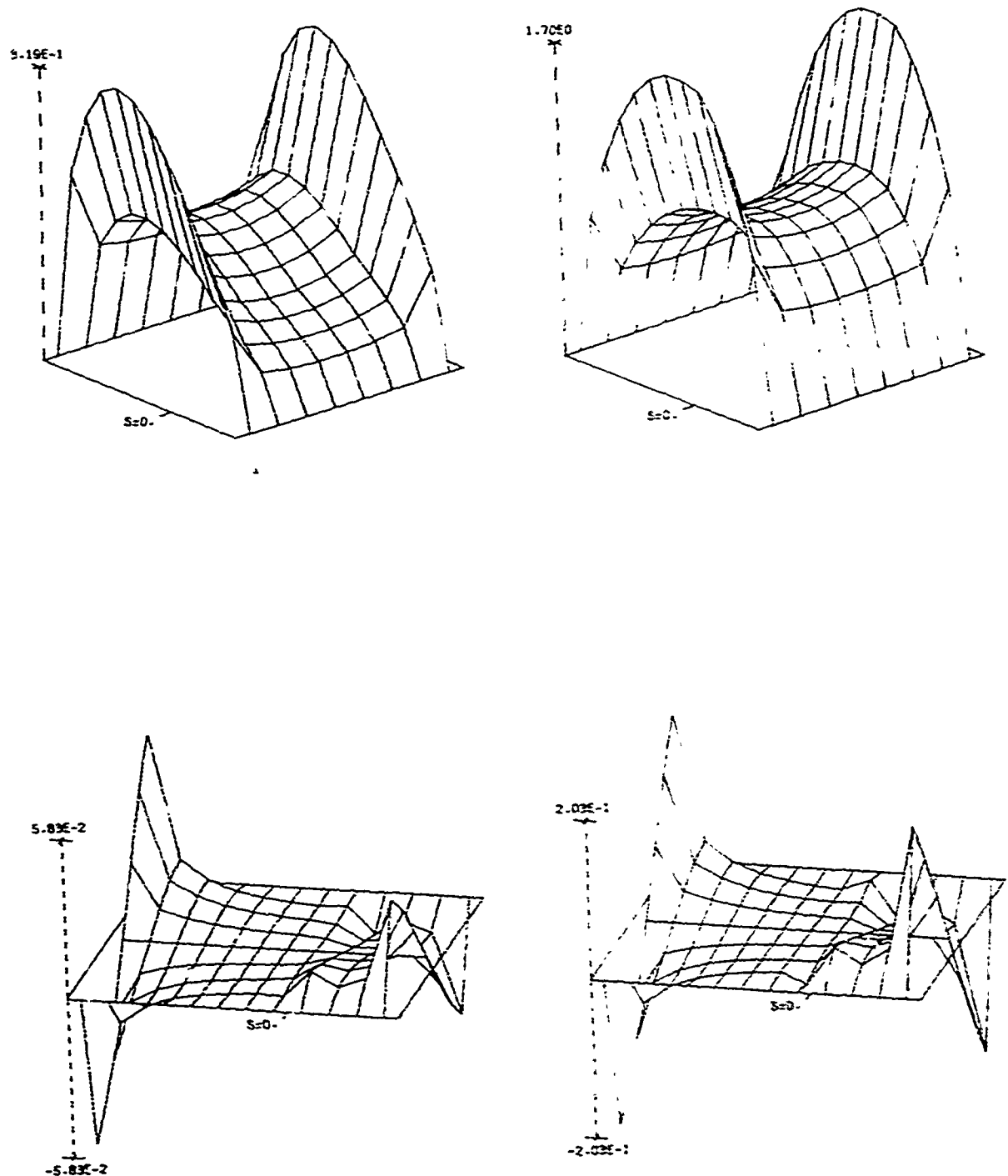


Figure 5.12. Current induced on a rectangular plate bent at $s = 0$,
 $S_x = 0.10\lambda$, $S_c = 0.05\lambda$, $\gamma_d = 0.15\lambda$, $\alpha = 50^\circ$, $\beta = 45^\circ$,
 $\phi = 0^\circ$, $H_0 = 0.0$, $H_z = -1.0$, MFB = 9, MFB = 5, N = 9;
(a) $\text{Re}(J_s)$, (b) $\text{Im}(J_s)$, (c) $\text{Re}(J_y)$, (d) $\text{Im}(J_y)$.

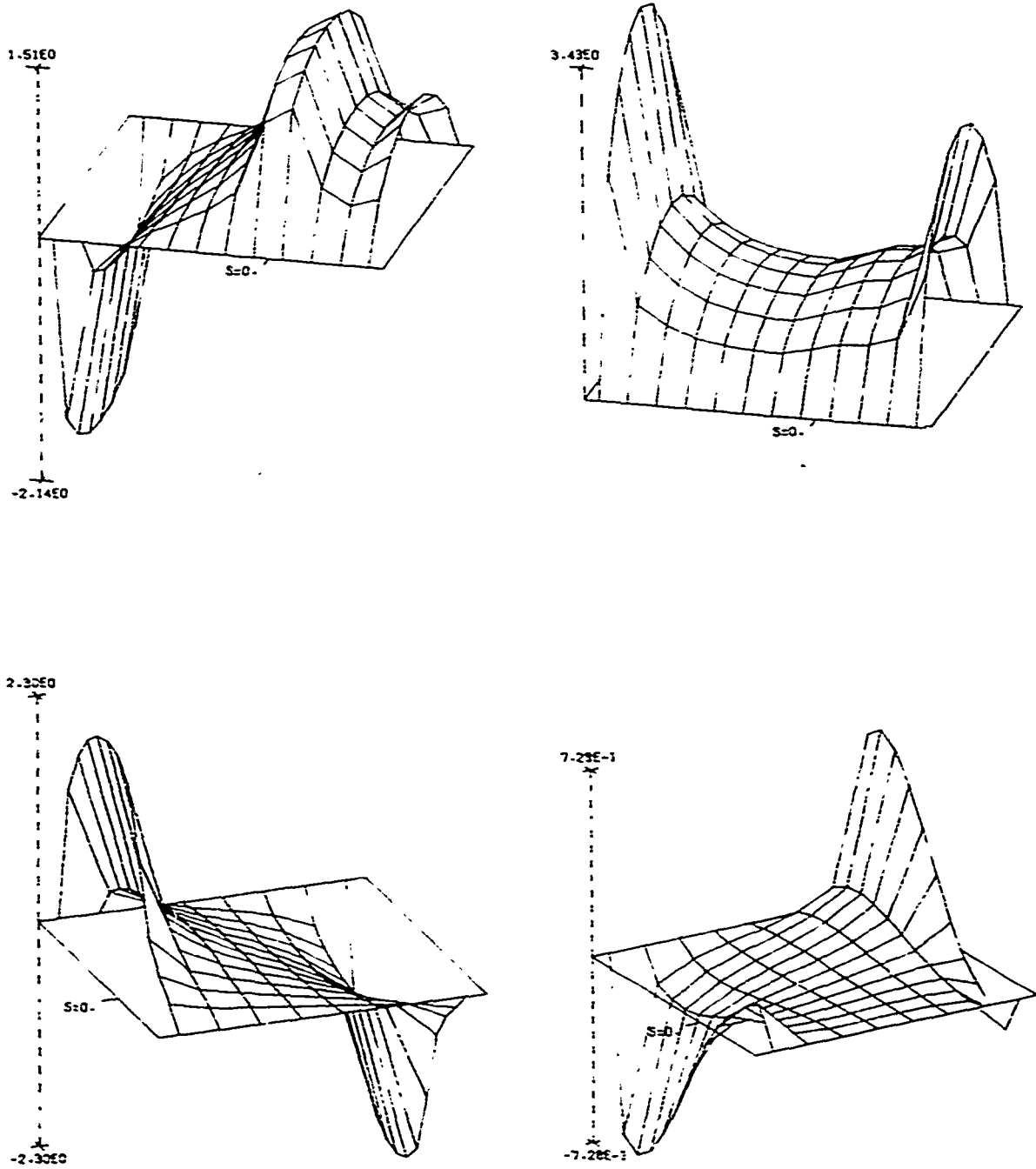


Figure 5.13. Current induced on a rectangular plate bent at $s = 0$,
 $S_x = 0.10$, $S_c = 0.05$, $Y_d = 0.15$, $\alpha = 50^\circ$, $\theta = 45^\circ$,
 $\beta = 0^\circ$, $H_0 = 1.0$, $H_c = 0.0$, MPB = 9, MFB = 5, N = 9;
(a) $\text{Re}(J_y)$, (b) $\text{Im}(J_y)$, (c) $\text{Re}(J_s)$, (d) $\text{Im}(J_s)$.

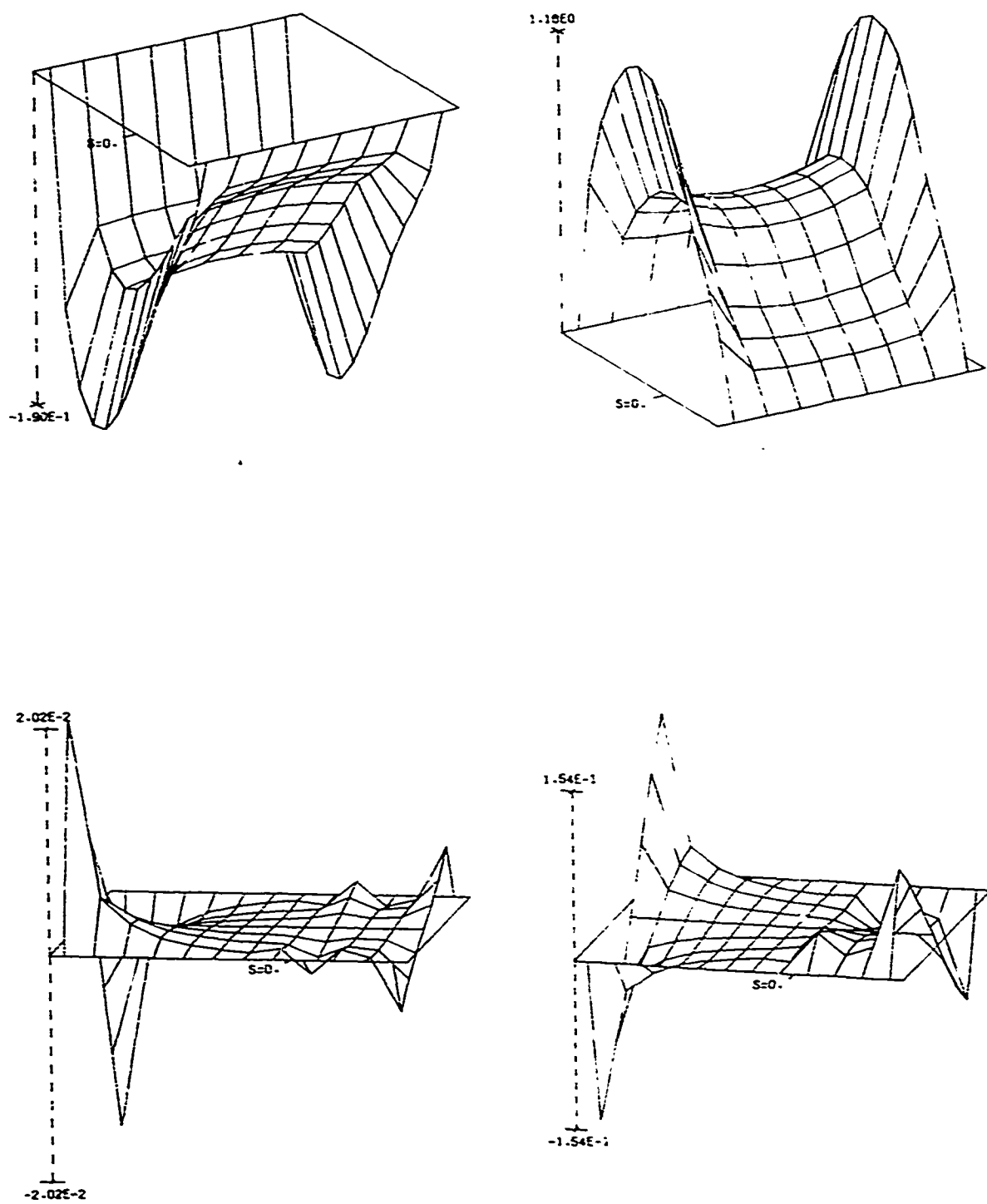


Figure 5.14. Current induced on a rectangular plate bent at $s = 0$,

$S_x = 0.10\lambda$, $S_c = 0.05\lambda$, $Y_d = 0.15\lambda$, $\alpha = 50^\circ$, $\theta = 45^\circ$,
 $\phi = 180^\circ$, $H_e = 0.0$, $H_d = 1.0$, MPB = 9, MFB = 5, N = 9;

(a) $\text{Re}(J_s)$, (b) $\text{Im}(J_s)$, (c) $\text{Re}(J_y)$, (d) $\text{Im}(J_y)$.

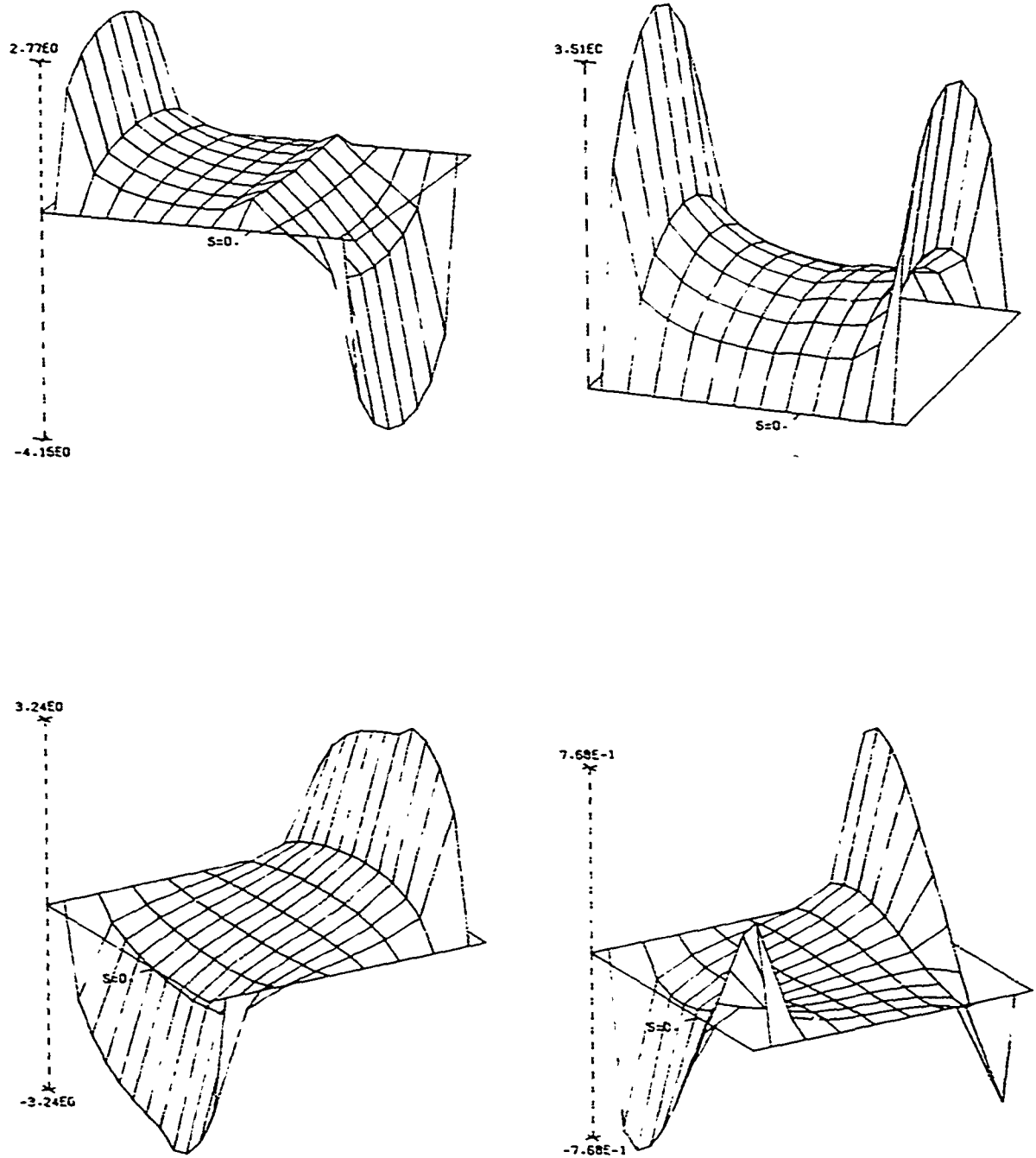


Figure 5.15. Current induced on a rectangular plate bent at $s = 0$,
 $S_x = 0.10\lambda$, $S_c = 0.0\lambda$, $Y_d = 0.15\lambda$, $\alpha = 50^\circ$, $\theta = 45^\circ$,
 $\delta = 180^\circ$, $H_0 = -1.0$, $I_s = 0.0$, MPB = 9, MFB = 5, N = 9;
(a) $\text{Re}(J_y)$, (b) $\text{Im}(J_y)$, (c) $\text{Re}(J_s)$, (d) $\text{Im}(J_s)$.

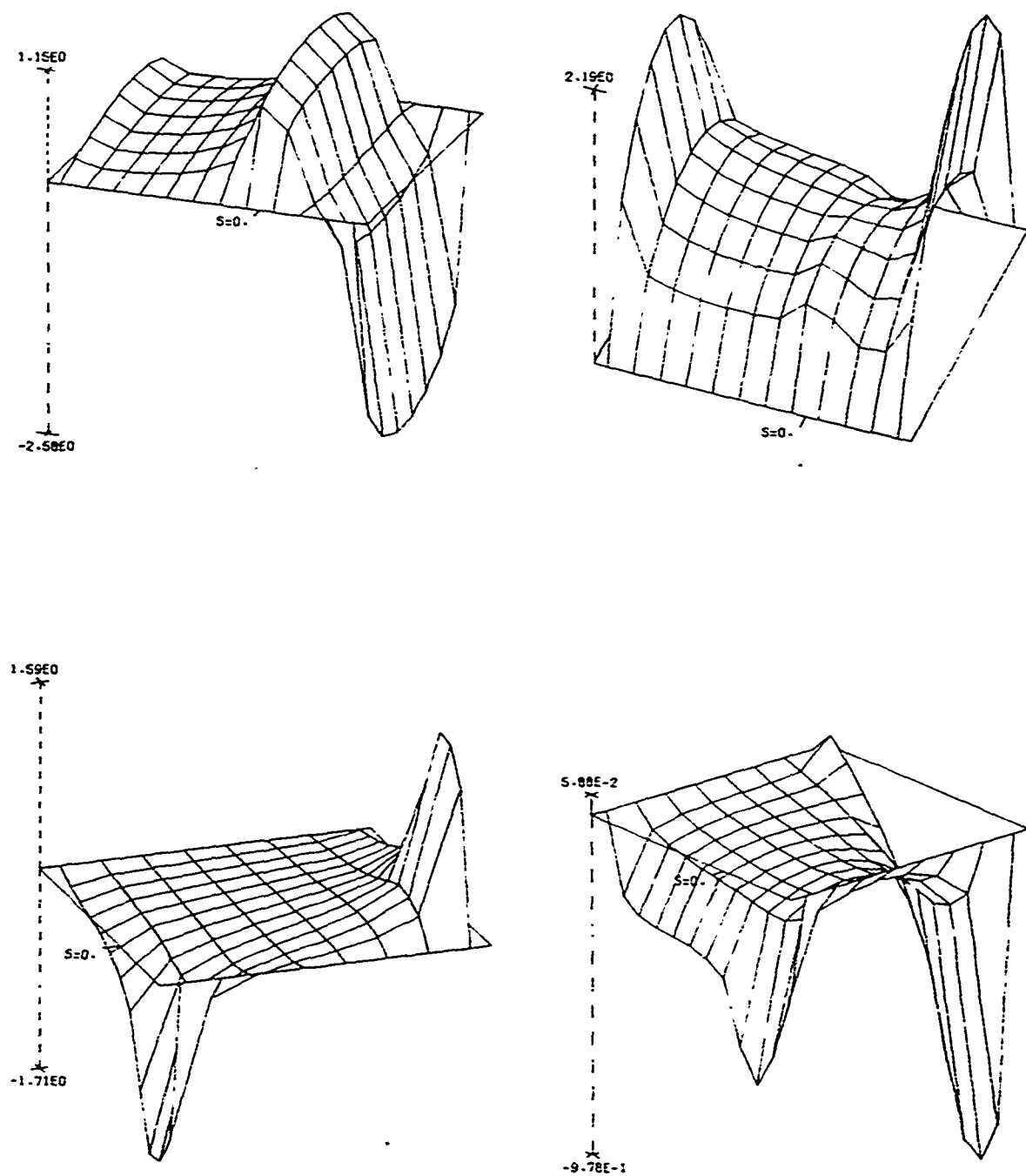


Figure 5.16. Current induced on a rectangular plate bent at $s = 0$,
 $S_x = 0.10\lambda$, $S_c = 0.05\lambda$, $Y_d = 0.15^\circ$, $\alpha = 50^\circ$, $\theta = 45^\circ$,
 $\phi = 270^\circ$, $H_\theta = 0.0$, $H_\phi = 1.0$, MPB = 9, MFB = 5, N = 9;
(a) $\text{Re}(J_y)$, (b) $\text{Im}(J_y)$, (c) $\text{Re}(J_s)$, (d) $\text{Im}(J_s)$.

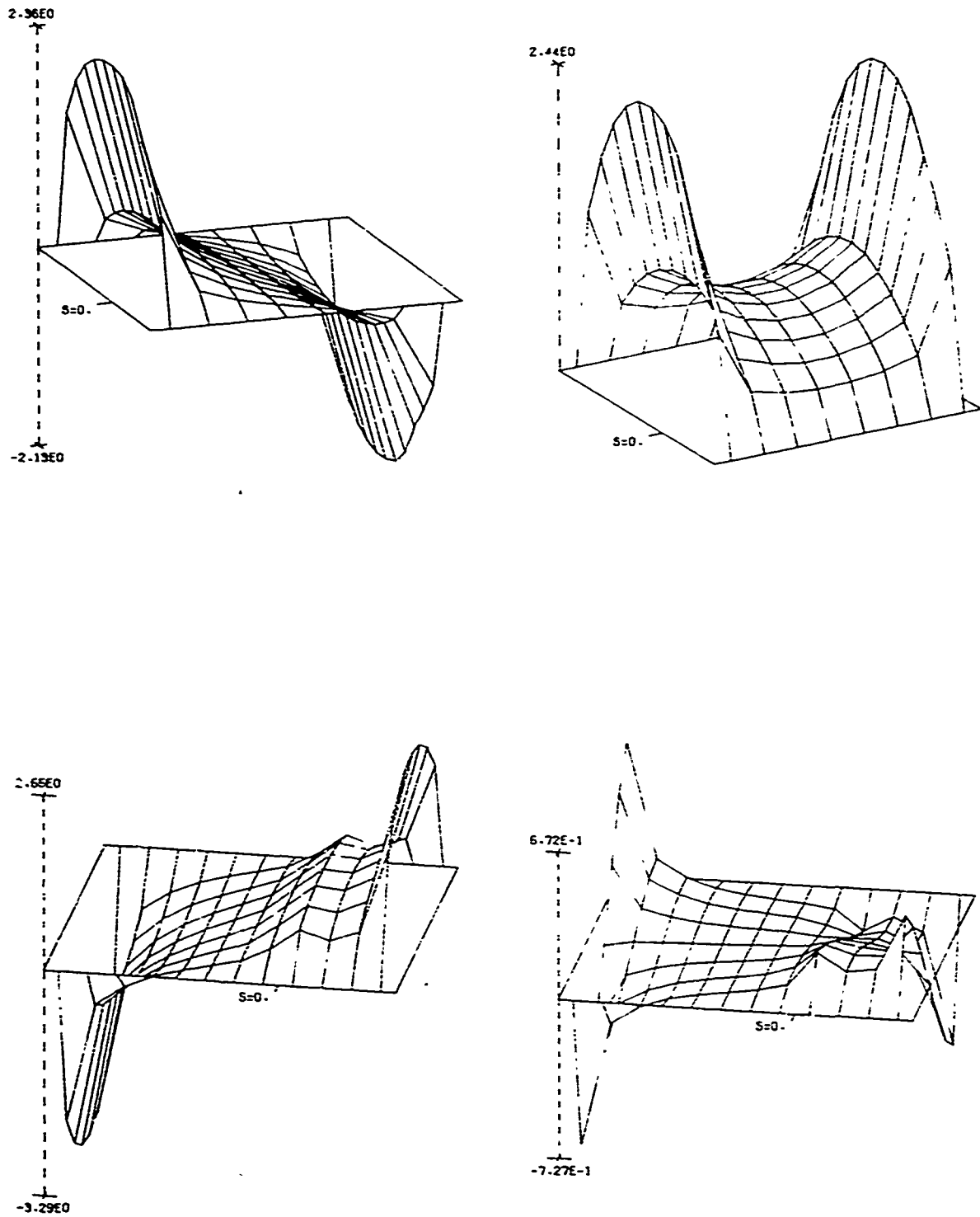


Figure 5.17. Current induced on a rectangular plate bent at $s = 0$,
 $S_x = 0.10\lambda$, $S_c = 0.05\lambda$, $Y_d = 0.15\lambda$, $\alpha = 50^\circ$, $\theta = 45^\circ$,
 $\phi = 270^\circ$, $H_\theta = 1.0$, $H_c = 0.0$, MPB = 9, MFB = 5, N = 9;
 (a) $\text{Re}(J_s)$, (b) $\text{Im}(J_s)$. (c) $\text{Re}(J_v)$, (d) $\text{Im}(J_v)$.

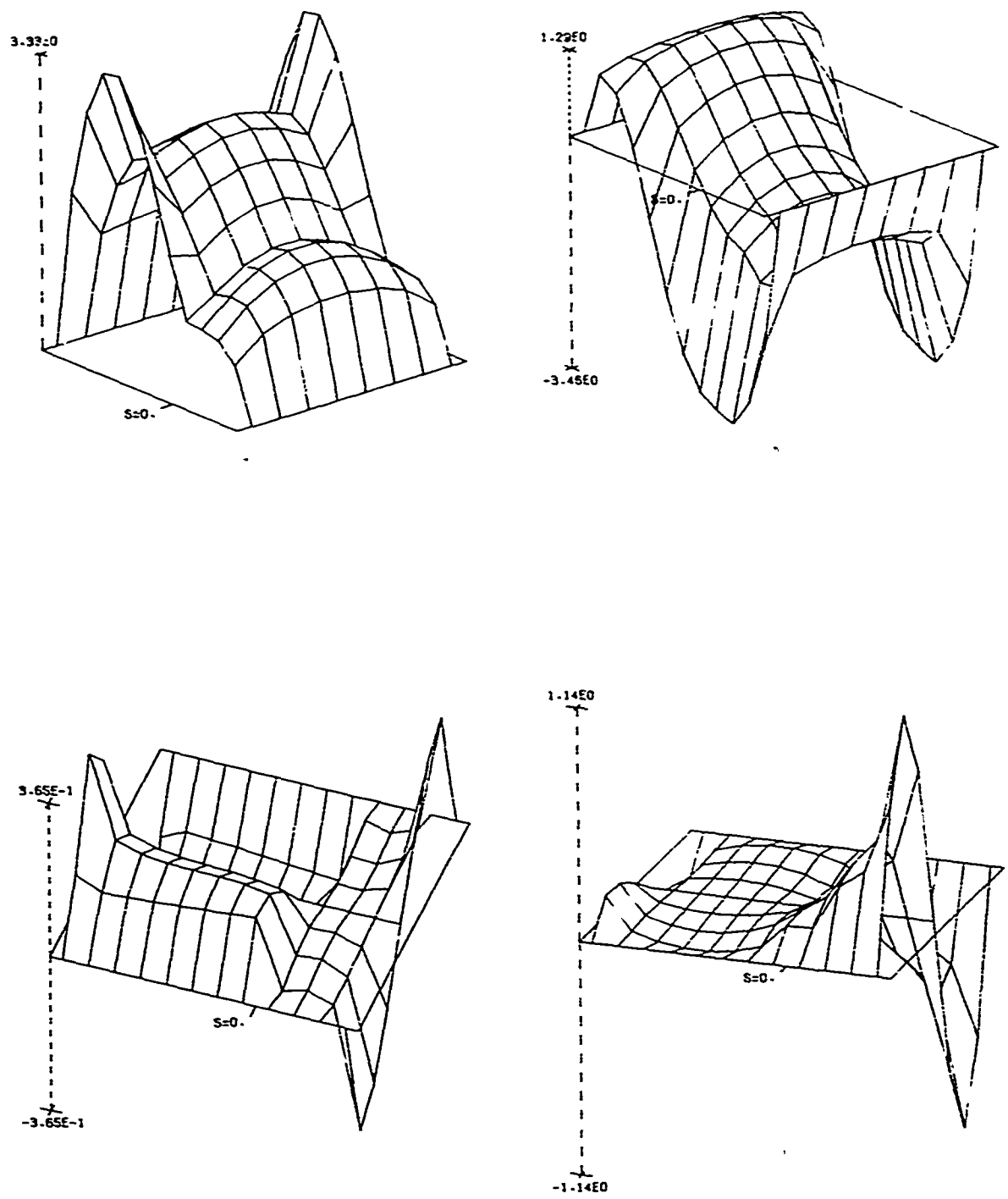


Figure 5.18. Current induced on a rectangular plate bent at $s = 0$,
 $S_x = 0.667\lambda$, $S_c = 0.333\lambda$, $Y_d = 1.0\lambda$, $\alpha = 50^\circ$, $\theta = 0^\circ$,
 $\delta = 0^\circ$, $H_\theta = 0.0$, $H_\phi = -1.0$, MPB = 9, MFB = 5, N = 9;
(a) $\text{Re}(J_s)$, (b) $\text{Im}(J_s)$, (c) $\text{Re}(J_y)$, (d) $\text{Im}(J_y)$.

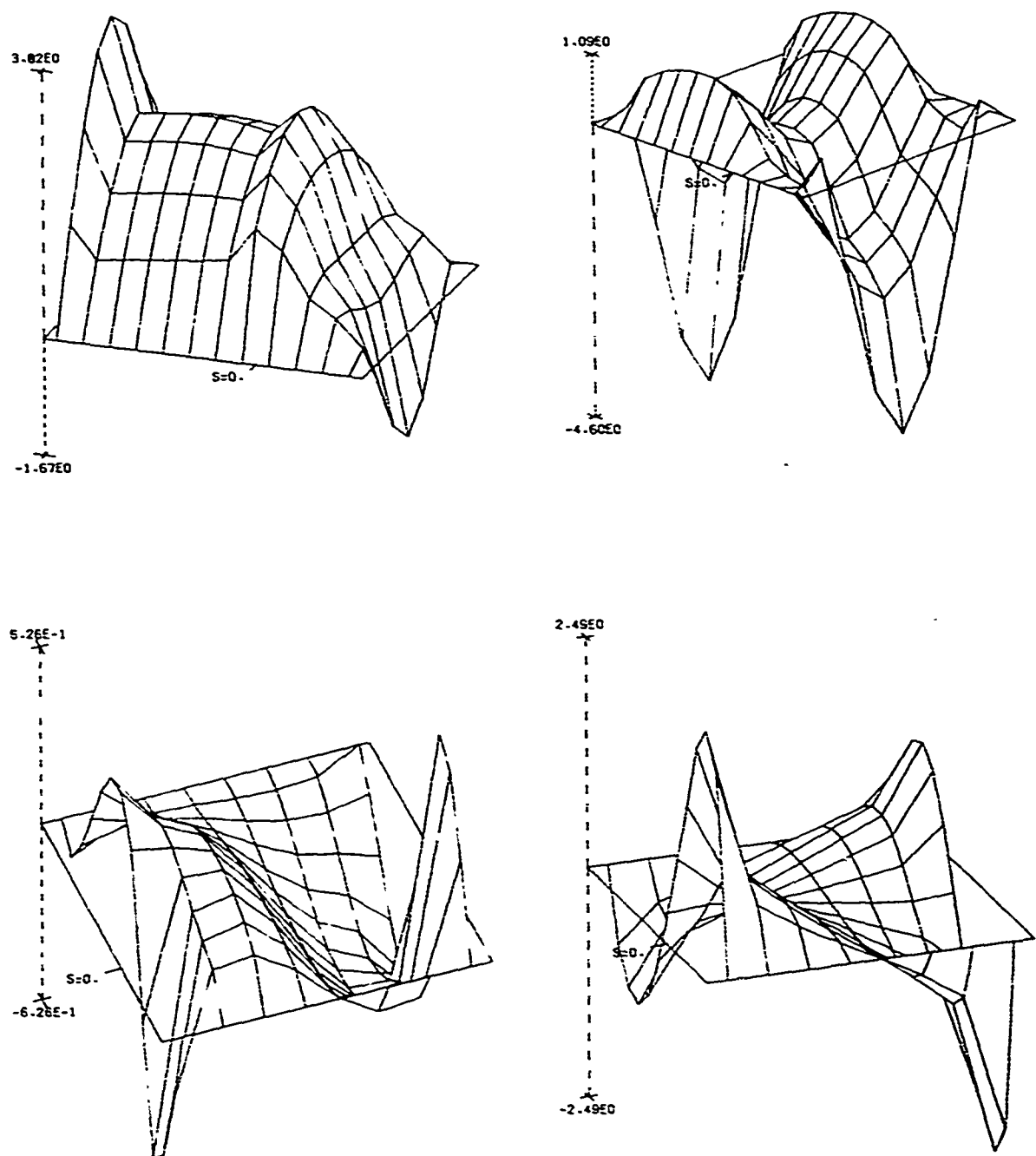


Figure 5.19. Current induced on a rectangular plate bent at $s = 0$,
 $S_x = 0.667\lambda$, $S_c = 0.333\lambda$, $Y_d = 1.0\lambda$, $\alpha = 50^\circ$, $\theta = 0^\circ$,
 $\phi = 0^\circ$, $H_\theta = 1.0$, $H_\phi = 0.0$, MPB = 9, MFB = 5, N = 9;
(a) $\text{Re}(J_y)$, (b) $\text{Im}(J_y)$, (c) $\text{Re}(J_s)$, (d) $\text{Im}(J_s)$.

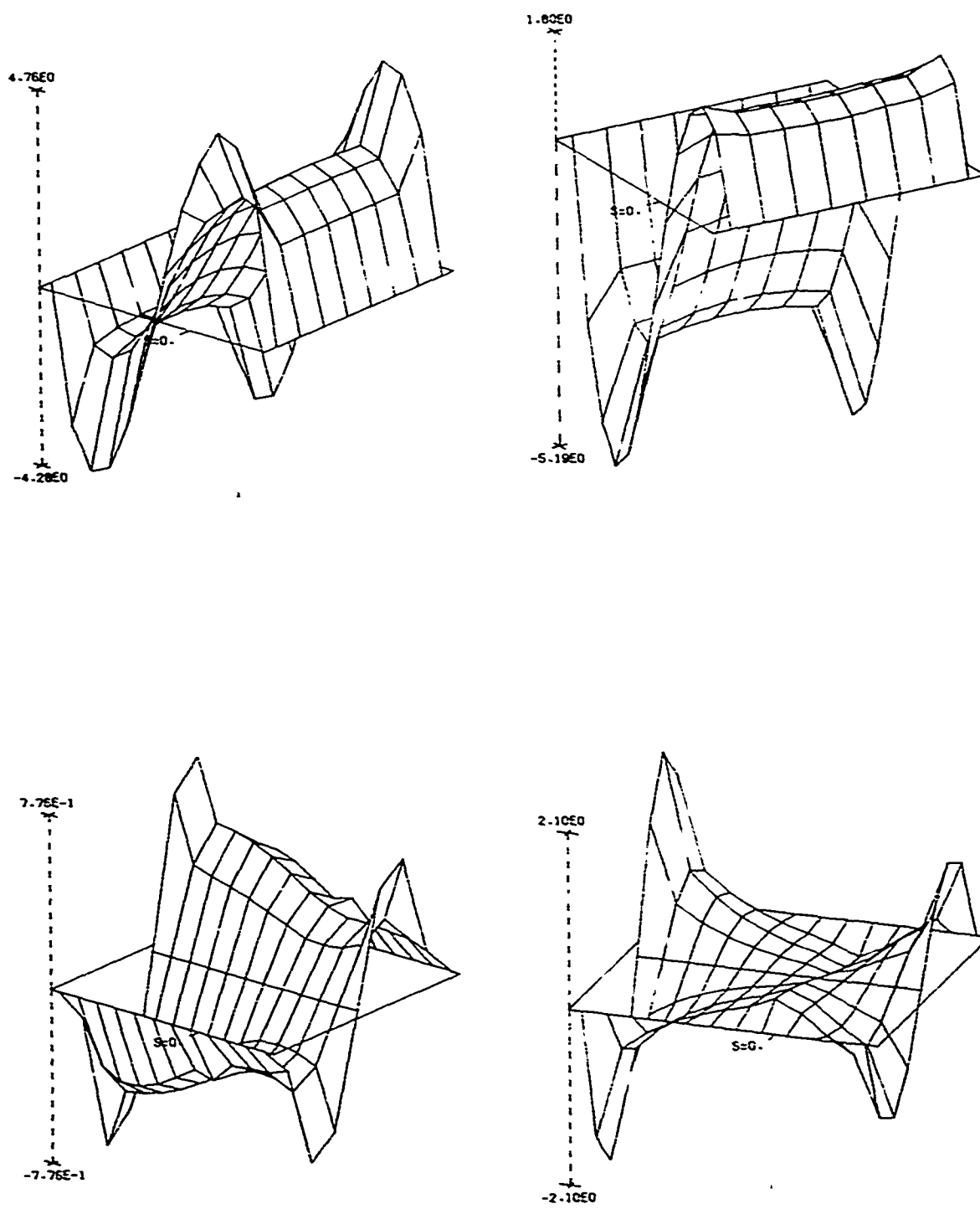


Figure 5.20. Current induced on a rectangular plate bent at $s = 0$,
 $S_x = 0.667\lambda$, $S_c = 0.333\lambda$, $Y_d = 1.0\lambda$, $\alpha = 50^\circ$, $\theta = 45^\circ$,
 $\phi = 0^\circ$, $H_\theta = 0.0$, $H_z = -1.0$, MPB = 9, MFB = 5, N = 9;
 (a) $\text{Re}(J_s)$, (b) $\text{Im}(J_s)$, (c) $\text{Re}(J_y)$, (d) $\text{Im}(J_y)$.

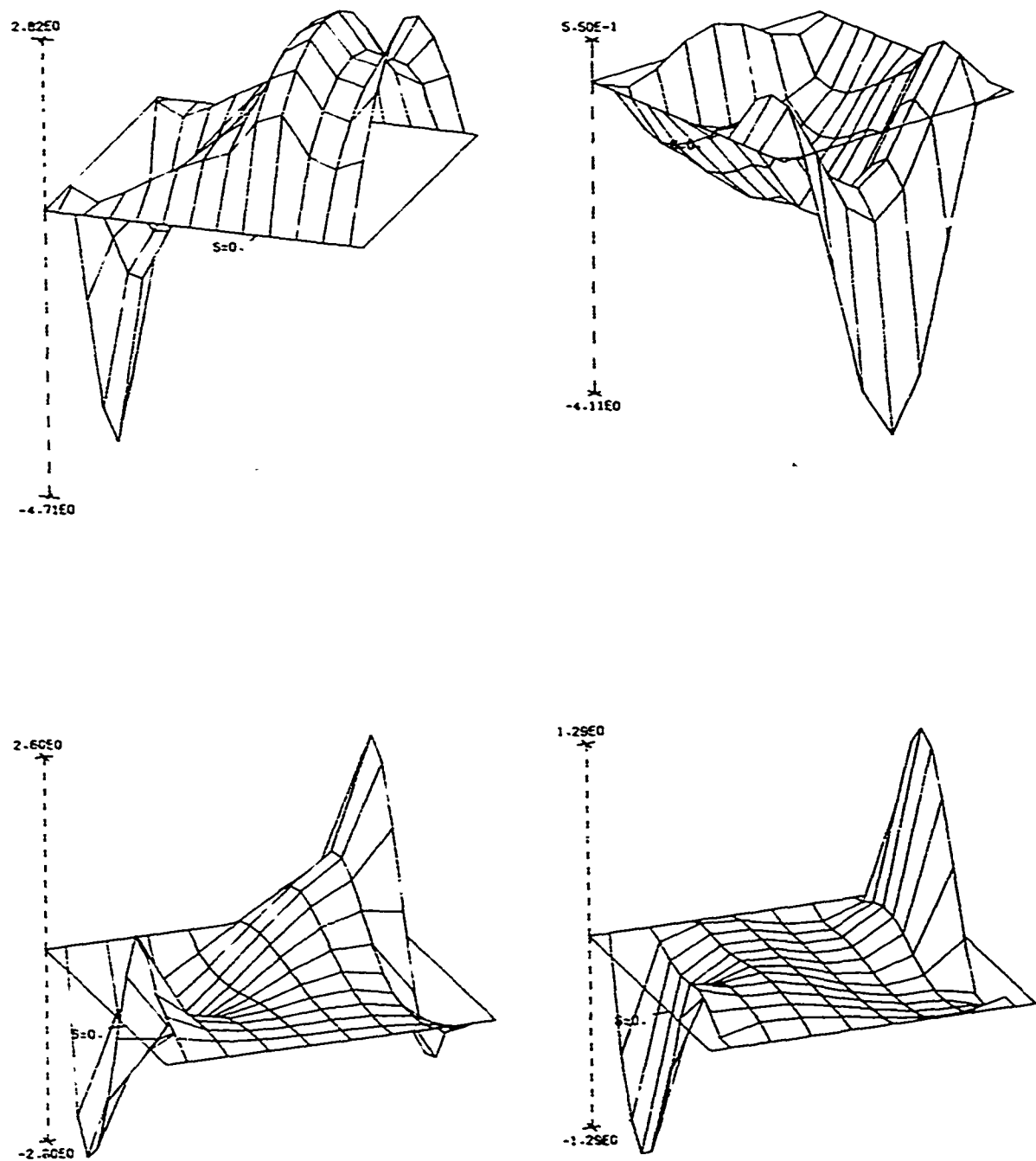


Figure 5.21. Current induced on a rectangular plate bent at $s = 0$,
 $S_x = 0.667\lambda$, $S_c = 0.333\lambda$, $Y_d = 1.0\lambda$, $\alpha = 50^\circ$, $\varepsilon = 45^\circ$,
 $\phi = 0^\circ$, $H_\theta = 1.0$, $H_\phi = 0.0$, MPR = 9, MFB = 5, N = 9;
(a) $\text{Re}(J_y)$, (b) $\text{Im}(J_y)$, (c) $\text{Re}(J_s)$, (d) $\text{Im}(J_s)$.

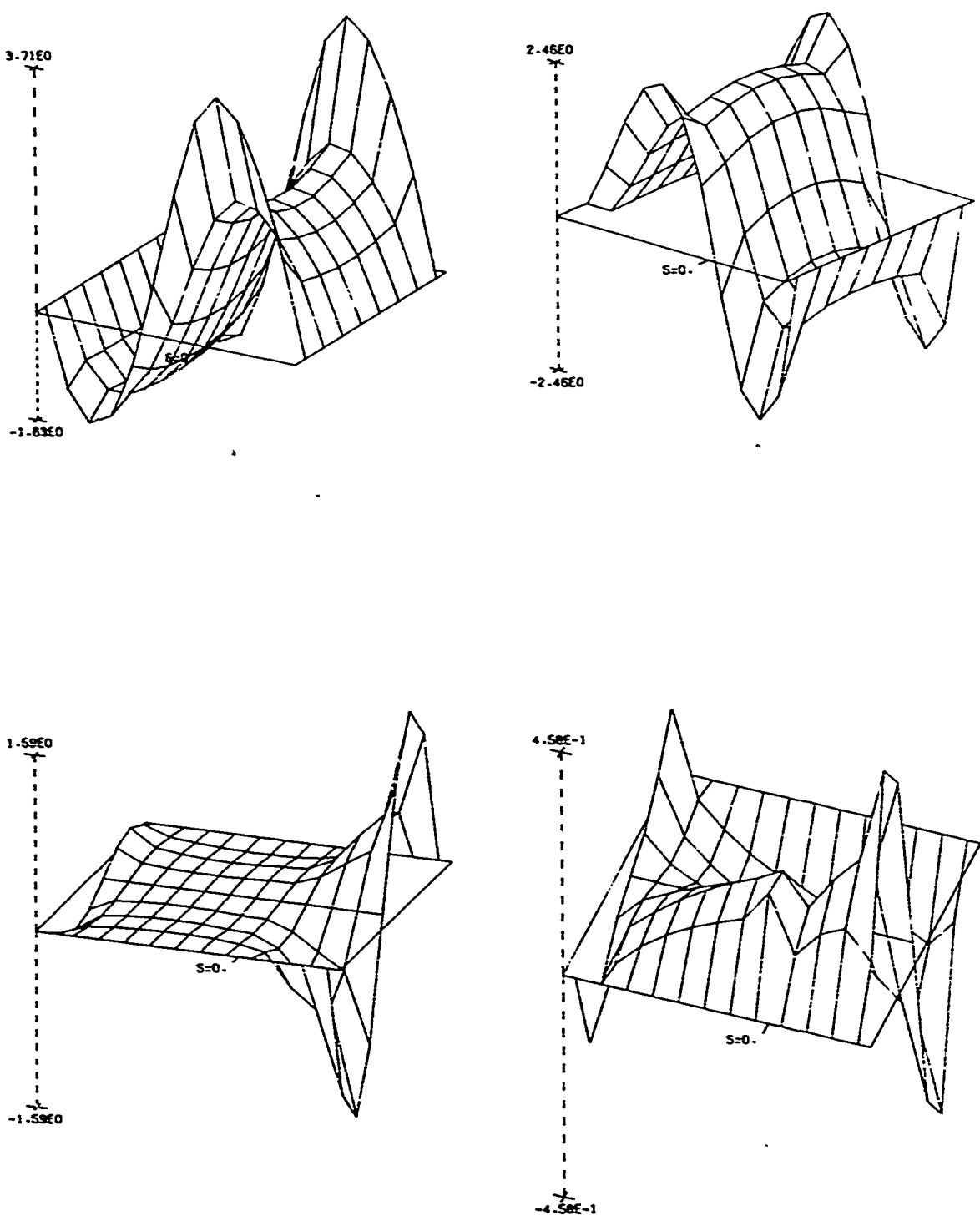


Figure 5.22. Current induced on a rectangular plate bent at $s = 0$,
 $S_x = 0.667\lambda$, $S_c = 0.333\lambda$, $Y_d = 1.0\lambda$, $\alpha = 50^\circ$, $\theta = 45^\circ$,
 $\dot{\phi} = 180^\circ$, $H_\theta = 0.0$, $H_\phi = 1.0$, MPB = 9, MFB = 5, N = 9;
(a) $\text{Re}(J_s)$, (b) $\text{Im}(J_s)$, (c) $\text{Re}(J_y)$, (d) $\text{Im}(J_y)$.

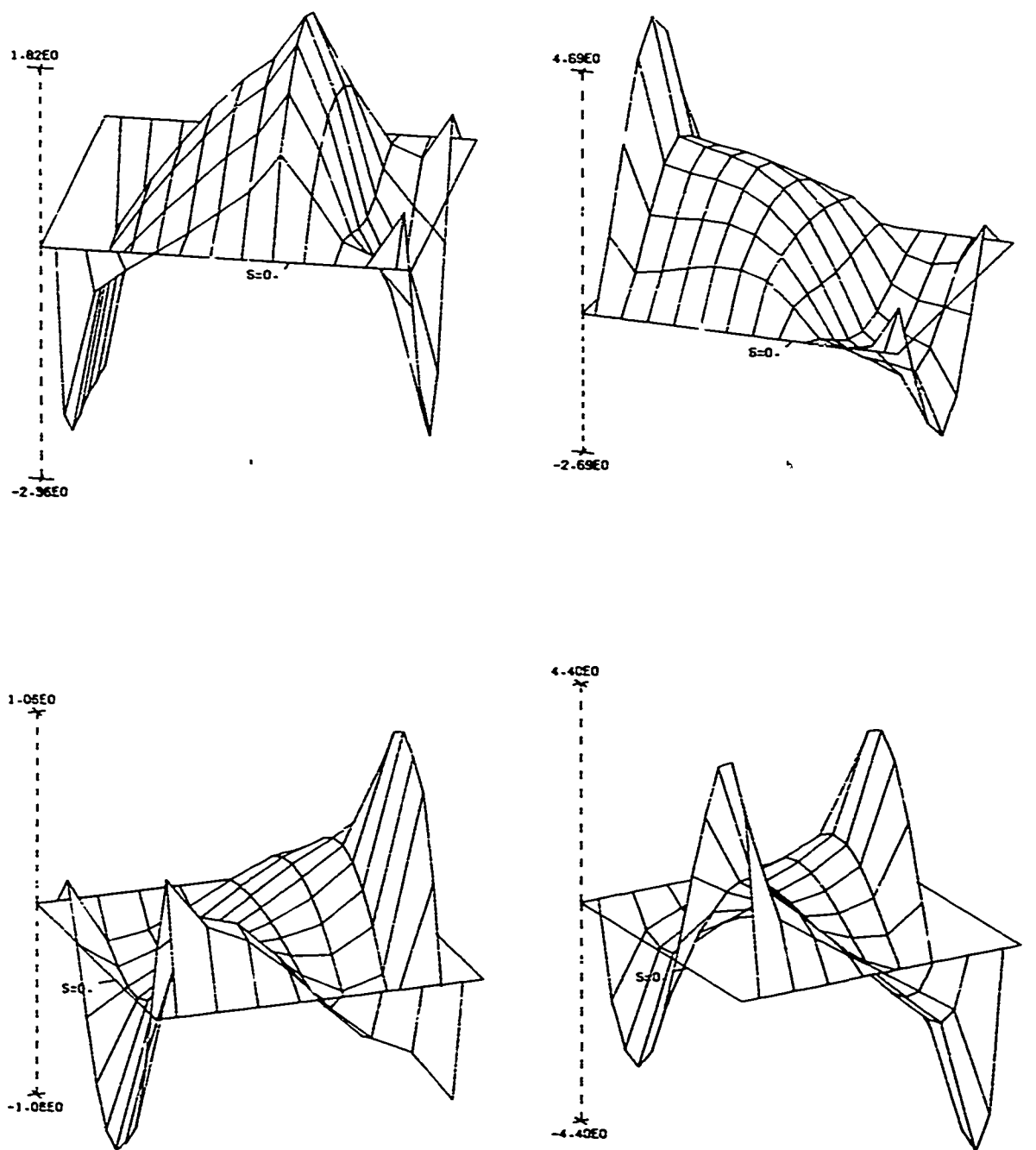


Figure 5.23. Current induced on a rectangular plate bent at $s = 0$,
 $S_x = 0.667\lambda$, $S_c = 0.333\lambda$, $Y_d = 1.0\lambda$, $\alpha = 50^\circ$, $\theta = 45^\circ$,
 $\phi = 180^\circ$, $H_\theta = -1.0$, $H_c = 0.0$, MPB = 9, NFB = 5, N = 9;
(a) $\text{Re}(J_y)$, (b) $\text{Im}(J_y)$, (c) $\text{Re}(J_s)$, (d) $\text{Im}(J_s)$.

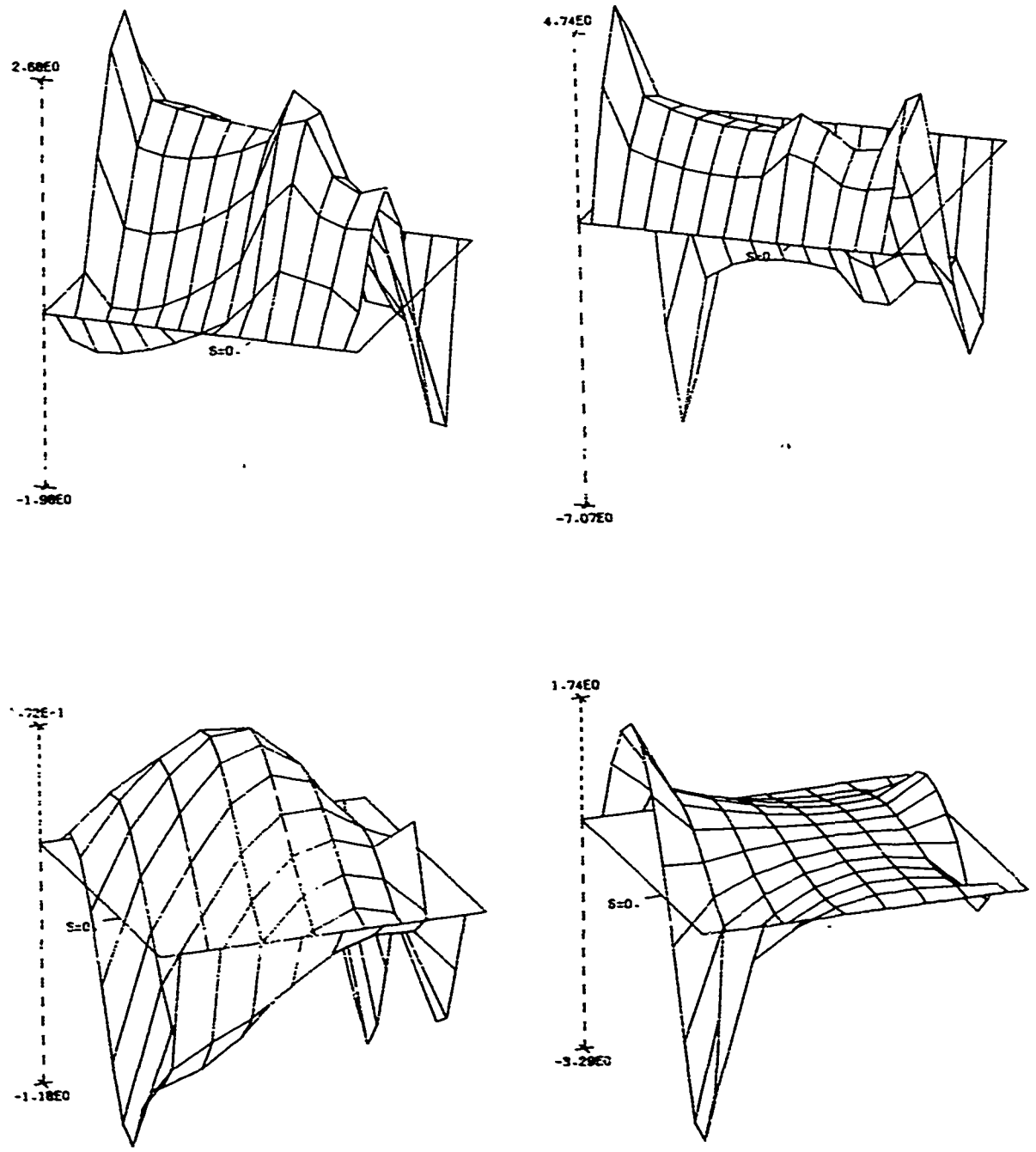


Figure 5.24. Current induced on a rectangular plate bent at $s = 0$,
 $S_x = 0.667\lambda$, $S_c = 0.333\lambda$, $Y_d = 1.0\lambda$, $\alpha = 50^\circ$, $\theta = 45^\circ$,
 $\phi = 270^\circ$, $H_\theta = 0.0$, $H_\phi = 1.0$, MPB = 9, MFB = 5, N = 9;
(a) $\text{Re}(J_y)$, (b) $\text{Im}(J_y)$, (c) $\text{Re}(J_s)$, (d) $\text{Im}(J_s)$.

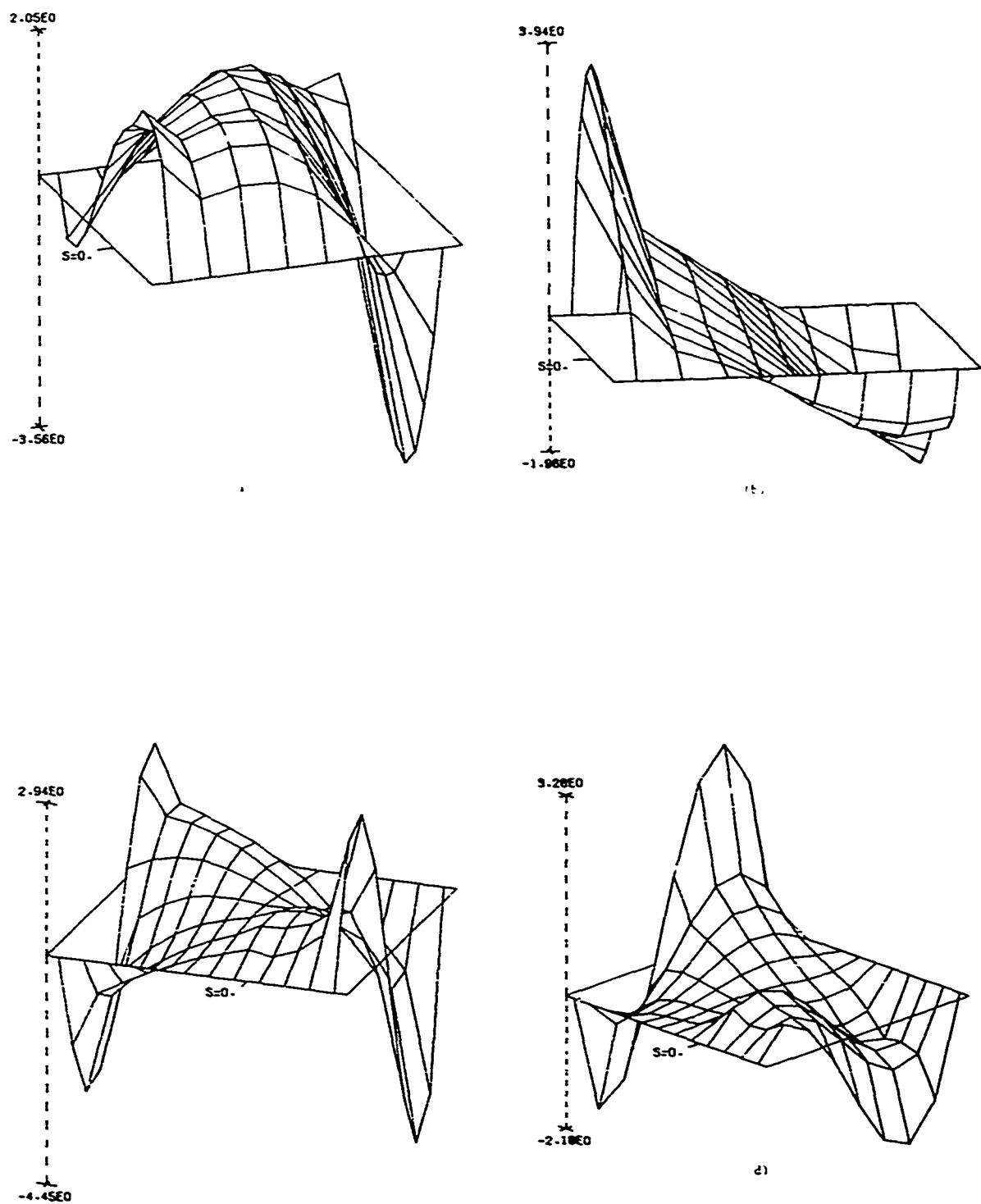


Figure 5.25. Current induced on a rectangular plate bent at $s = 0$,
 $S_x = 0.667\lambda$, $S_c = 0.333\lambda$, $Y_d = 1.0\lambda$, $\alpha = 50^\circ$, $\theta = 45^\circ$,
 $\phi = 270^\circ$, $H_\theta = 1.0$, $H_\phi = 0.0$, MPB = 9, MFB = 5, N = 9;
(a) $\text{Re}(J_s)$, (b) $\text{Im}(J_s)$, (c) $\text{Re}(J_y)$, (d) $\text{Im}(J_y)$.

the largest positive and/or negative value of the computed current on the vertical scale(s) on the left hand side of the figure. Note that the plots of current distribution stop half a subdomain from any edge where they would tend to be singular if continued to the edge and that all computed values are linked to computed currents at adjacent points by straight lines; the intersections of the lines in the figures thus are points at which the current is computed. Unfortunately, currents which flow parallel to a bend are singular on both sides of the bend, but the digital plotter merely connects currents on either side of the bend by straight lines. If this point is overlooked, some figures appear to represent currents which are completely unphysical (e.g., see Figure 11(a)).

In comparing the dominant component of the plate current (i.e., the current component parallel to the incident electric field vector) to the currents resulting from TE and TM illumination of strips of the corresponding bend angle and electrical size, it was found that the plate currents distributions along the plate center lines, i.e., along the x-, c-, and y-axes, are remarkably similar to those of the corresponding TE and TM illuminated strips. This result provided a convenient checkpoint for assessing the validity of many of the computations of plate currents.

Finally, we note that some apparent anomalies in the figures, such as the sudden downturn of the current normal to the edges in Figure 5.6(b), have been verified to be

correct by comparing the current distribution to the corresponding TE strip problem (see Figure 3.8). When such anomalies occur near corners (e.g., Figures 5.8(a) and 5.9(a)), however, then such comparisons are invalid. It is not clear in these cases, therefore, whether the result is physical, anomalous, or a result of insufficient sampling of the current since these anomalies appear only at the higher frequencies.

VI. CONCLUSIONS AND RECOMMENDATIONS

In this report, we have developed a numerical procedure for solving thin bent plate scattering problems using a method of moments solution of the electric field integral equation. The resulting technique is simple, efficient, and highly convergent. Simplicity is attained because only simple pulse representations of the current and charge are used, all derivatives are easily determined using finite difference approximations, continuity of current flowing around a bend is automatically incorporated, and no special condition on the current is required near edges or corners. Furthermore, all the integrals required involve only the free space Green's function in the integrand. Some efficiency is gained because of the simple integrals that must be performed. In addition, for flat plate structures or for flat portions of a bent plate, many of the integrals that must be computed may be reused possibly a hundred or more times in the moment matrix filling operation. Finally, some of the efficiency results from the high rate of convergence of the method since this reduces the amount of central core and/or computation time needed to obtain a converged solution. The authors expect that further savings in computation time should be possible by replacing the

present numerical integration scheme by analytically derived approximations to the integrals.

Some of the important features of the method which should be kept in mind in any possible generalizations of the method to arbitrary structures are the following:

1. Currents normal to an edge should be represented by half patches. The current is taken to be zero throughout the half patch.
2. Currents parallel to an edge should be represented by a full patch. The point inside the subdomain to which the numerically determined current is assumed to correspond should be near (or at) the patch center, away from the edge, so that the patch current coefficient represents a finite current.
3. Currents normal to a bend should be represented by patches which wrap around the bend, thus ensuring continuity of current flowing around the bend. The patch current coefficient for each patch can be associated with the value of current directly at the bend.
4. Charge subdomains adjacent to edges or bends are chosen such that their boundaries coincide with the edge or bend. The charge is computed by a finite difference approximation to the divergence of the current entering and leaving the charge subdomain.
5. The moment matrix equation is derived by forcing the component of scattered field $\bar{E}^S = -j\omega \bar{A} - \nabla \phi$ at the center of and along the direction of the assumed current in each subdomain to equal the negative of the same component of the incident field there. The directional derivative of the scalar potential there is approximated by an appropriate finite difference of the scalar potential computed at the centers of adjacent charge subdomains.

Several approaches for implementing these techniques into a general surface modeling algorithm have been considered.

However, such an approach is still in a formative stage of development at this point and is therefore not reported here. This approach is promising in that it may be possible to replace present wire grid surface modeling codes by a surface patch model code which uses the electric field integral equation.

The symmetry of the structure has not been utilized in the computer code developed from the algorithm described in this report. For the flat plate structure, there exist two symmetry planes (for the bent plate, only one symmetry plane exists) which can be used to reduce the size of the matrix that must be stored in the computer. For arbitrary angles of incidence, four separate problems then need to be solved to obtain the total solution. Since each subproblem requires the same matrix fill time as the original problem without utilizing symmetry, one merely trades reduced core requirements for increased computation time. Another technique for reducing storage limitations is to use matrix partitioning to reduce the size of matrix that must reside in core at any one time. Unfortunately, this technique also increases computation time. For larger plates or better resolution or convergence of the currents, such techniques may be necessary, however. On the other hand, one should be aware that the extra effort that must go into implementing these features, gains very little additional capability in handling larger structures. This

fact is due to the so-called "curse of dimensions" that always plagues such multi-dimensional problems.

Other extensions which can be considered are methods for treating a wire attached to a plate structure in the central portion of a plate, at an edge, or at a corner. A code is presently available for treating a disconnected wire and plate configuration (Appendix G) and it remains only to develop a technique for connecting the two structures.

There appears to be no difficulty in extending the present technique to treat a corner formed by three mutually perpendicular conducting planes. Besides the practical interest in such structures, such a geometry would be useful in numerically determining a "corner condition", since no separable coordinate system is available for analyzing such an exterior corner.

In conclusion, the data given here for current distributions on a bent plate is extremely useful since so little information is currently available as to what happens to current flowing on a bent rectangular plate. However, possibly more important for future numerical work is the ability of the staggered current subdomain scheme to resolve a number of apparently conflicting requirements on the current representation, thus leading to a simpler and more efficient numerical scheme.

APPENDIX A

BEHAVIOR OF CURRENTS NEAR BENDS AND EDGES

In this section, the behavior of currents flowing near edges and bends on conducting surfaces is summarized. The correct behavior of the currents is rigorously obtained by requiring that the total energy be bounded in any neighborhood of the edge not containing sources. We follow here the argument of Jones, which, in his words, is "plausible though lacking the rigor of ... (other) ... investigations" [4]. Jones argues that the behavior of the current near an edge or bend can be determined from an infinite cylindrical wedge of the same wedge angle as the bend or edge. Figure A.1 shows the cross-section of such an infinite cylindrical wedge. In the region $0 \leq \phi \leq 2\pi - \beta$, the fields can be decomposed into parts either TE or TM to z and can be expressed in terms of corresponding potential functions which are source free solutions of the wave equation in cylindrical coordinates [6]:

$$\psi_{TM} = \sum_{n=1}^{\infty} \int_{-\infty}^{\infty} f_n(k_z) J_{v_n}(k_z \rho) \sin v_n \phi e^{-jk_z z} dk_z \quad (A.1)$$

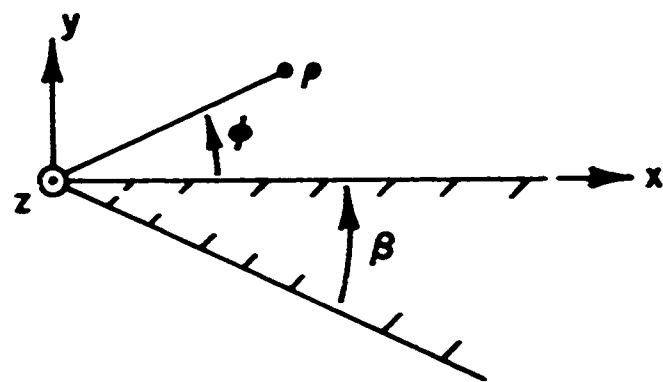


Figure A.1. Cross-section of an infinite cylindrical wedge.

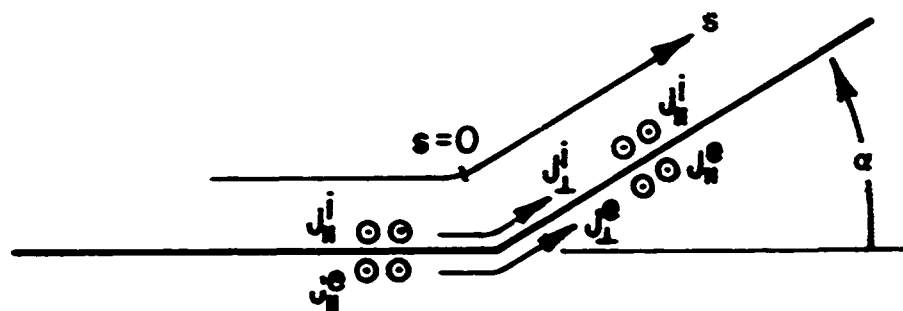


Figure A.2. Cross-section of a bent plate or strip with currents flowing parallel to and perpendicular to the bend.

$$\psi_{TE} = \sum_{n=0}^{\infty} \int_{-\infty}^{\infty} g_n(k_z) J_{v_n}(k_p \rho) \cos v_n \phi e^{-jk_z z} dk_z \quad (A.2)$$

where

$$v_n = \frac{n\pi}{2\pi - \beta} , \quad (A.3)$$

$$k_p = \sqrt{k^2 - k_z^2} . \quad (A.4)$$

The Bessel functions of the first kind are used in (A.1) and (A.2) because only they satisfy the finite energy condition in the neighborhood of $\rho = 0$ [4]. The field components are then given by

$$E_\rho = \frac{1}{j\omega\epsilon} \frac{\partial^2 \psi_{TM}}{\partial \rho \partial z} - \frac{1}{\rho} \frac{\partial \psi_{TE}}{\partial \phi} , \quad (A.5a)$$

$$E_\phi = \frac{1}{j\omega\epsilon\rho} \frac{\partial^2 \psi_{TM}}{\partial \phi \partial z} + \frac{\partial \psi_{TE}}{\partial \rho} , \quad (A.5b)$$

$$E_z = \frac{1}{j\omega\epsilon} \left(\frac{\partial^2}{\partial z^2} + k^2 \right) \psi_{TM} , \quad (A.5c)$$

$$H_\rho = \frac{1}{\rho} \frac{\partial \psi_{TM}}{\partial \phi} + \frac{1}{j\omega\mu} \frac{\partial^2 \psi_{TE}}{\partial \rho \partial z} , \quad (A.5d)$$

$$H_\phi = - \frac{\partial \psi_{TM}}{\partial \rho} + \frac{1}{j\omega\mu c} \frac{\partial^2 \psi_{TE}}{\partial \phi \partial z} , \quad (A.5e)$$

$$H_z = \frac{1}{j\omega\mu} \left(\frac{\partial^2}{\partial z^2} + k^2 \right) \psi_{TE} . \quad (A.5f)$$

The separation constant v_n and the ϕ -dependent harmonic functions in (A.1) and (A.2) are chosen such that (A.5a) and (A.5c) both vanish at $\phi = 0$ and $\phi = 2\pi - \beta$ as required.

Referring to Figure A.2, we note that a bend in a plate (strip) forms both an interior and an exterior wedge. There are two components of current, one flowing parallel and one flowing perpendicular to the bend. If one notes that the surface current density is defined as $\bar{J} = \hat{n} \times \bar{H}$ where \hat{n} is a unit outward normal to the plate (strip), and that for small values of ρ ,

$$J_v(x) \xrightarrow[x \rightarrow 0]{} \frac{1}{\Gamma(v+1)} \left(\frac{x}{2}\right)^v \quad (A.6)$$

then one easily deduces from (A.5), using the conventions of Figure A.2, the following expansions for the current near the wedge tip at $s = 0$:

$$\begin{aligned} J_{||}^e(s) &= A_1 |s|^{-\frac{|\alpha|}{\pi+|\alpha|}} + A_2 \operatorname{sgn} s |s|^{\frac{\pi-|\alpha|}{\pi+|\alpha|}} \\ &\quad + A_3 |s|^{\frac{2\pi-|\alpha|}{\pi+|\alpha|}} + A_4 \operatorname{sgn} s |s|^{\frac{3\pi-|\alpha|}{\pi+|\alpha|}} + \dots \quad (A.7a) \end{aligned}$$

$$\begin{aligned} J_{\perp}^e(s) &= B_0 + B_1 \operatorname{sgn} s |s|^{\frac{\pi}{\pi+|\alpha|}} + B_2 |s|^{\frac{2\pi}{\pi+|\alpha|}} \\ &\quad + B_3 \operatorname{sgn} s |s|^{\frac{3\pi}{\pi+|\alpha|}} + \dots \quad (A.7b) \end{aligned}$$

$$J_{||}^i(s) = C_1 |s|^{\frac{|\alpha|}{\pi - |\alpha|}} + C_2 \operatorname{sgn} s |s|^{\frac{\pi + |\alpha|}{\pi - |\alpha|}}$$

$$+ C_3 |s|^{\frac{2\pi + |\alpha|}{\pi - |\alpha|}} + C_4 \operatorname{sgn} s |s|^{\frac{3\pi + |\alpha|}{\pi - |\alpha|}} + \dots \quad (A.7c)$$

$$J_{\perp}^i(s) = D_0 + D_1 \operatorname{sgn} s |s|^{\frac{\pi}{\pi - |\alpha|}} + D_2 |s|^{\frac{2\pi}{\pi - |\alpha|}}$$

$$+ D_3 \operatorname{sgn} s |s|^{\frac{3\pi}{\pi - |\alpha|}} + \dots \quad (A.7d)$$

where

$$\operatorname{sgn} s = \begin{cases} 1, & s > 0 \\ -1, & s < 0 \end{cases} \quad (A.8)$$

The coefficients in (A.7), of course, are functions of position along the bend. One should keep in mind that in a numerical solution, the unknown current that is numerically determined in a plate or strip problem is actually the sum of the interior and exterior currents. Except for the constant terms, the exterior current typically dominates the interior current for small s because it involves lower powers of s or, in the case of $J_{||}^e$, is singular.

When $\alpha = \pi$, the tip of the wedge becomes an edge on a vanishingly thin slab of conducting material (Figure A.3).

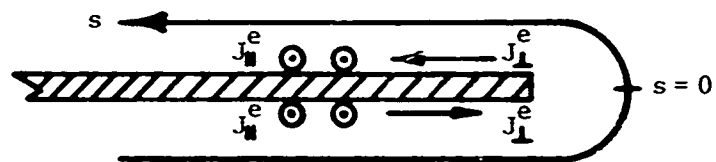
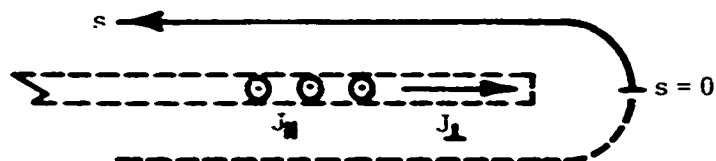


Figure A.3. Exterior currents on either side of a conducting edge.



$$\left. \begin{aligned} J_H(s) &= J_H^e(s) + J_H^e(-s) \\ J_L(s) &= J_L^e(s) - J_L^e(-s) \end{aligned} \right\}, \quad s > 0$$

Figure A.4. Net equivalent currents near a conducting edge.

In computing scattered fields from the currents flowing on a metallic scatterer, we use the equivalence principle [6] and remove the metal, leaving the currents to radiate in free space. For the vanishingly thin scatterer, the currents on either side of the edge then radiate from the same surface in space and hence may be replaced by a net equivalent current which is the appropriate vector sum of the currents on either side of the edge. Referring to Figure A.4 for the assumed current directions and using (A.7) with $\alpha = \pi$, we obtain

$$\begin{aligned} J_{\parallel}(s) &= J_{\parallel}^e(s) + J_{\parallel}^e(-s) \\ &= 2A_1 s^{-\frac{1}{2}} + 2A_3 s^{\frac{1}{2}} + \dots, \quad s > 0, \quad (A.9a) \end{aligned}$$

$$\begin{aligned} J_{\perp}(s) &= J_{\perp}^e(-s) - J_{\perp}^e(s) \\ &= -2B_1 s^{\frac{1}{2}} - 2B_3 s^{\frac{3}{2}} - \dots, \quad s > 0. \quad (A.9b) \end{aligned}$$

Thus the component of (net) current parallel to the edge has a square root singularity while the component of (net) current perpendicular to the edge vanishes as the square root of distance from the edge.

APPENDIX B

SURFACE CURRENT ON A THIN SCATTERER

Consider currents which exist on a thin (maximum thickness, Δt) scatterer as shown in Figure B.1(a). The scatterer is assumed to have two readily identifiable "sides". Quantities associated with one of the sides are denoted by a positive sign superscript, the other side by a negative sign superscript. Thus, for example, the surface currents are given by

$$\bar{J}^{\pm} = \hat{n}^{\pm} \times \bar{H}^{\pm} \quad (B.1)$$

where

$$\bar{H}^{\pm} = \bar{H}^{si} + \bar{H}^{inc} . \quad (B.2)$$

The incident magnetic field intensity, \bar{H}^{inc} , is essentially the same on both sides of the strip if Δt is small. $\bar{H}^{st\pm}$ is the scattered field on the positive (negative) side of the scatterer and \hat{n}^{\pm} is a unit vector normal to the scatterer. According to the equivalence principle [6], as far as the region exterior to the scatterer is concerned, the scatterer may be removed and the surface currents \bar{J}^{\pm} placed on the surface vacated by the scatterer (Figure B.1(b)). With the scatterer removed, these currents radiate in free space and, together with the incident fields, produce the correct fields

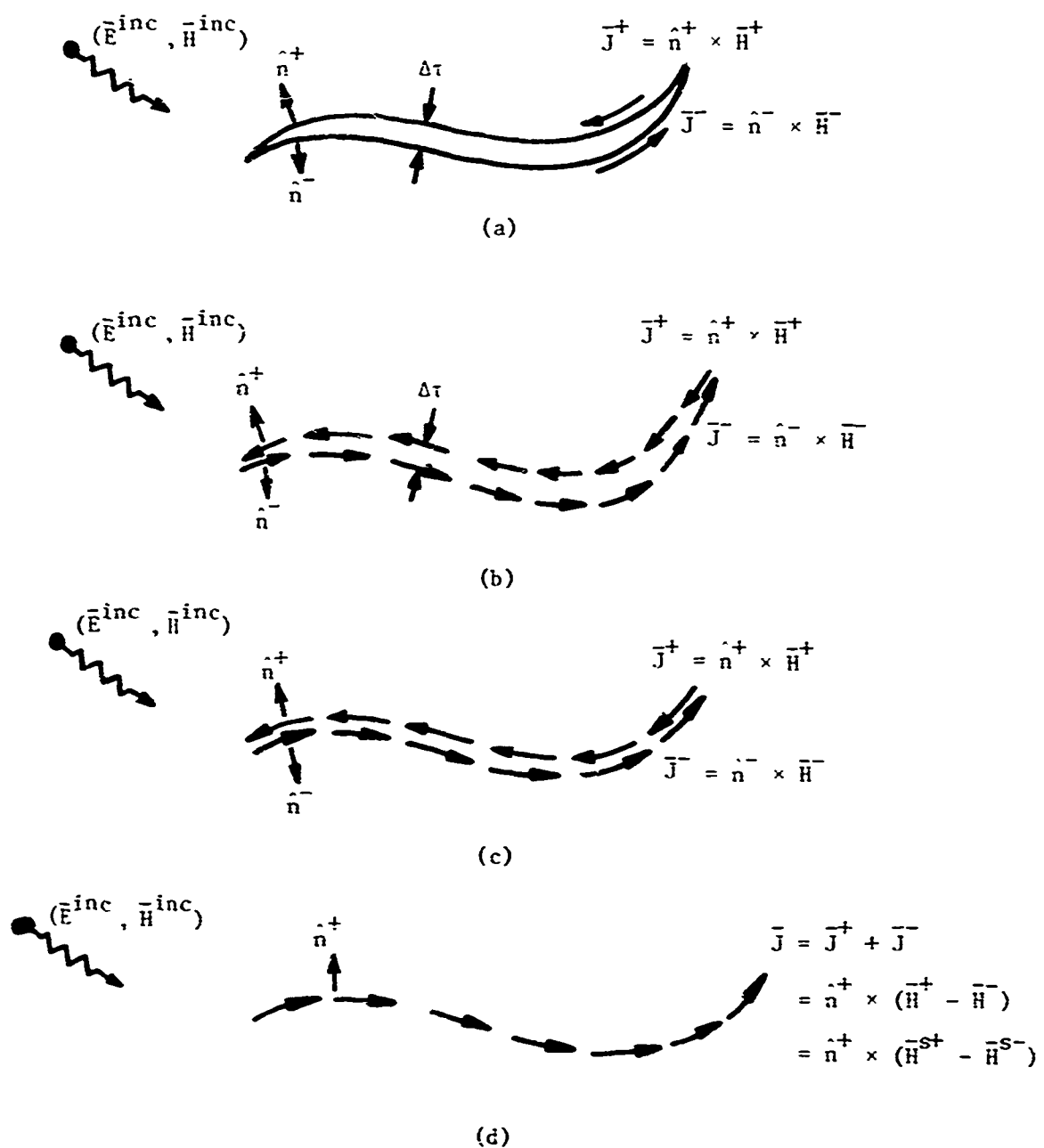


Figure B.1. Sequence of steps to arrive at a net equivalent current: (a) original scatterer of maximum thickness $\Delta\tau$, (b) scatterer replaced by equivalent currents radiating in free space, (c) equivalent currents for a vanishingly thin scatterer, and (d) replacement of currents on either side by a net equivalent current representing the scatterer.

everywhere exterior to the scatterer (and zero fields interior to the scatterer, but this is of no consequence in the following).

Now in many problems, the maximum thickness, $\Delta\tau$, of the scatterer is so small that it is convenient to assume that $\Delta\tau \approx 0$. The result is that the equivalent surface currents \bar{J}^+ and \bar{J}^- now exist on the same surface (Figure B.1(c)) and cannot be separately solved for in a numerical solution procedure. (Note that when we require the tangential electric field to vanish at a point on the scatterer, there is no longer any mechanism to distinguish which side of the scatterer we are on.) Instead, one solves for the net equivalent current (Figure B.1(d))

$$\bar{J} = \bar{J}^+ + \bar{J}^- . \quad (\text{B.3})$$

If one subsequently desires to know the current on one side or the other, he must first compute the scattered field from

$$\bar{H}^S = \frac{1}{\mu} \nabla \times \bar{A} \quad (\text{B.4})$$

where

$$\bar{A} = \frac{\mu}{4\pi} \iint_{\text{scatterer}} \bar{J}(\bar{r}') \frac{e^{-jk|\bar{r}-\bar{r}'|}}{|\bar{r}-\bar{r}'|} dS' \quad (\text{B.5})$$

and then form \bar{J}^+ or \bar{J}^- using (B.1) and (B.2). Some care must be taken in the evaluation of \bar{H}^S on the scatterer surface; one should see, for example, [7] in this regard.

The situation is somewhat simpler if the scatterer is planar, such as a flat strip or flat plate; by symmetry, one has in this case

$$\hat{n}^{\pm} \times \hat{H}^{s\pm} = \frac{\bar{J}}{2}, \quad (B.6)$$

and hence by (B.1) and (B.2),

$$\bar{J}^{\pm} = \frac{\bar{J}}{2} + \hat{n}^{\pm} \times \hat{H}^{inc}. \quad (B.7)$$

The differences in the interpretation of the equivalent currents represented by (B.1) and (B.3) should be particularly kept in mind in comparing experimentally measured currents with numerically computed currents. The latter is of the type (B.3) whereas the former is generally of the type (B.1).

APPENDIX C
INTEGRATION OF THE SELF PATCH

The integrands of the functions ψ_{xx} and ψ_{cc} are singular whenever the field point is located within the source patch region. By a simple translation of the origin these self term integrals can always be written in the following form:

$$\psi_{self} = \int_{-\frac{\Delta s}{2}}^{\frac{\Delta s}{2}} \int_{-\frac{\Delta y}{2}}^{\frac{\Delta y}{2}} \frac{e^{-jk[s^2 + y^2]^{\frac{1}{2}}}}{[s^2 + y^2]^{\frac{1}{2}}} dy ds \quad (C.1)$$

where $\Delta s = \Delta x$ or $\Delta s = \Delta c$ depending on whether (C.1) is the self term for ψ_{xx} or ψ_{cc} , respectively. Since the integrand is symmetric, ψ_{self} may also be written as

$$\psi_{self} = 4 \int_0^{\frac{\Delta s}{2}} \int_0^{\frac{\Delta y}{2}} \frac{e^{-jk[s^2 + y^2]^{\frac{1}{2}}}}{[s^2 + y^2]^{\frac{1}{2}}} dy ds . \quad (C.2)$$

Subtraction and addition of the term $[s^2 + y^2]^{-\frac{1}{2}}$ yields

$$\psi_{self} = 4 \int_0^{\frac{\Delta s}{2}} \int_0^{\frac{\Delta y}{2}} \left\{ \frac{e^{-jk[s^2 + y^2]^{\frac{1}{2}}}}{[s^2 + y^2]^{\frac{1}{2}}} - 1 + \frac{1}{[s^2 + y^2]^{\frac{1}{2}}} \right\} dy ds . \quad (C.3)$$

The first term in the integrand of (C.3) is now bounded and smooth, and can therefore be integrated accurately by numerical quadrature. The second term in the integrand is singular at $s = y = 0$. Thus we can write ψ_{self} as the sum of two integrals

$$\psi_{\text{self}} = \psi_{\text{self}}^b + \psi_{\text{self}}^s , \quad (\text{C.4})$$

where ψ_{self}^b has a bounded integrand and ψ_{self}^s has a singular integrand.

We consider now ψ_{self}^s which is given by

$$\psi_{\text{self}}^s = 4 \int_0^{\frac{\Delta s}{2}} \int_0^{\frac{\Delta y}{2}} \frac{1}{[s^2 + y^2]^{\frac{1}{2}}} dy ds . \quad (\text{C.5})$$

Integration with respect to y yields

$$\psi_{\text{self}}^s = 4 \int_0^{\frac{\Delta s}{2}} \log \left[y + \left(s^2 + y^2 \right)^{\frac{1}{2}} \right] \Big|_{y=0}^{y=\frac{\Delta y}{2}} ds , \quad (\text{C.6})$$

or

$$\begin{aligned} \psi_{\text{self}}^s &= 4 \int_0^{\frac{\Delta s}{2}} \log \left\{ \frac{\Delta y}{2} + \left[s^2 + \left(\frac{\Delta s}{2} \right)^2 \right]^{\frac{1}{2}} \right\} ds \\ &\quad - 4 \int_0^{\frac{\Delta s}{2}} (\log s) ds . \end{aligned} \quad (\text{C.7})$$

Integration with respect to s now yields

$$\begin{aligned}\psi_{\text{self}}^s &= \left[4s \log \left\{ \frac{\Delta y}{2} + \left[s^2 + \left(\frac{\Delta y}{2} \right)^2 \right]^{\frac{1}{2}} \right\} \right. \\ &\quad + 4 \left(\frac{\Delta y}{2} \right) \log \left\{ s + \left[s^2 + \left(\frac{\Delta y}{2} \right)^2 \right]^{\frac{1}{2}} \right\} \\ &\quad \left. - 4s - 4s \log s + 4s \right]_{s=0}^{s=\frac{\Delta s}{2}}, \quad (\text{C.8})\end{aligned}$$

or

$$\begin{aligned}\psi_{\text{self}}^s &= 2\Delta s \log \left\{ \frac{\Delta y}{2} + \left[\left(\frac{\Delta s}{2} \right)^2 + \left(\frac{\Delta y}{2} \right)^2 \right]^{\frac{1}{2}} \right\} \\ &\quad + 2\Delta y \log \left\{ \frac{\Delta s}{2} + \left[\left(\frac{\Delta s}{2} \right)^2 + \left(\frac{\Delta y}{2} \right)^2 \right]^{\frac{1}{2}} \right\} \\ &\quad - 2\Delta s \log \left(\frac{\Delta s}{2} \right) - 2\Delta y \log \left(\frac{\Delta y}{2} \right) \\ &= 2\Delta s \log \left\{ \left(\frac{\Delta y}{\Delta s} \right) + \left[1 + \left(\frac{\Delta y}{\Delta s} \right)^2 \right]^{\frac{1}{2}} \right\} \\ &\quad + 2\Delta y \log \left\{ \left(\frac{\Delta s}{\Delta y} \right) + \left[1 + \left(\frac{\Delta s}{\Delta y} \right)^2 \right]^{\frac{1}{2}} \right\}. \quad (\text{C.9})\end{aligned}$$

Thus, upon obtaining a numerically determined value for ψ_{self}^b , the value of ψ_{self}^s may be determined from (C.4) and (C.9).

APPENDIX D

BEHAVIOR OF SURFACE CURRENT NEAR A CORNER

In a numerical solution to a plate scattering problem, one might be properly concerned with whether or not the numerical solution represents (or is even capable of representing) the correct behavior of the current near a corner where two edges meet perpendicularly. The corner current has been examined during this study and in this section, we show that although no explicit condition on the current is imposed at the corners, the numerical solution does seem to exhibit the correct behavior at the corners. The behavior of the current at the corners or the "corner condition" may be determined from the solution of the problem of scattering by a quarter plane [8] formed by taking one quadrant of an infinite ground screen. This problem may be solved by separation of variables in spherico-conal coordinates [8] and the eigenfunctions of the resulting vector Helmholtz equation can be used to determine the corner condition in the same way as the cylindrical wavefunctions are used to determine edge conditions on a wedge (Appendix A).

Figure D.1 shows a quarter plane lying between the positive x- and y-axes in the $z = 0$ plane. Points on the quarter plane are located by coordinates (ρ, ϕ) where ρ is

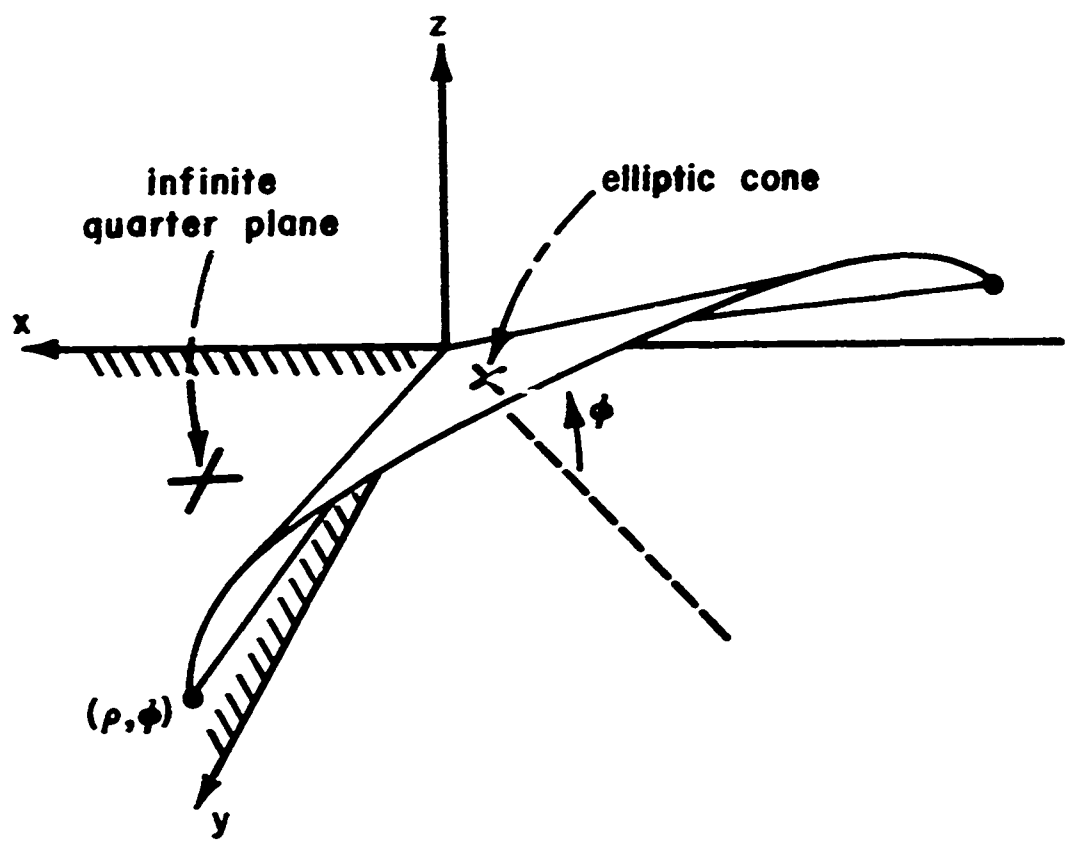


Figure D.1. Sphero-conal coordinates on an infinite quarter plane.

the distance to the origin and ϕ is the angle that an elliptic conical surface makes with the half line $y = -x$, $z = 0$, $x < 0$ (see Figure D.1). For points on the quarter plane, the relationships between the two coordinate systems are

$$x = \rho \sqrt{\frac{1}{2} - \frac{1}{2} \cos^2 \phi} - \frac{\rho \cos \phi}{2} \quad (\text{D.1a})$$

$$y = \rho \sqrt{\frac{1}{2} - \frac{1}{2} \cos^2 \phi} + \frac{\rho \cos \phi}{2} \quad (\text{D.1b})$$

$$\rho = \sqrt{x^2 + y^2} \quad (\text{D.1c})$$

$$\phi = \cos^{-1} \left(\frac{y - x}{\sqrt{x^2 + y^2}} \right) . \quad (\text{D.1d})$$

(The coordinate system of [8] has been rotated here by $\pi/4$ radians to better fit the present discussion.) According to Satterwhite and Kouyoumjian [8], the dominant behavior of the surface current near the corner is given by

$$\bar{J}(\bar{r}) = A r^{-0.186} \left[-\phi_{o2}(\phi) \hat{\phi} + 1.228 \frac{\sqrt{1 + \sin^2 \phi}}{\sin \phi} \phi'_{o2}(\phi) \hat{z} \right] \quad (\text{D.2})$$

where the functions $\phi_{o2}(\phi)$ and its derivative are periodic in ϕ and hence have Fourier series representations;

$$\phi_{o2}(\phi) \approx 0.964 \sin \phi + 0.010 \sin 3\phi + 0.001 \sin 5\phi \quad (\text{D.3a})$$

$$\phi'_{o2}(\phi) \approx 0.964 \cos \phi + 0.030 \cos 3\phi + 0.005 \cos 5\phi \quad (\text{D.3b})$$

As a check on the consistency of (D.2), we demonstrate that it satisfies the edge conditions. Because of the symmetry of the expression, it is sufficient to examine the edge along the y axis where $\phi = 0$. For small ϕ ,

$$\phi_{02} \xrightarrow[\phi \rightarrow 0]{} \phi$$

$$\phi'_{02} \xrightarrow[\phi \rightarrow 0]{} 1$$

$$x \xrightarrow[\phi \rightarrow 0]{} \frac{\rho\phi^2}{2}$$

Hence,

$$\begin{aligned} \bar{J} &\xrightarrow[\phi \rightarrow 0]{} A \rho^{-0.186} \left[-\phi \hat{\phi} + \frac{1.228}{\phi} \hat{\rho} \right] \\ &= A \rho^{-0.186} \left[-\sqrt{\frac{2x}{\rho}} \hat{\phi} + 1.228 \sqrt{\frac{\rho}{2x}} \hat{\rho} \right]. \quad (\text{D.4}) \end{aligned}$$

We see that the $\hat{\phi}$ component (normal to the edge) vanishes as the square root of x while the $\hat{\rho}$ component (parallel to the edge) varies as the reciprocal of the square root of the distance from the edge, in agreement with the edge conditions (Appendix A).

In order to compare with the numerical results obtained in Section V, we examine the y -component of \bar{J} . Noting that

$$\hat{\rho} = \frac{\hat{x}\hat{x} + \hat{y}\hat{y}}{\sqrt{\hat{x}^2 + \hat{y}^2}}, \quad (\text{D.5a})$$

$$\hat{\phi} = \frac{\hat{y}\hat{x} - \hat{x}\hat{y}}{\sqrt{\hat{x}^2 + \hat{y}^2}}, \quad (\text{D.5b})$$

one readily determines from (D.2) that

$$J_y = A (x^2 + y^2)^{-0.593} \left[x \phi_{o2}(\phi) + 1.228 \frac{\sqrt{1 + \sin^2 \phi}}{\sin \phi} y \phi'_{o2}(\phi) \right] \quad (D.6)$$

where

$$\phi = \cos^{-1} \left(\frac{y - x}{\sqrt{x^2 + y^2}} \right).$$

In order to get a feeling of the current shape in the neighborhood of the corner, (D.6) is plotted in Figure D.2. It is interesting to note in the figure, that indeed the current vanishes as the square root of distance from the x-axis and has a square root singularity on the y axis, but also that along a radial line approaching the corner, the current is singular as $\phi^{-0.186}$. Comparison with some of the low frequency plate results, say Figure 5.2(a) shows that there is at least qualitative agreement between the computed corner behavior and the theoretical corner condition.

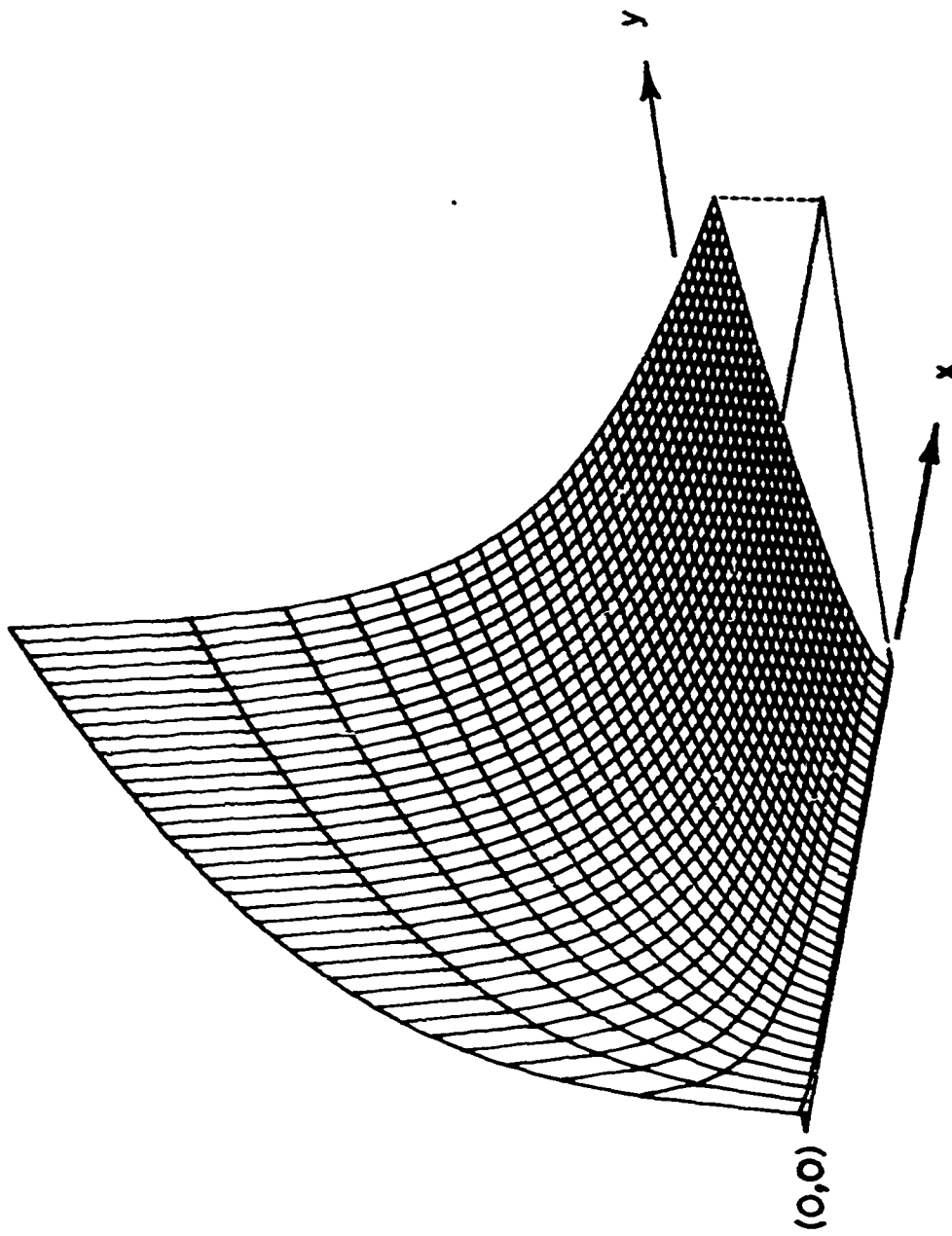


Figure D.2. Behavior of the magnitude of the y-component of current (J_y) near the corner of an infinite quarter plane located in the first quadrant of the x-y plane.

APPENDIX E
PATCH CURRENT CORRECTION FACTOR FOR CURRENTS
FLOWING PARALLEL TO AN EDGE

In [5], it was empirically found that for TM scattering by infinite strips, the coefficients of a pulse expansion of the current converge to the correct current evaluated at the center of the pulse, except for the subdomains near an edge. In the edge subdomain , convergence to the correct current is achieved only when the correct singular edge behavior of the current is explicitly incorporated in the current representation in these subdomains. However, only the edge subdomain currents appear to be affected by the use of a more accurate representation there. Hence, the edge currents can be corrected a posteriori by means of a correction factor which is the ratio of moment method impedance matrix elements for the self terms for the edge subdomains with and without the correct singular edge current representation. Later investigations have shown that these empirically observed results have some theoretical basis, as well.

It appears reasonable to expect that results analogous to those above hold for current components parallel to the edges of a rectangular plate. With this assumption, for

edge patches, convergence to the correct current would result only if the correct edge singularity is incorporated in the current representation. If no other currents are affected by this special treatment of the edge currents, then there again exists a correction factor for the currents near the edge which is determined by a ratio of the impedance matrix self-terms for a patch with and without the correct singularity in the representation. Specifically, we must compute the ratio

$$\frac{I_p}{I_s} = \frac{\int_{-\frac{\Delta x}{2}}^{\frac{\Delta x}{2}} \int_{-\frac{\Delta y}{2}}^{\frac{\Delta y}{2}} \left(\frac{\sqrt{\frac{\Delta x}{2}}}{\sqrt{x + \frac{\Delta x}{2}}} \right) \frac{e^{-jkR}}{R} dy dx}{\int_{-\frac{\Delta x}{2}}^{\frac{\Delta x}{2}} \int_{-\frac{\Delta y}{2}}^{\frac{\Delta y}{2}} \frac{e^{-jkR}}{R} dy dx} \quad (E.1)$$

where $R = \sqrt{x^2 + y^2}$. I_p represents the current value obtained from a pulse representation of the singular edge current and I_s represents the more accurate value obtained from the singular pulse representation in parentheses in (E.1). Note that in the assumed representation the current is singular at an edge located at $x = -\Delta x/2$ but that the singular pulse is of unit height at $x = 0$ where the value of the current is sought. If the frequency is low enough or the patch sizes are sufficiently small such that

$$\max kR = \frac{k}{2} \sqrt{\Delta x^2 + \Delta y^2} \ll 1 ,$$

then the exponential function can be approximated by the first term in its series expansion about $R = 0$ so that we obtain

$$\frac{I_p}{I_s} \approx \frac{\sqrt{\frac{\Delta x}{2}} \int_{-\frac{\Delta x}{2}}^{\frac{\Delta x}{2}} \int_{-\frac{\Delta y}{2}}^{\frac{\Delta y}{2}} \frac{1}{\sqrt{x + \frac{\Delta x}{2}} \sqrt{x^2 + y^2}} dy dx}{\int_{-\frac{\Delta x}{2}}^{\frac{\Delta x}{2}} \int_{-\frac{\Delta y}{2}}^{\frac{\Delta y}{2}} \frac{1}{\sqrt{x^2 + y^2}} dy dx}, \quad (E.2)$$

The denominator of (E.2) can be readily evaluated as shown in Appendix C and is given by

$$\begin{aligned} \int_{-\frac{\Delta x}{2}}^{\frac{\Delta x}{2}} \int_{-\frac{\Delta y}{2}}^{\frac{\Delta y}{2}} \frac{1}{\sqrt{x^2 + y^2}} dy dx &= 2\Delta y \ln \left[\frac{\Delta x}{\Delta y} + \sqrt{\left(\frac{\Delta x}{\Delta y}\right)^2 + 1} \right] \\ &\quad + 2\Delta x \ln \left[\frac{\Delta y}{\Delta x} + \sqrt{\left(\frac{\Delta y}{\Delta x}\right)^2 + 1} \right]. \end{aligned} \quad (E.3)$$

The integral appearing in the numerator of (E.2) is somewhat more difficult to evaluate. An exact solution can be found in terms of an infinite series, but the following form is more practical to evaluate:

$$\begin{aligned}
& \sqrt{\frac{\Delta x}{2}} \int_{-\frac{\Delta x}{2}}^{\frac{\Delta x}{2}} \int_{-\frac{\Delta y}{2}}^{\frac{\Delta y}{2}} -\frac{1}{\sqrt{x + \frac{\Delta x}{2}} \sqrt{x^2 + y^2}} dy dx = 2\sqrt{2} \Delta x \ln \left(\frac{\Delta y}{\Delta x} \right) \\
& + 4\sqrt{2} \Delta x - 2\Delta x \ln \left[\frac{\sqrt{2} - 1}{\sqrt{2} + 1} \right] + 2\sqrt{2} \Delta x \ln \left[1 + \sqrt{1 + \left(\frac{\Delta x}{\Delta y} \right)^2} \right] \\
& + \sqrt{2} \Delta x \int_{-\frac{\Delta x}{2}}^{\frac{\Delta x}{2}} \frac{\ln \left[1 + \sqrt{1 + \left(\frac{2x}{\Delta y} \right)^2} \right] - \ln \left[1 + \sqrt{1 + \left(\frac{\Delta x}{\Delta y} \right)^2} \right]}{\sqrt{x + \frac{\Delta x}{2}}} dx. \tag{E.4}
\end{aligned}$$

The only integral remaining on the right hand side of (E.4) has a non-singular integrand and can be accurately integrated numerically. It is possible to express the ratio completely in terms of the ratios of the subdomain dimensions as follows:

$$\begin{aligned}
& \sqrt{2} \ln \left(\frac{\Delta y}{\Delta x} \right) + 2\sqrt{2} - \ln \left[\frac{\sqrt{2} + 1}{\sqrt{2} - 1} \right] + \sqrt{2} \ln \left[1 + \sqrt{1 + \left(\frac{\Delta x}{\Delta y} \right)^2} \right] \\
& + \frac{1}{2} \sqrt{\frac{\Delta y}{\Delta x}} \int_{-\frac{\Delta x}{\Delta y}}^{\frac{\Delta x}{\Delta y}} \frac{\ln \left[1 + \sqrt{1 + u^2} \right] - \ln \left[1 + \sqrt{1 + \left(\frac{\Delta x}{\Delta y} \right)^2} \right]}{\sqrt{u + \frac{\Delta x}{\Delta y}}} du \\
& \frac{I_p}{I_s} \approx \frac{\frac{1}{2} \sqrt{\frac{\Delta y}{\Delta x}} \int_{-\frac{\Delta x}{\Delta y}}^{\frac{\Delta x}{\Delta y}} \frac{\ln \left[1 + \sqrt{1 + u^2} \right] - \ln \left[1 + \sqrt{1 + \left(\frac{\Delta x}{\Delta y} \right)^2} \right]}{\sqrt{u + \frac{\Delta x}{\Delta y}}} du}{\frac{\Delta y}{\Delta x} \ln \left[\frac{\Delta x}{\Delta y} + \sqrt{\left(\frac{\Delta x}{\Delta y} \right)^2 + 1} \right] + \ln \left[\frac{\Delta y}{\Delta x} + \sqrt{\left(\frac{\Delta y}{\Delta x} \right)^2 + 1} \right]} \tag{E.5}
\end{aligned}$$

Using (E.5), one can determine the ratio I_p/I_s as a function of $\Delta x/\Delta y$, as shown in Figure E.1. The result obtained in this manner is, of course, a quasi-static approximation since only the first term in the series expansion of the free

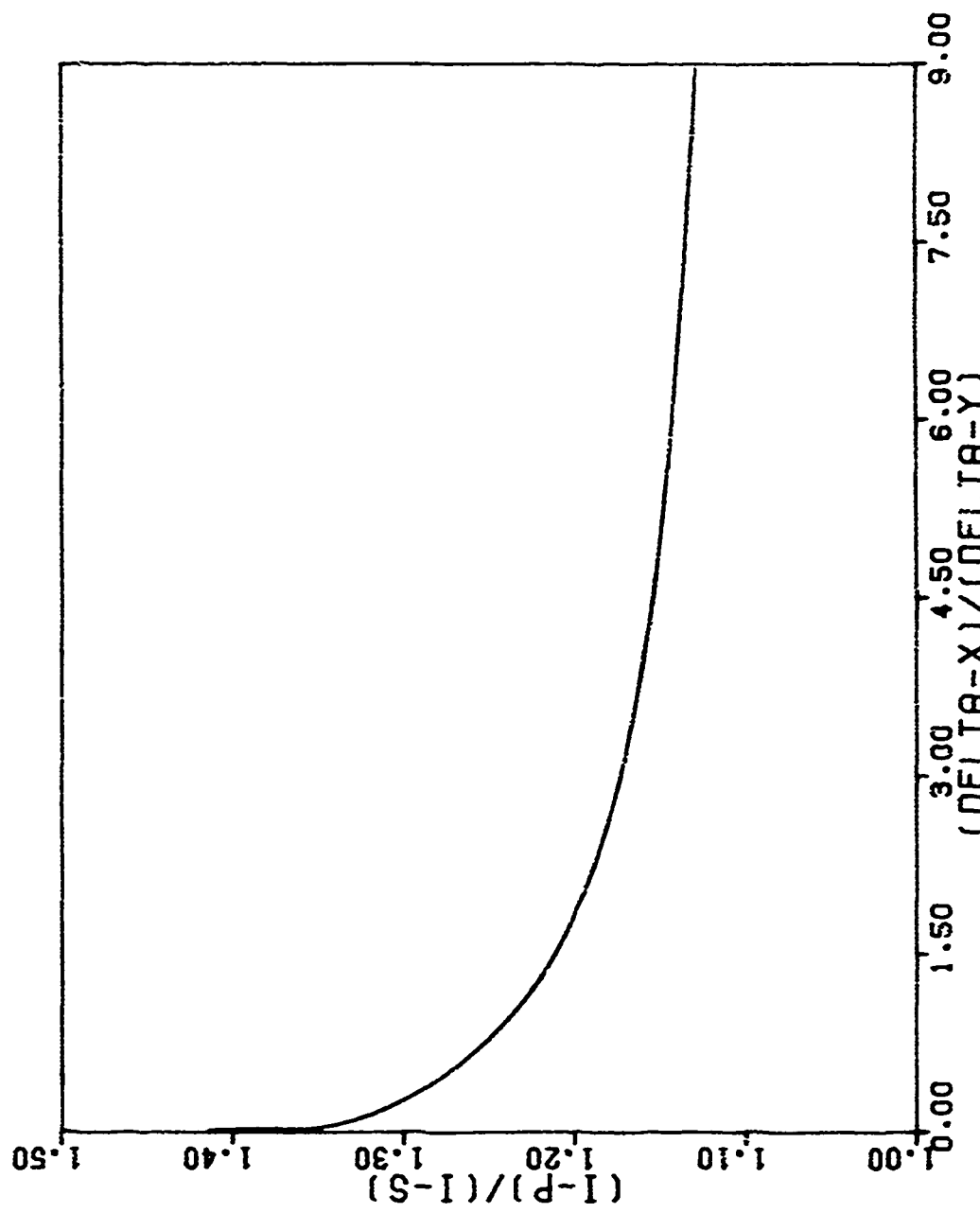


Figure E.1. Plot of the quasi-static patch current correction factor for currents flowing parallel to an edge as a function of the subdomain dimension ratio $\Delta x/\Delta y$.

space Green's function is used. No attempt has been made to verify that (E.5) does indeed predict the correct edge current nor has the approach been extended to correct currents flowing parallel to a bend. Such investigations would be worthwhile to extend the capabilities of the techniques described herein for treating plate structures.

APPENDIX F

ALTERNATE FORMS FOR THE INTEGRAL EQUATION FOR A BENT PLATE

It can be shown by means of a series of tedious but straightforward manipulations that the scalar potential defined by (4.3) and (4.8) can be written in the alternative form

$$\begin{aligned}
 \Phi(\bar{r}) = & -\frac{1}{j\omega\rho\varepsilon} \left[\frac{A_x^x \left(\bar{r} + \frac{\Delta s_x}{2} \hat{s} \right) - A_x^x \left(\bar{r} - \frac{\Delta s_x}{2} \hat{s} \right)}{\Delta s_x} \right. \\
 & + \frac{A_c^c \left(\bar{r} + \frac{\Delta s_c}{2} \hat{c} \right) - A_c^c \left(\bar{r} - \frac{\Delta s_c}{2} \hat{c} \right)}{\Delta s_c} \\
 & \left. + \frac{A_v^v \left(\bar{r} + \frac{\Delta v}{2} \hat{y} \right) - A_v^v \left(\bar{r} - \frac{\Delta v}{2} \hat{y} \right)}{\Delta v} \right] \\
 & + \phi^x(\bar{r}) + \phi^c(\bar{r}) \tag{F.1}
 \end{aligned}$$

The quantities A_x^x and A_c^c arise from partitioning the vector potential as follows:

$$A_x = A_x^x + A_x^c \tag{F.2a}$$

$$A_c = A_c^x + A_c^c \tag{F.2b}$$

where the superscripts denote partial potentials arising

from currents which flow only in the direction indicated by the superscript. Thus, the vector potential A_p^x ($p = x$ or c) is defined by the first two lines of (4.14b) while A_p^c is associated with the last two lines of (4.14b). The terms $\phi^x(\bar{r})$ and $\phi^c(\bar{r})$ are scalar potentials produced by currents which flow around the bend in the plate:

$$\phi^x(\bar{r}) = \frac{j}{4\pi\omega\epsilon} \sum_{LJ=1}^{N-1} \frac{\int_{y_{LJ}^s - \frac{\Delta y}{2}}^{y_{LJ}^s + \frac{\Delta y}{2}} \int_{-\frac{\Delta s_x}{2}}^{\frac{\Delta s_x}{2}} \frac{e^{-jk|\bar{r}-\bar{r}'|}}{|\bar{r}-\bar{r}'|} dx' dy'}{\int_{y_{LJ}^s - \frac{\Delta y}{2}}^{y_{LJ}^s + \frac{\Delta y}{2}} \frac{\Delta s_x}{2} ds_x} J_{MPB-1,LJ}^s \quad (F.3a)$$

$$\phi^c(\bar{r}) = \frac{-j}{4\pi\omega\epsilon} \sum_{LJ=1}^{N-1} \frac{\int_{y_{LJ}^s - \frac{\Delta y}{2}}^{y_{LJ}^s + \frac{\Delta y}{2}} \int_{-\frac{\Delta s_c}{2}}^{\frac{\Delta s_c}{2}} \frac{e^{-jk|\bar{r}-\bar{r}'|}}{|\bar{r}-\bar{r}'|} dx' dy'}{\int_{y_{LJ}^s - \frac{\Delta y}{2}}^{y_{LJ}^s + \frac{\Delta y}{2}} \frac{\Delta s_c}{2} ds_c} J_{MPB-1,LJ}^s \quad (F.3b)$$

These terms are related to the consequences of the numerical approach on the "electrical completeness" that is always implicit in the use of the Lorentz gauge condition to replace scalar potential by vector potential quantities [9]. Note that the moments of the effective charges from which the potentials (F.3a) and (F.3b) arise are equal in magnitude but of opposite sign and hence cancel as the bend angle, α , and the difference in subdomain lengths, $\Delta s_x - \Delta s_c$, approach zero. The contribution of these terms also vanishes when Δs_x and Δs_c both approach zero. Hence (F.1) is a numerical approximation to the Lorentz gauge condition

$$\phi(\bar{r}) = - \frac{1}{j\omega\mu\epsilon} \left[\frac{\partial A_x^x}{\partial s_x} + \frac{\partial A_c^c}{\partial s_c} + \frac{\partial A_v^v}{\partial y} \right] = - \frac{1}{j\omega\mu\epsilon} \nabla \cdot \bar{A} \quad (F.4)$$

If one writes (F.1) as

$$\phi(\bar{r}) = - \frac{1}{j\omega\mu\epsilon} \left[\frac{\Delta A_x^x(\bar{r})}{\Delta s_x} + \frac{\Delta A_c^c(\bar{r})}{\Delta s_c} + \frac{\Delta A_v^v(\bar{r})}{\Delta y} \right] + \phi^x(\bar{r}) + \phi^c(\bar{r}) \quad (F.5)$$

where the central finite difference operators in (F.5) are defined by comparing to (F.1), then Equations (4.12) can be written in the alternative form

$$\begin{aligned} -E_x^{inc}(s_{IS}^s, y_{JS}^s) \Delta s_x &= \frac{\Delta s_x}{j\omega\mu\epsilon} \left[k^2 A_x(s_{IS}^s, s_{JS}^s) \right. \\ &\quad + \frac{\Delta^2}{\Delta s_x^2} A_x^x(s_{IS}^s, s_{JS}^s) + \frac{\Delta^2}{\Delta s_x \Delta s_c} A_c^c(s_{IS}^s, s_{JS}^s) \\ &\quad \left. + \frac{\Delta^2}{\Delta s_x \Delta y} A_y(s_{IS}^s, s_{JS}^s) \right] \\ - \Delta s_x \frac{\Delta}{\Delta s_x} &\left[\phi^x(s_{IS}^s, s_{JS}^s) + \phi^c(s_{IS}^s, s_{JS}^s) \right], \quad (F.6a) \end{aligned}$$

IS=1 to MPB-2

JS=1 to MSUNKY ,

$$\begin{aligned}
-E_c^{inc}(s_{IS}^s, y_{JS}^s) \Delta s_c &= \frac{\Delta s_c}{j\omega\mu\varepsilon} \left[k^2 A_c(s_{IS}^s, y_{JS}^s) \right. \\
&+ \frac{\Delta^2}{\Delta s_c^2} A_c^c(s_{IS}^s, y_{JS}^s) + \frac{\Delta^2}{\Delta s_c \Delta s_x} A_x^x(s_{IS}^s, y_{JS}^s) \\
&\left. + \frac{\Delta^2}{\Delta y^2} A_y(s_{IS}^s, y_{JS}^s) \right] \\
&- \Delta s_c \frac{\Delta}{\Delta s_c} \left[\phi^x(s_{IS}^s, y_{JS}^s) + \phi^c(s_{IS}^s, y_{JS}^s) \right], \quad (F.6b) \\
&\text{IS=MPB to MSUNKS} \\
&\text{JS=1 to MSUNKY ,}
\end{aligned}$$

$$\begin{aligned}
-E_y^{inc}(s_{IY}^y, y_{JY}^y) \Delta y &= \frac{\Delta y}{j\omega\mu\varepsilon} \left[k^2 A_y(s_{IY}^y, y_{JY}^y) \right. \\
&+ \frac{\Delta^2}{\Delta y^2} A_y^y(s_{IY}^y, y_{JY}^y) + \frac{\Delta^2}{\Delta y \Delta s_x} A_x^x(s_{IY}^y, y_{JY}^y) \\
&\left. + \frac{\Delta^2}{\Delta y \Delta s_c} A_c^c(s_{IY}^y, y_{JY}^y) \right] \\
&- \Delta y \frac{\Delta}{\Delta y} \left[\phi^x(s_{IY}^y, y_{JY}^y) + \phi^c(s_{IY}^y, y_{JY}^y) \right], \quad (F.6c) \\
&\text{IY=1 , NYUNKS} \\
&\text{JY=1 , NYUNKY ,}
\end{aligned}$$

$$\begin{aligned}
& - \frac{1}{2} \left[E_x^{inc}(s_{IS}^s, y_{JS}^s) \Delta s_x + E_c^{inc}(s_{IS}^s, y_{JS}^s) \Delta s_c \right] \\
& = \frac{1}{2j\omega\mu\varepsilon} \left\{ k^2 A_x(s_{IS}^s, y_{JS}^s) \Delta s_x + k^2 A_c(s_{IS}^s, y_{JS}^s) \Delta s_c \right. \\
& \quad + \left(\Delta s_x \frac{\Delta}{\Delta s_x} + \Delta s_c \frac{\Delta}{\Delta s_c} \right) \left[\frac{\Delta}{\Delta s_x} A_x^s(s_{IS}^s, y_{JS}^s) \right. \\
& \quad \left. \left. + \frac{\Delta}{\Delta s_c} A_c^s(s_{IS}^s, y_{JS}^s) + \frac{\Delta}{\Delta y} A_y^s(s_{IS}^s, y_{JS}^s) \right] \right\} \\
& - \left(\Delta s_x \frac{\Delta}{\Delta s_x} + \Delta s_c \frac{\Delta}{\Delta s_c} \right) \left[\phi_x^s(s_{IS}^s, y_{JS}^s) + \phi_c^s(s_{IS}^s, y_{JS}^s) \right], \tag{F.6d}
\end{aligned}$$

IS=MPB-1

JS=1 , MSUNKY .

We emphasize that Equations (F.6) are numerically equivalent to (4.12). This present form has the advantage of illustrating explicitly the fact that the scalar potential integrals are nothing more than vector potential integrals evaluated at different observation points. On the other hand, (4.12) is a more compact form and does not require a special treatment of the edge currents as does (F.6).

APPENDIX G

DETERMINATION OF CURRENTS EXCITED ON A WIRE/PLATE STRUCTURE

In this appendix, we investigate the problem of determining the currents excited on a structure which comprises a straight wire and a bent plate and which is illuminated by a known incident field (\bar{E}^i , \bar{H}^i). Coupled integro-differential equations are formulated for this problem in terms of the unknown surface current \bar{J}_s on the plate and the unknown axial current I on the wire. These equations are solved numerically by the methods developed in this report and sample results are presented.

The plate and wire are depicted in Figure G.1, which, in addition, serves to define various quantities pertinent to the present problem. The wire is thin relative to its length and to the wavelength of the electromagnetic field, and the plate is vanishingly thin. Both the wire and the plate are assumed to be perfect conductors, and the usual approximations of thin-wire analyses are employed here.

A Cartesian coordinate system is located on the plate as shown in the figure where one sees that the bend is coincident with the x axis. One surface of the bent plate in Figure G.1 is labeled S_I and is in the x-y plane while that labeled S_{II} is declined by an angle α from the y-axis.

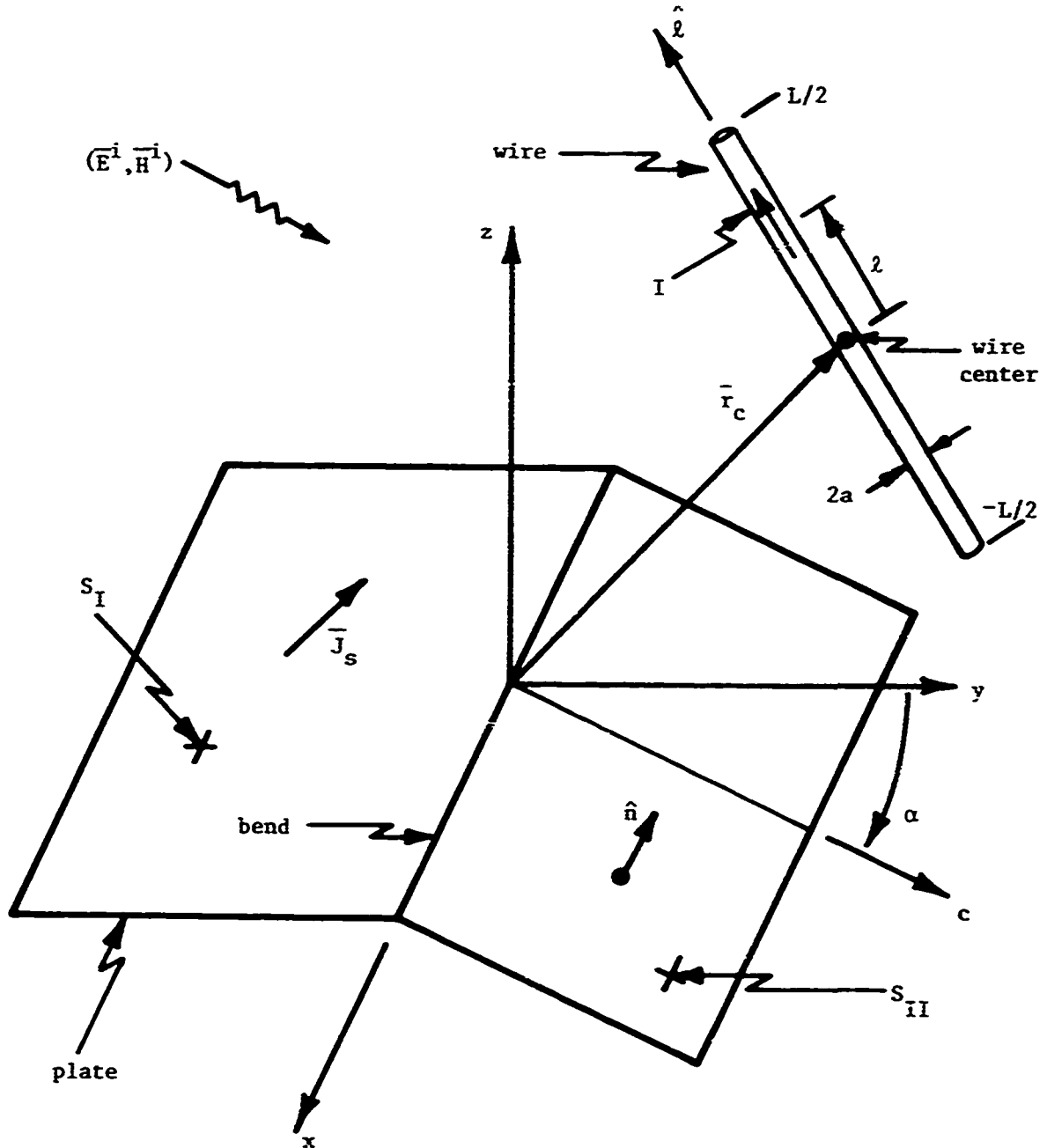


Figure G.1. Geometry of a wire near a bent plate.

Points (x, y) on S_I are located in the usual way,
 $\bar{r} = x\hat{x} + y\hat{y}$, while those on S_{II} are located by

$$\bar{r} = x\hat{x} + c\hat{c} \quad (G.1)$$

where c is measured along the c axis in the direction of
the unit vector \hat{c} defined by

$$\hat{c} = \hat{y} \cos\alpha - \hat{z} \sin\alpha . \quad (G.2)$$

The unit vector normal to the surface S_I is simply $\hat{n} = \hat{z}$
while that normal to the surface S_{II} is

$$\hat{n} = \hat{x} \times \hat{c} . \quad (G.3)$$

The geometry of the thin, cylindrical wire is specified
by its radius a and by the location of its lower and upper
endpoints, (x_a, y_a, z_a) and (x_b, y_b, z_b) , respectively.
From knowledge of these endpoints, one can determine other
needed geometric quantities:

LENGTH: L

$$L = \left[(x_b - x_a)^2 + (y_b - y_a)^2 + (z_b - z_a)^2 \right]^{\frac{1}{2}} \quad (G.4a)$$

UNIT VECTOR: $\hat{\ell}$

$$\hat{\ell} = \frac{1}{L} \left[(x_b - x_a)\hat{x} + (y_b - y_a)\hat{y} + (z_b - z_a)\hat{z} \right] \quad (G.4b)$$

WIRE CENTER: \bar{r}_c

$$\bar{r}_c = \frac{1}{2} \left[(x_a + x_b) \hat{x} + (y_a + y_b) \hat{y} + (z_a + z_b) \hat{z} \right] \quad (G.4c)$$

Formulation

The total electric field tangential to the surfaces of the perfectly conducting plate and wire must be zero. This can be expressed as

$$\hat{n} \times \bar{E} = 0 \quad \text{on } S_I \text{ and } S_{II} \quad (G.5a)$$

and

$$\hat{i} \cdot \bar{E} = 0 \quad \text{on wire} \quad (G.5b)$$

or as

$$\hat{n} \times \bar{E}^s = -\hat{n} \times \bar{E}^i \quad \text{on } S_I \text{ and } S_{II} \quad (G.6a)$$

and

$$\hat{i} \cdot \bar{E}^s = -\hat{i} \cdot \bar{E}^i \quad \text{on wire} \quad (G.6b)$$

where \bar{E} is the total electric field, \bar{E}^i is the specified incident field, and \bar{E}^s is the scattered electric field produced by the currents and charges induced on the plate and wire. The total scattered electric field can be written

$$\bar{E}^s = -j\omega \bar{A} - \nabla \phi \quad (G.7)$$

where \bar{A} is the magnetic vector potential and ϕ is the electric scalar potential. \bar{A} is due to both the wire

current and the plate current and ϕ is due to both wire and plate charges.

On the plate, enforcement of (G.6a) leads to

$$\hat{n} \times (j\omega \bar{A} + \nabla \phi) = \hat{n} \times \bar{E}^i \quad \text{on } S_I \text{ and } S_{II} \quad (\text{G.8})$$

where

$$\bar{A} \Big|_{\substack{\text{on} \\ \text{plate}}} = \frac{u}{4\pi} \iint_{S_I + S_{II}} \bar{J}_s(\bar{r}') \frac{e^{-jk|\bar{r}-\bar{r}'|}}{|\bar{r}-\bar{r}'|} dS'$$

$$+ \frac{\mu}{4\pi} \hat{\ell} \int_{\ell'=-L/2}^{L/2} I(\ell') \frac{e^{-jk|\bar{r}-\bar{r}_c-\ell'\hat{\ell}|}}{|\bar{r}-\bar{r}_c-\ell'\hat{\ell}|} d\ell', \quad \bar{r} \in S_I, S_{II} \quad (\text{G.9a})$$

and where

$$\phi \Big|_{\substack{\text{on} \\ \text{plate}}} = j \frac{\eta}{4\pi k} \iint_{S_I + S_{II}} \nabla' \cdot \bar{J}_s(\bar{r}') \frac{e^{-jk|\bar{r}-\bar{r}'|}}{|\bar{r}-\bar{r}'|} dS'$$

$$+ j \frac{\eta}{4\pi k} \int_{\ell'=-L/2}^{L/2} \frac{d}{d\ell'} I(\ell') \frac{e^{-jk|\bar{r}-\bar{r}_c-\ell'\hat{\ell}|}}{|\bar{r}-\bar{r}_c-\ell'\hat{\ell}|} d\ell', \quad \bar{r} \in S_I, S_{II} \quad (\text{G.9b})$$

Attention is called to the fact that the plate is bent and, thus, that Equation (G.8) must be enforced on both planar surfaces with appropriate interpretation of the unit normal vector \hat{n} discussed above. In addition, the integrals over the plate in Equations (G.9) must be taken over sur-

faces S_I and S_{II} individually with the following definition of the surface current density:

$$\bar{J}_s = \begin{cases} J_x(x,y)\hat{x} + J_y(x,y)\hat{y} & \text{on } S_I \\ J_x(x,c)\hat{x} + J_c(x,c)\hat{c} & \text{on } S_{II} \end{cases} \quad (G.10)$$

The notation in Equation (G.10) serves to emphasize the dependence of the surface current density on surface S_{II} upon the coordinates of this surface.

Equation (G.6b), the boundary condition on the wire, can be expressed as

$$(j\omega\bar{A} + \nabla\phi) \cdot \hat{\ell} = j\omega\bar{A} \cdot \hat{\ell} + \frac{\partial}{\partial \ell} \phi = \bar{E}^i \cdot \hat{\ell} \quad \text{on wire} \quad (G.11)$$

in which

$$\begin{aligned} \bar{A}(\ell) &= \frac{\mu}{4\pi} \hat{\ell} \int_{\ell'=-L/2}^{L/2} I(\ell') K(\ell-\ell') d\ell' \\ &+ \frac{\mu}{4\pi} \iint_{S_I+S_{II}} \bar{J}_s(\bar{r}') \frac{e^{-jk|\bar{r}_c + \ell\hat{\ell} - \bar{r}'|}}{|\bar{r}_c + \ell\hat{\ell} - \bar{r}'|} dS', \quad \ell \in (-L/2, L/2) \end{aligned} \quad (G.12)$$

and

$$\Phi(\ell) = j \frac{n}{4\pi k} \int_{\ell'=-L/2}^{L/2} \frac{d}{d\ell'} I(\ell') K(\ell - \ell') d\ell'$$

$$+ j \frac{n}{4\pi k} \iint_{S_I + S_{II}} \bar{v}' \cdot \bar{J}_s(\bar{r}') \frac{e^{-jk|\bar{r}_c + \hat{\ell}\hat{\ell} - \bar{r}'|}}{|\bar{r}_c + \hat{\ell}\hat{\ell} - \bar{r}'|} dS' , \quad \ell \in (-L/2, L/2) \quad (G.12b)$$

with the exact kernel $K(\ell - \ell')$ above given by

$$K(\zeta) = \frac{1}{2\pi} \int_{\phi'=-\pi}^{\pi} \frac{e^{-jk\left[\zeta^2 + 4a^2 \sin^2 \frac{\phi'}{2}\right]^{1/2}}}{\left[\zeta^2 + 4a^2 \sin^2 \frac{\phi'}{2}\right]^{1/2}} d\phi' \quad (G.13)$$

(G.8) and (G.11) constitute a set of coupled, vector integro-differential equations, which, in principle, can be solved for the unknown current density \bar{J}_s on the plate and axial current I on the wire.

Sample Results

By a simple extension of the numerical techniques developed elsewhere in this report for solving the bent-plate equations, one can solve (G.8) and (G.11) and thereby determine \bar{J}_s on the plate and I on the wire. In the following paragraphs are presented data illustrative of the behavior of current on the wire and plate in selected configurations.

In Figures G.2 and G.3 are shown, respectively, the plate current on a $0.5\lambda \times 0.5\lambda$ square plate and a wire

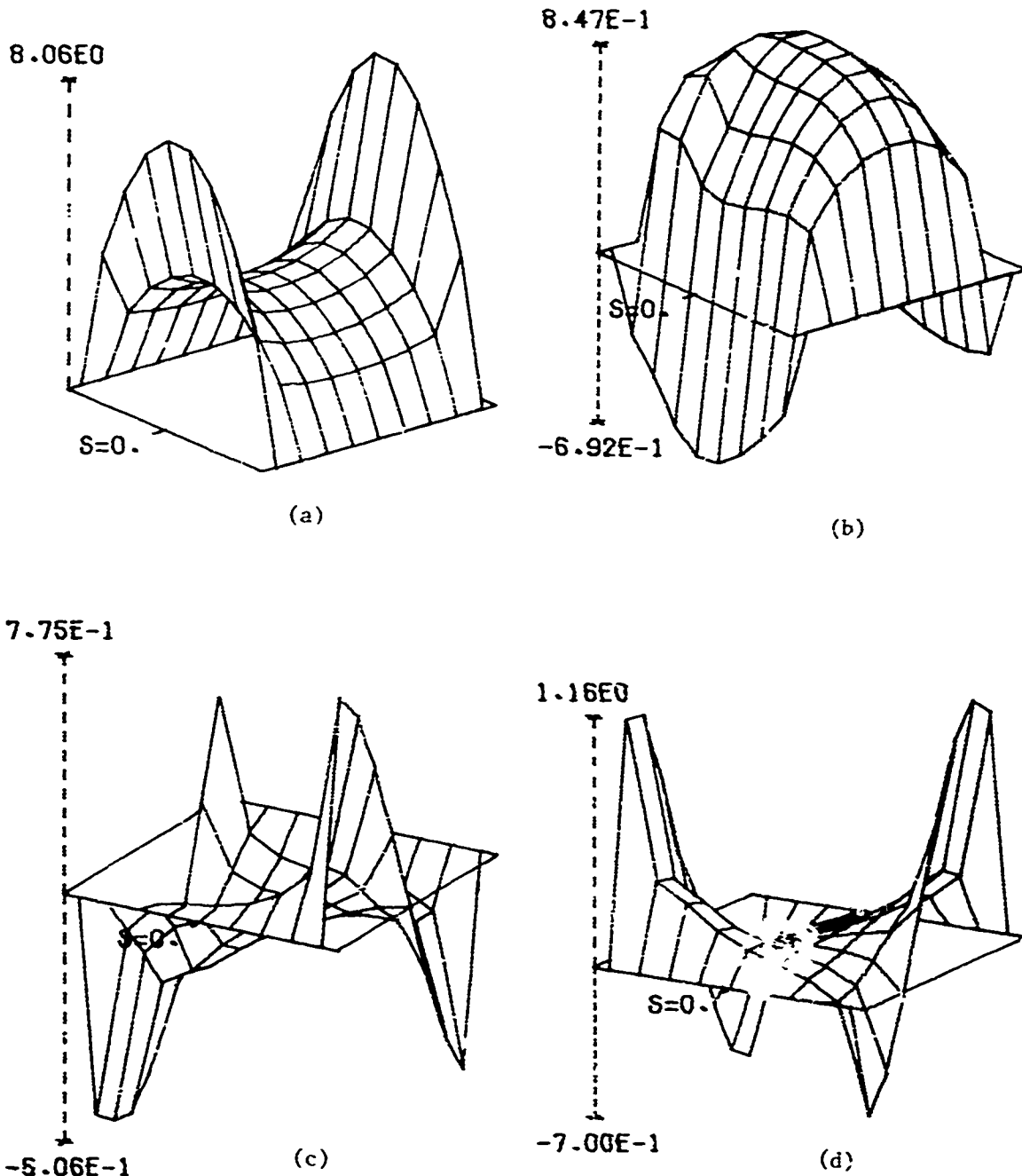


Figure G.2. Current induced on a square plate near a wire, $S_x = 0.5\lambda$,
 $y_d = 0.5\lambda$, $L = 1.0\lambda$, $a = .001\lambda$, $\bar{r}_c = (-0.125\lambda, -0.125\lambda, 0.525\lambda)$, $\hat{i} = (0.0, 0.0, 1.0)$, $\theta = 0^\circ$, $\phi = 0^\circ$, $H_g = 0.9$,
 $H_\phi = -1.0$; (a) $\text{Re}(J_s)$, (b) $\text{Im}(J_s)$, (c) $\text{Re}(J_y)$, (d) $\text{Im}(J_y)$.
The wire current is shown in Figure G.3.

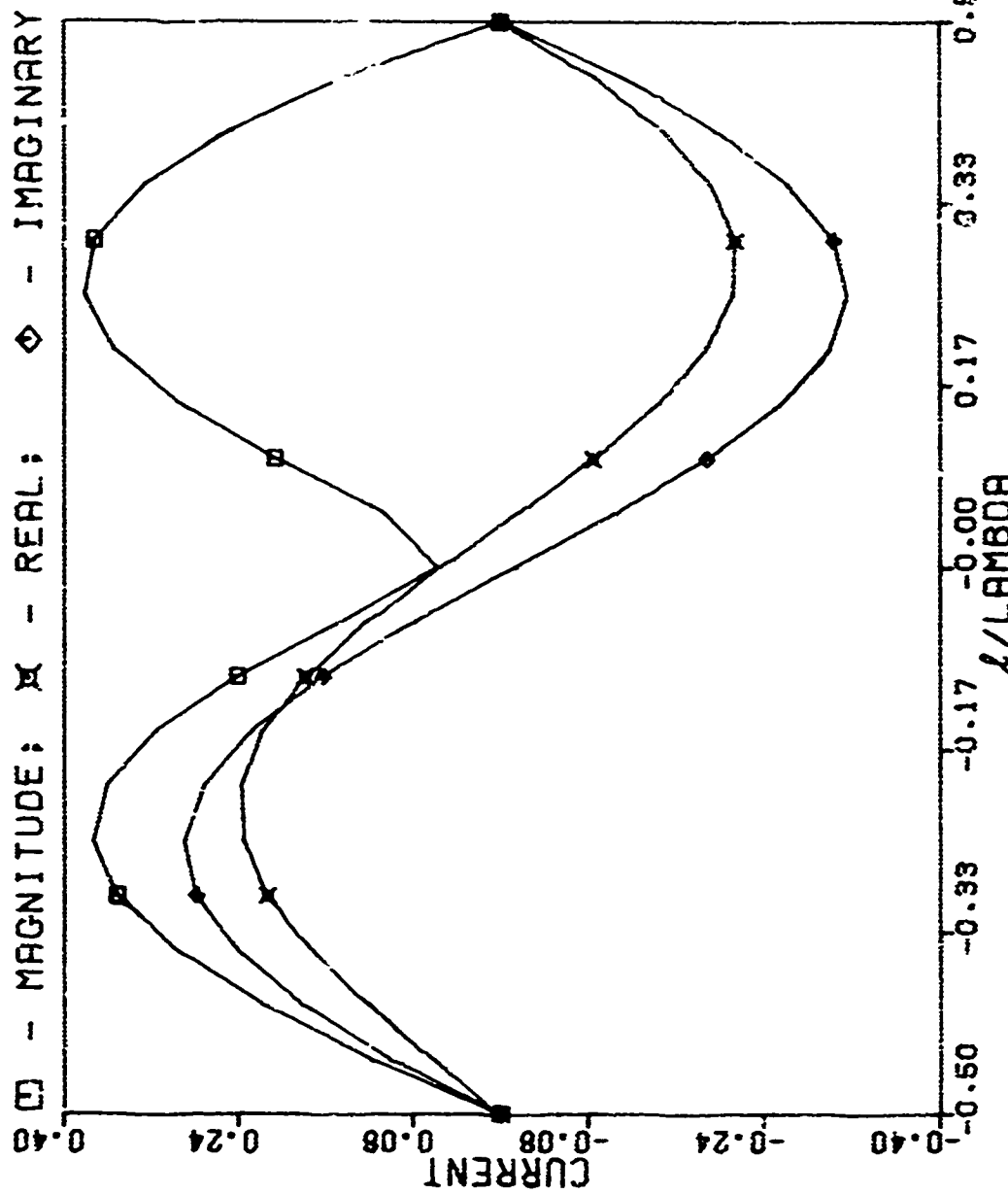


Figure G.3. Current induced on a wire near a square plate, $s_x = 0.5\lambda$, $y_d = 0.5\lambda$, $L = 1.0\lambda$, $a = .001\lambda$, $\vec{F}_{C_0} = (-0.125\lambda, -0.125\lambda, 0.525\lambda)$, $\hat{\delta} = (0.0, 0.0, 1.0)$, $\theta = 0^\circ$, $\phi = 0^\circ$, $H_0 = 0.0$, $H_\phi = -1.0$. The plate current is shown in Figure G.2.

of length $L = \lambda$ and radius $a = 0.001\lambda$, due to illumination which is normally incident upon the plate but which does not excite the thin wire directly. The wire is perpendicular to the plate and is located above the point $(-0.325\lambda, -0.125\lambda)$ on the plate. Other details of plate/wire geometry and incident illumination are recorded in the labels of Figures G.2 and G.3. Since the incident electric field \bar{E}^i is normal to the wire, it does not excite the wire directly and, hence, the sole illumination of the wire is due to scattering from the plate. One recalls that the antiresonant current on a one-wavelength thin wire is an odd function and can be induced by only an odd-function excitation (with respect to the wire center), while the forced response on a wire of any length is even for an even-function excitation and is odd for an odd-function excitation. Since the only illumination received by the wire is the electric field scattered from the plate, which decays rapidly along the wire axis, one expects a relatively significant odd-function excitation compared with the even-function part. In addition, the antiresonant (sinusoidal) current is more readily excited on a one-wavelength wire than is the forced response. As one would anticipate from the brief discussion above, the current on the wire illustrated in Figure G.3 is essentially sinusoidal. The slight deviation from a sinusoidal distribution is due to the even-function portion of the forced response. The

plate current \bar{J}_s depicted in Figure G.2 is almost what it would be if the wire were not present; small differences can be observed primarily near the wire location and in the small asymmetry introduced by the presence of the wire.

With the plate/wire geometry as stated above but with the incident electric field now parallel to the wire and perpendicular to the plate (see labels in Figures G.4 and G.5), one observes essentially the expected shifted cosine current on the one-wavelength wire, which is the forced response due to a constant illumination. The slight deviation from the shifted cosine manifested in the asymmetry of the current of Figure G.5 is due to the fact that a small antiresonant current is induced by the odd-function, axial electric field which exists on the wire due to secondary scattering from the plate. The plate current (Figure G.4) is excited only by scattering of the incident field from the wire with no direct contribution from the incident illumination itself. Notice that the plate current is symmetric about the diagonal passing through $(-0.125\lambda, -0.125\lambda)$ over which the wire is located and that this current is significantly smaller, as expected, than the current depicted in Figure G.2.

Next we consider the same $0.5\lambda \times 0.5\lambda$ square plate but with a wire parallel to it. The wire length and radius are 0.5λ and 0.001λ , respectively, its center is 0.1λ above the point $(-0.125\lambda, 0)$, and its axis is parallel to the y-

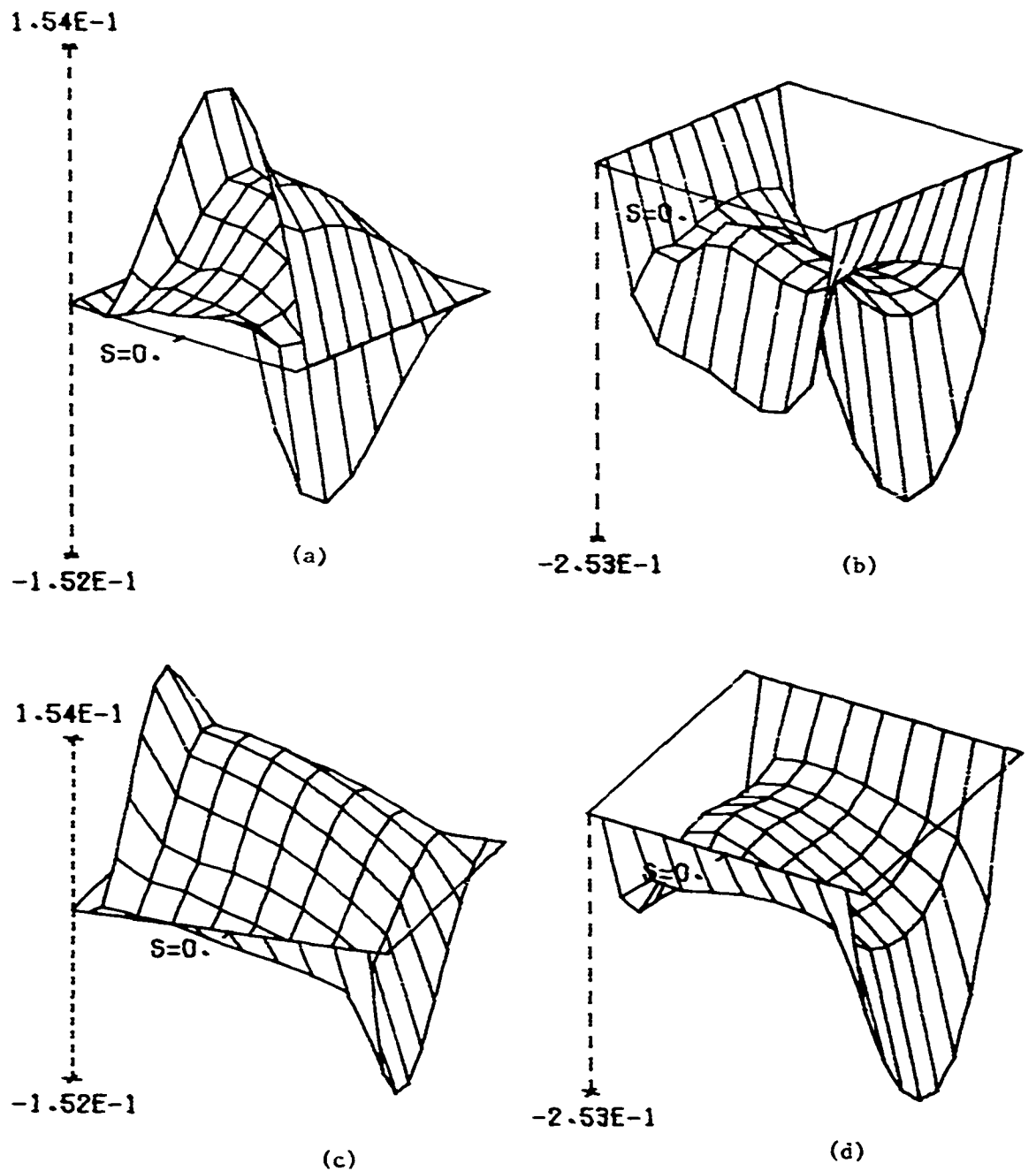


Figure G.4. Current induced on a square plate near a wire, $S_x = 0.5\lambda$, $Y_d = 0.5\lambda$, $I = 1.0\lambda$, $a = .001\lambda$, $\vec{r}_c = (-0.125\lambda, -0.125\lambda, 0.525\lambda)$, $\hat{i} = (0.0, 0.0, 1.0)$, $\theta = 90^\circ$, $\phi = 0^\circ$, $H_\theta = 0.0$, $H_\phi = 1.0$; (a) $\text{Re}(J_s)$, (b) $\text{Im}(J_s)$, (c) $\text{Re}(J_y)$, (d) $\text{Im}(J_y)$. The wire current is shown in Figure G.5.

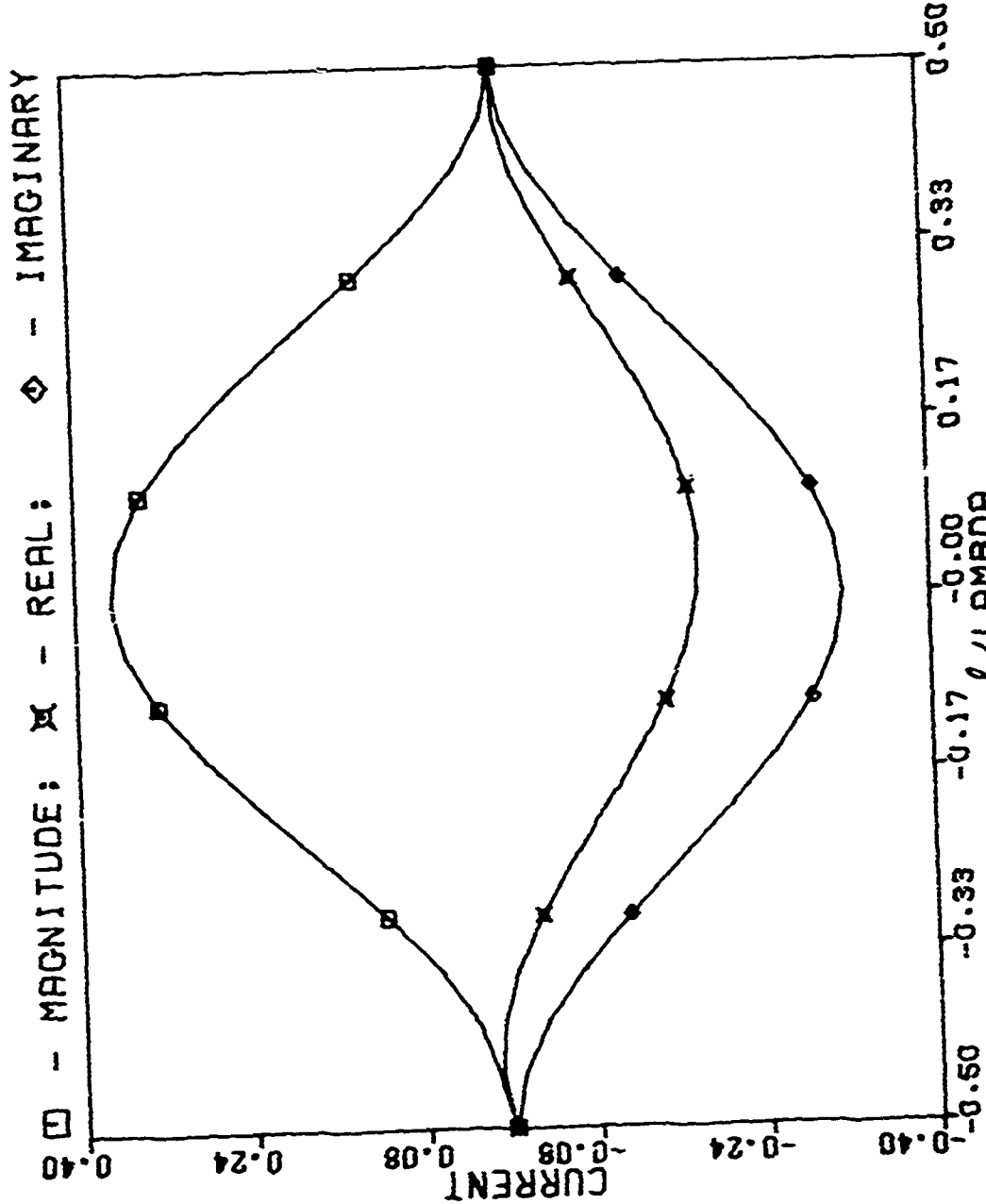


Figure G.5. Current Induced on a wire near a square plate, $S_x = 0.5\lambda$, $y_d = 0.5\lambda$, $l = 1.0\lambda$, $a = .001\lambda$, $T_c = (-0.125\lambda, -0.125\lambda, 0.525\lambda)$, $\hat{x}^d = (0.0, 0.0, 1.0)$, $\theta = 90^\circ$, $\phi = 0^\circ$, $H_0 = 0.0$, $H_\phi = 1.0$. The plate current is shown in Figure G.4.

axis. The illumination is normally incident upon the plate with polarization such that $\vec{E}^i \cdot \hat{\lambda} = 0$; so the only wire excitation is due to scattering from the plate. A half wavelength wire is resonant length and the resonant current is an even function with respect to the wire center. This resonant current can be excited only by an even-function illumination. We note from Figure G.6 that the presence of the wire has little or no discernable effect on the plate current. Also, the distribution of plate current is such that the illumination of the wire is an odd function which can induce no even-function resonant wire current. The wire current seen in Figure G.7 is entirely forced and is an odd function about the wire center as expected. This non-resonant current is small and should not be viewed as sinusoidal (of wavelength λ), even though its shape appears to be (of wavelength $\lambda/2$).

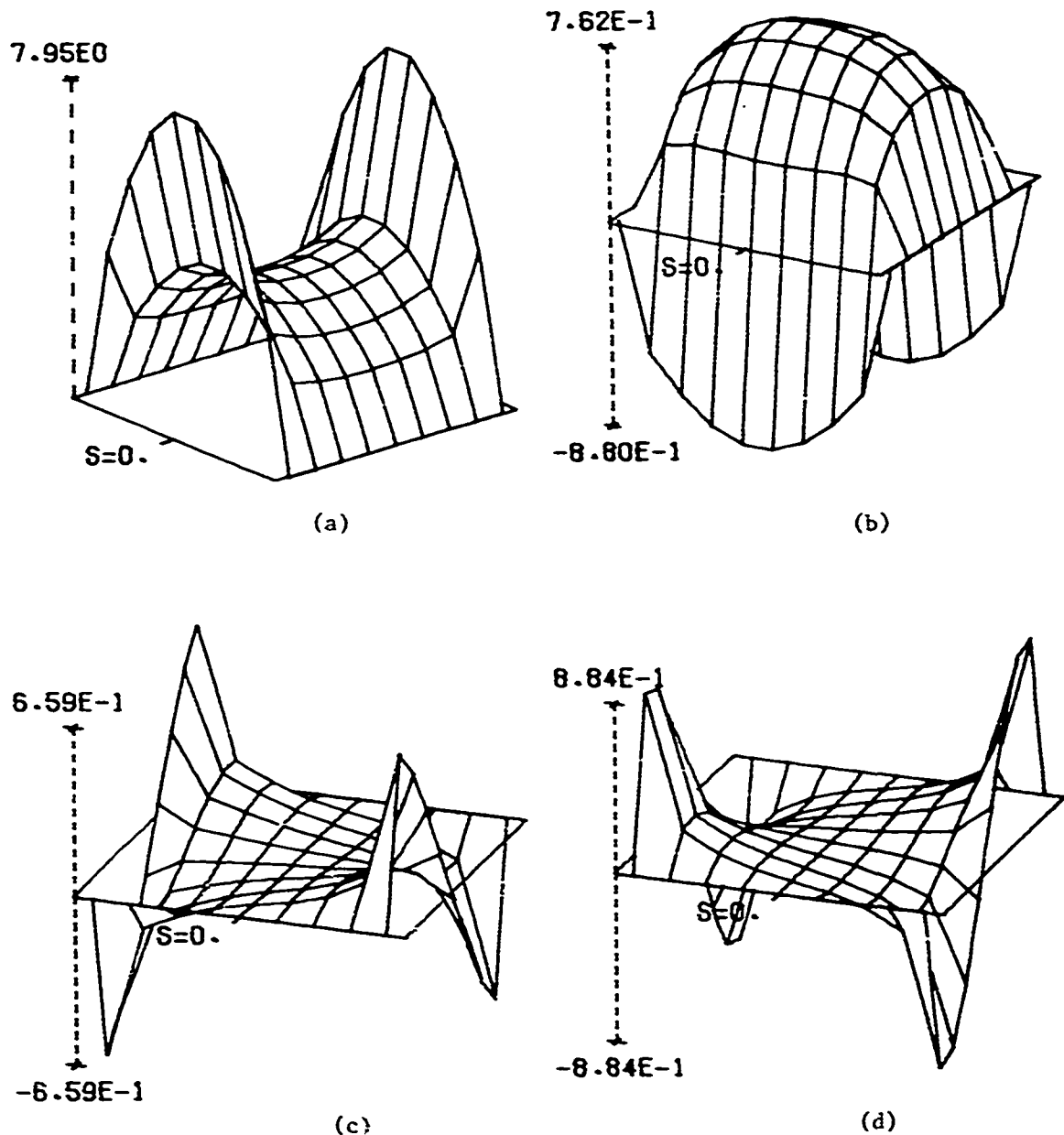


Figure G.6. Current induced on a square plate near a wire, $S_x = 0.5\lambda$, $Y_d = 0.5\lambda$, $L = 0.5\lambda$, $a = .001\lambda$, $\bar{r}_c = (-0.125\lambda, 0.0, 0.1\lambda)$, $\hat{z} = (0.0, 1.0, 0.0)$, $\theta = 0^\circ$, $\phi = 0^\circ$, $H_\theta = 0.0$, $H_\phi = -1.0$; (a) $\text{Re}(J_s)$, (b) $\text{Im}(J_s)$, (c) $\text{Re}(J_y)$, (d) $\text{Im}(J_y)$. The wire current is shown in Figure G.7.

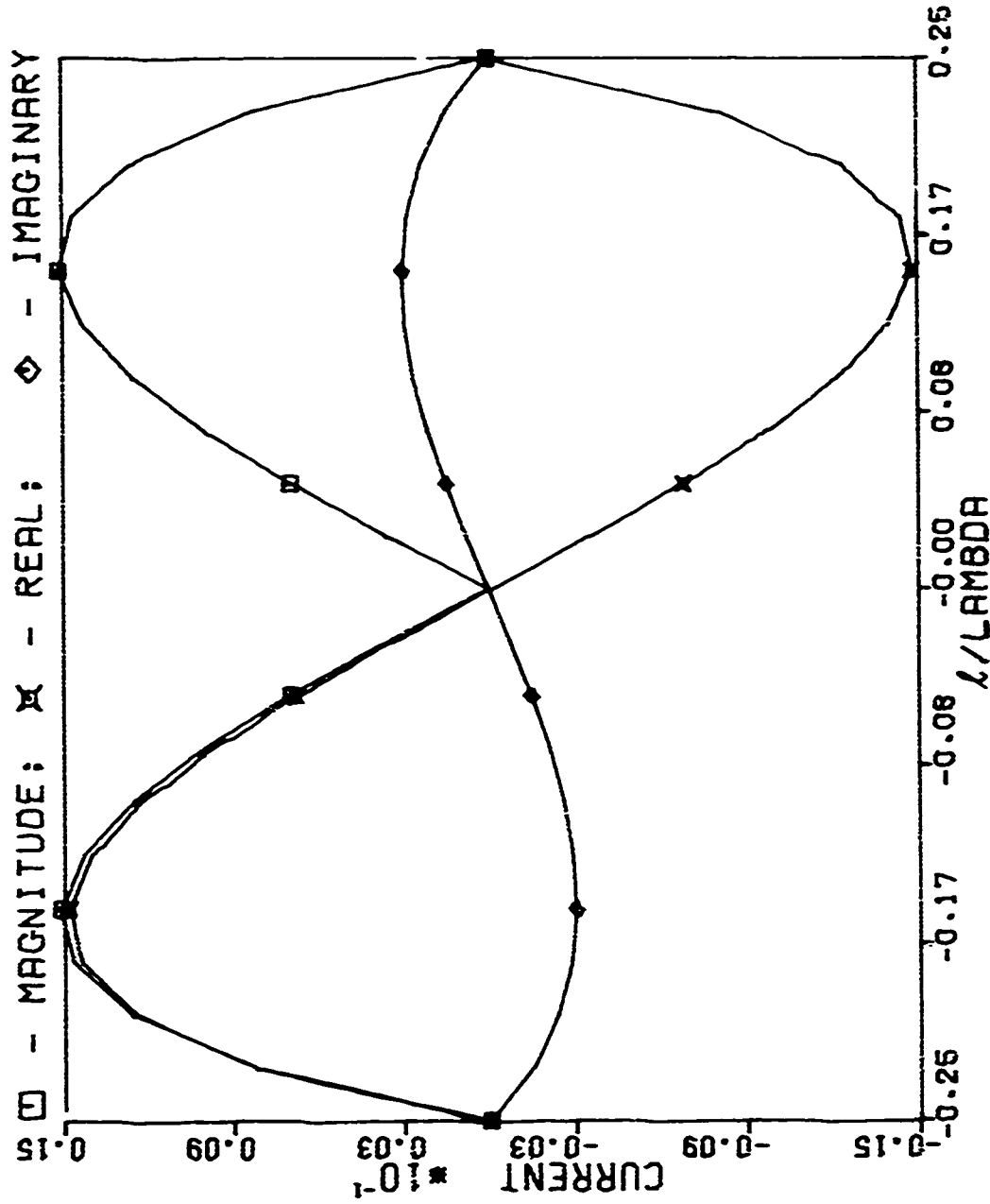


Figure G.7. Current Induced on a wire near a square plate, $S_x = 0.5\lambda$, $Y_d = 0.5\lambda$, $L = 0.5\lambda$, $a = .001\lambda$, $F_{c_0} = (-0.125\lambda, 0.0, 0.1\lambda)$, $\hat{z} = (0.0, 1.0, 0.0)$, $\theta = 0^\circ$, $\phi = 0^\circ$, $H_0 = 0.0$, $H_\phi = -1.0$. The plate current is shown in Figure G.6.

REFERENCES

- [1] R. F. Harrington, Field Computation by Moment Methods. New York: Macmillan, 1968.
- [2] Y. Rahmat-Samii and R. Mittra, "Integral Equation Solution and RCS Computation of a Thin Rectangular Plate," IEEE Trans. Ant. and Prop., Vol. AP-22, pp. 608 - 610, July 1974.
- [3] D. R. Wilton and O. C. Dunaway, "Electromagnetic Penetration through Apertures of Arbitrary Shape: Formulation and Numerical Solution Procedure," Report No. TR-74-192 for Air Force Weapons Laboratory, Kirtland AFB, NM, by University of Mississippi, University, MS, August 1975.
- [4] D. S. Jones, The Theory of Electromagnetism. New York: Pergamon, 1964, pp. 567 - 568.
- [5] D. R. Wilton and S. Govind, "Incorporation of Edge Conditions in Moment Method Solutions," accepted for publication by IEEE Trans. Ant. and Prop..
- [6] R. F. Harrington, Time-Harmonic Electromagnetic Fields. New York: McGraw-Hill, 1961.
- [7] J. Van Bladel, Electromagnetic Fields. New York: McGraw-Hill, 1965, pp. 354 - 355.
- [8] R. S. Satterwhite and R. G. Kouyoumjian, "Electromagnetic Diffraction by a Perfectly Conducting Plane Angular Section," Tech. Rept. No. 2183-2 for Air Force Cambridge Research Laboratories, USAF, Bedford, MA, by The Ohio State University, Columbus, OH, March 1970.
- [9] R. W. P. King, Fundamental Electromagnetic Theory. New York: Dover, 1963, pp. 84 - 88 and pp. 272 - 273.